1-1-1991

Regular and chaotic mixing of viscous fluids in eccentric rotating cylinders/

Paul D. Swanson
University of Massachusetts Amherst

REGULAR AND CHAOTIC MIXING OF VISCOUS FLUIDS IN ECCENTRIC ROTATING CYLINDERS

A Dissertation Presented

by

PAUL D. SWANSON

Submitted to the Graduate School of the

University of Massachusetts in partial fulfillment

of the requirements for the degree of

DOCTOR OF PHILOSOPHY

May 1991

Department of Polymer Science and Engineering

by

Paul D. Swanson

REGULAR AND CHAOTIC MIXING OF VISCOUS FLUIDS IN ECCENTRIC ROTATING CYLINDERS

A Dissertation Presented

by

Paul D. Swanson

Approved as to style and content by:

Julio M. Ottino, Chairman of Committee

David A. Hoagland, Member

Jonathan Machta, Member

Alexander Eydeland, Member

William McKnight, Department Head
Department of Polymer Science and Engineering

ACKNOWLEDGMENTS

There are a number of people who deserve ackknowledgment for shaping the course of this research and my graduate experience in general. First, I would like to thank my advisor, Julio Ottino, for the patience he has shown. I appreciate the interest my committee has shown during all of our discussions. Finally, I would like to thank all the members of the Ottino research group (and I am probably the last one to have known all of them) for many fruitful and stimulating discussions. All of our discussions, not just the discussions about research for I believe that education in graduate school should extent beyond a particular research topic.

ABSTRACT

REGULAR AND CHAOTIC MIXING OF VISCOUS FLUIDS IN ECCENTRIC ROTATING CYLINDERS

May 1991

PAUL D. SWANSON, B.S., UNIVERSITY OF MINNESOTA

Ph.D., UNIVERSITY OF MASSACHUSETTS

Directed by: Professor Julio M. Ottino

In this research we study the mixing of viscous fluids in a model flow, the eccentric cylinder system. The flow between eccentric rotating cylinders is used because an analytic expression for the stream function exists and we have fabricated an apparatus to experimentally generate the flow. We use the flow to determine the extent to which several computational methods are able to predict the experimental mixing in the flow. We have found that Poincaré sections give a good indication of the maximum extent of mixing in the experiments but they give no information on the rate of mixing. The locations of elliptic periodic points give an indication of where 'islands' of regular behavior will occur in the flow. The manifolds of the hyperbolic periodic point with the largest eigenvalue give a template of the striation pattern which forms in the experiments. Finally, stretching plots appear to match the experiments quite well.

We have found that co-rotation of the cylinders leads to mixing over a larger region of the flow domain than the equivalent counter-rotating motion of the cylinders. Driving the cylinders with different waveforms appears to produce little or no difference in the mixing. The Melnikov method has been adapted to adjust the waveforms such that the resultant mixing is in even closer agreement. In addition, we have determined that the points which stretch the most start on the stable manifold of a hyperbolic periodic point and end up on the unstable manifold. This results in the stretching plots assuming the shape of the manifolds and consequently matching the striation patterns of the experiments.

Finally, we have determined that the methods of analysis presented here can be applied to flows where only a discretized representation of the velocity field exists. This means that our methods of analysis will be effective even when the flow field must be determined numerically.

TABLE OF CONTENTS

LIST OF FIGURES

CHAPTER 1

INTRODUCTION

> Hardly any polymer process occurs without mixing playing an important, and often controlling, role. Yet of all the processes which make up an integrated operation, mixing is probably the least understood, and the least amenable to analysis. *Stanley Middleman*

This quotation from Middleman [1] sums up the state of not only mixing in polymer processing but fluid mixing in general. Initially, it appears puzzling that anyone would think mixing is not well understood. After all, everyone performs uncountable mixing tasks every day, whether it be mixing cream in coffee or adjusting the temperature of the shower. However, the pervasiveness of mixing or the ability to solve individual mixing problems empirically does not imply that mixing is understood from a general point of view. Upon deeper inspection it becomes clear that there are difficulties in developing a general, quantitative theory for the prediction of fluid mixing. First, the reason fluids are being mixed, and hence the concept of 'good' mixing, often depends on the specific process or product. Different processes can have widely differing criterion for judging mixing. Second, mixing problems of practical interest occur in flows or with fluids which invariably are complex, making

it difficult to separate the mixing from the fluid mechanics. The ultimate example of this is turbulence where the terms mixing and turbulent are sometimes used interchangeably.

A straightforward engineering approach to studying the mixing problem would be to define a measure so that a number which describes how well it is mixed could be attached to any particular mixture. Ideally the mixing measure would be a simple function of the velocity field. With this measure in hand one could proceed directly to mixing problems of practical interest. The measure would be used to determine how the 'goodness' of mixing varied with the various system parameters. However, this approach invariably leads to quotes such as Middleman's. At best such an approach will allow the determination of mixing in one particular system or for one purpose.

Rather than using the approach described above, which would invariably be quite restricted in applicability, we would like to study mixing from as general a viewpoint as possible. To frame the problem properly we make a number of assumptions. First, the most complete mixing 'measure' is assumed to be an actual picture of the mixed system. Whereas it is possible to extract any measure from the picture it is impossible to reconstruct the full picture from a measure. Second, we are interested in mixing and not in fluid mechanics so we would like to study mixing in a system with a known and simple velocity field. One consequence of

this restriction is that the deformation, or mixing, can be calculated for any initial configuration of fluid given enough computer power. However, it should be stressed that the required computer power may be enormous, possibly beyond the ability of all current computing power [2]. One of our primary goals is to develop methods which can predict some of the mixing behavior of a flow without resorting to brute force simulation of the experiments.

In its most general form fluid mixing is the motion of fluid elements i.e. kinematics. The mixing problem from a kinematical viewpoint is actually a solution to:

$$\frac{d\mathbf{x}}{dt} = \mathbf{v}(\mathbf{x}). \tag{1.1}$$

This is the standard definition of a dynamical system so we expect that dynamical systems concepts will be of use in the study of mixing. Further, the aspects of dynamical systems theory dealing with chaotic dynamics should be particularly useful for our work.

The main goal of this thesis is to determine the information various dynamical systems ideas, adapted or refined as necessary, can tell us about mixing. An obvious way to test the usefulness of these ideas is to develop a model system which is both experimentally realizable (so that we can conduct actual mixing experiments) and amenable to analysis by dynamical systems concepts. One system which meets these criteria is the flow between eccentric rotating cylinders, sometimes known as

the journal bearing flow; an analytic expression for the stream function exists and an experimental apparatus can be created to generate the flow. The journal bearing has been studied numerically and experimentally by others [3, 4, 5, 6] in the context of chaos in dynamical systems. But the focus of these authors was to demonstrate that physically realizable chaotic flows do exist. They did not examine the connection between chaotic behavior and effective mixing.

We begin in chapter 2 with a very brief review of the dynamical systems comments used in this work. Then we discuss the eccentric cylinder geometry, the analytic expression for the stream function, and the periodic modulation of the boundary cylinder motion we use to generate chaos. Chapter 3 describes the experimental apparatus and the experimental procedure used. In addition it contains the experimental results from the steady and chaotic flows. These results form the 'measure' of mixing which we use to evaluate our computational techniques. In chapter 4 we describe several computational techniques, adapted to the study of mixing from dynamical systems, and discuss their usefulness. In chapter 5 we examine in greater detail some of the unexpected results of this work, specifically the difference between co- and counter-rotational flows, the similarity in the mixing created by different waveforms, and the agreement between the stretching plots and experiments. In all cases we have developed explanations of why these initially unexpected results should occur. Finally, in chapter 6 we examine the feasibility of applying the tools

developed in chapter 4 to systems where there is no explicit expression for the velocity field - only a finite element representation of the velocity field; there are few experimental mixing systems, and even fewer of practical importance, where an exact expression for the velocity field exists so it is important to examine how well the techniques developed here work with an approximate velocity field.

The topics presented in this thesis are quite far removed from traditional polymer science or chemical engineering. Consequently, have a large body of background information which many readers may not be familiar with but is beyond the scope of this thesis to present. What follows are a number of references which we have found to be the most useful in providing the necessary background information. Percival and Richards [7] provides a clear introduction to dynamics, mainly of Hamiltonian systems. The four part series of books by Abraham and Shaw [8, 9, 10, 11] provide an excellent visual presentation of chaos in dynamical systems. Baker and Gollub [12] provide an introduction to the terminology of dynamics and chaos in the context of the forced pendulum. Finally, Guckenheimer and Holmes [13] and Lichtenberg and Lieberman [14] are general references for dynamical systems and chaos but are not recommended as introductory texts.

CHAPTER 2

PRELIMINARIES

The purpose of this chapter is twofold: First, provide the necessary dynamical systems theory background and second, introduce the eccentric cylinder geometry. The dynamical systems theory section focuses only on topics directly relevant to this thesis and then only in a very cursory manner. The part dealing with the eccentric cylinder geometry discusses the analytic expression for the stream function and the method of perturbing the flow to produce chaos.

2.1 Chaos in Two-Dimensional Hamiltonian Systems

What follows is a very brief review of the aspects of chaos in two-dimensional Hamiltonian systems which we will use in our mixing studies. The frictionless pendulum is used as an example to introduce the important concepts. A far more complete presentation of this material is given by Ottino [15] or Baker and Gollub [12].

Two dimensional, incompressible flow problems can be solved through the use of a stream function, Ψ. The velocity field is derived from the stream function according to:

$$v_x = \frac{dx}{dt} = -\frac{\partial \Psi}{\partial y}; \; v_y = \frac{dy}{dt} = \frac{\partial \Psi}{\partial x}. \tag{2.1}$$

Physically, this means that the fluid flows along level curves of the stream function. In an analogous manner, the dynamics in a Hamiltonian system are prescribed by:

$$\frac{dp}{dt} = -\frac{\partial H}{\partial q}; \; \frac{dq}{dt} = \frac{\partial H}{\partial p} \tag{2.2}$$

which is the mathematical way to state that trajectories in a Hamiltonian system follow level curves of the Hamiltonian, H. Clearly, these two types of dynamical systems are quite similar. Any results from Hamiltonian mechanics which are valid for arbitrary Hamiltonians will also apply to fluid flows governed by a stream function solution.

A familiar example of a Hamiltonian system is the frictionless pendulum. In this case p is the momentum of the pendulum and q is the position (which determines its potential energy). The Hamiltonian represents the total energy of the system. A plot of the phase space of the pendulum is shown in figure 2.1[1]. Of particular importance are the hyperbolic points and the separatrixes. Physically for the pendulum the hyperbolic points represent the unstable steady state where the pendulum is standing straight up. The separatrixes represent the boundary between oscillation in the pendulum and continuous rotation i.e. the pendulum spins around and around. In dynamical systems terminology the separatrixes are also called *manifolds*.

[1]Figures 2.1, 2.2, and 2.3 courtesy of Tom Danielson.

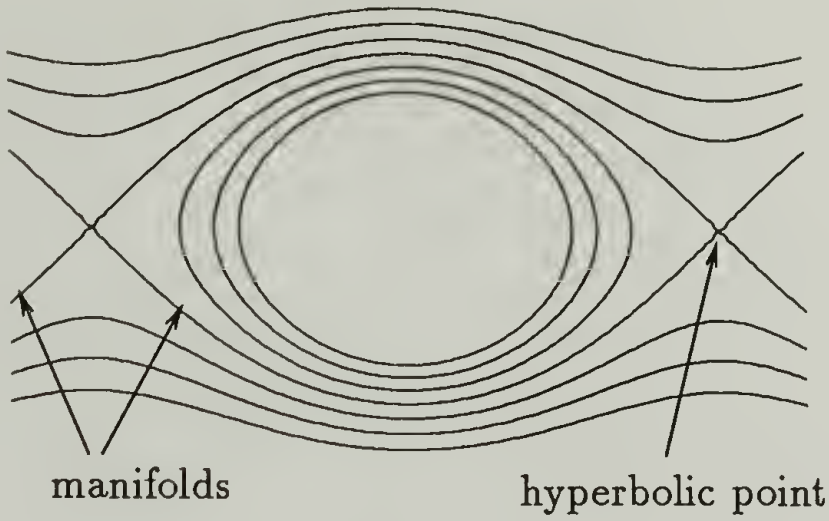

Figure 2.1: Phase space for the frictionless pendulum.

If the Hamiltonian of the pendulum is perturbed by adding a periodically time dependent function of period T which is also Hamiltonian[2] the new dynamical system is still Hamiltonian. The new Hamiltonian governing the system is

$$H_{new}(p, q, t) = H_{old}(p, q) + \epsilon G(p, q, t) \tag{2.3}$$

where G has the property

$$G(p, q, t) = G(p, q, t + T). \tag{2.4}$$

The new dynamical system may exhibit chaotic behavior i.e. some orbits may no longer follow smooth, closed trajectories in phase space but rather will appear to move in an erratic fashion through some region of the phase space.

[2]All of the properties described here are applicable to more general types of perturbation. However, we use this form because it is equivalent to the perturbation we will on the eccentric rotating cylinder flow.

Time dependence adds a new variable to the system so the phase space is now three dimensional instead of two dimensional. However, the phase space can be reduced back to two dimensions by creating a map from the continuous system. Since we have periodic time dependence we can think of the phase flow as occurring on a torus. The cross section of this torus is the (p, q) space, the phase space of the original unperturbed system, and time marks the location around the torus. An arbitrary plane perpendicular to the time variable will be intersected once every period T by all trajectories. As a result most of the behavior of the three dimensional system can be seen in this two dimensional cross section. Such a cross section is referred to as a *Poincaré section.* To create the Poincaré section we pick an arbitrary time, say t_0, and then mark the locations of trajectories in (p, q) space at this time and every period thereafter, i.e. we mark the trajectories at times of $t_0 + nT$. Note that this creates a mapping and trajectories will appear to jump from one position to another rather than move continuously. Many properties of the original phase space are retained. The most important of these are that the map preserves area, it is continuous in the sense that a line will be mapped into a line, trajectories are unique, and the map has an inverse. In mathematical terminology the mapping is a diffeomorphism.

If a Poincaré section were created for the steady flow a picture identical to figure 2.1 would emerge. In this case the choice of period, T, is arbitrary. Figure 2.2

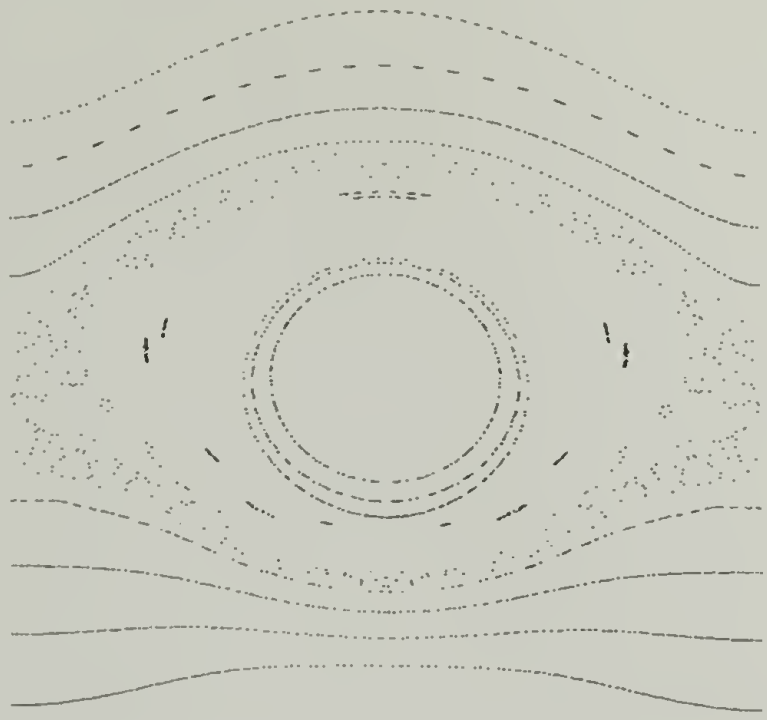

Figure 2.2: Possible Poincaré section for the perturbed frictionless pendulum.

shows how a Poincaré section for the perturbed flow might appear. Some of the trajectories appear to lie on closed curves just as in the unperturbed system. These trajectories are called *regular* since they are the same as in the unperturbed flow. However, other of the trajectories form a hazy cloud of points in a fairly well defined region of the flow. This region is called the *chaotic* region since the cloud of points appears to be random.

In the steady flow it appears that a manifold smoothly connects one hyperbolic point to another. However, in reality there are two manifolds. One is the stable manifold, along which trajectories move closer to a hyperbolic point, and the other is the unstable manifold, along which points move away from a hyperbolic point. In the steady flow the manifolds lie directly on top of each other and appear as a

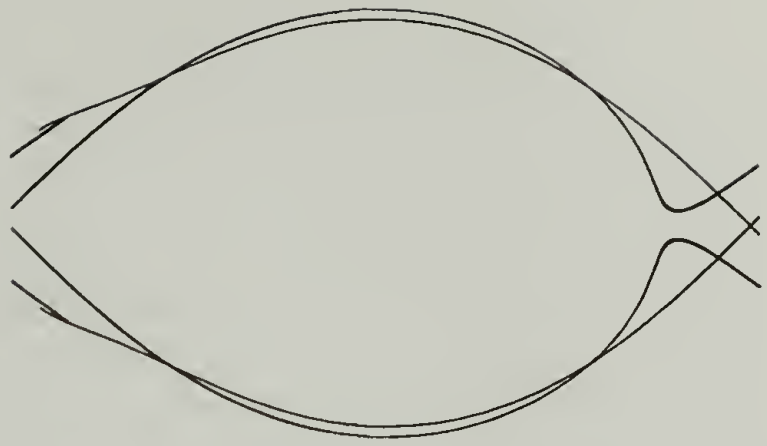

Figure 2.3: Depiction of the separation of the manifolds in the perturbed frictionless pendulum.

single manifold. However, figure 2.3 shows that when the flow is perturbed the manifolds come apart and clearly they are separate entities. If the manifolds intersect transversally as they do in figure 2.3 the system also exhibits chaos. This is one of the definitions of chaos.

One method which can quantify the separation of the stable and unstable manifolds, at least for small perturbations, is the Melnikov method (see [16], [13] for a more detailed description). The goal of the Melnikov method is to determine the signed distance between the stable and unstable manifolds. If the distance changes signs there is a transverse intersection of the stable and unstable manifolds and the system is then proven to be chaotic.

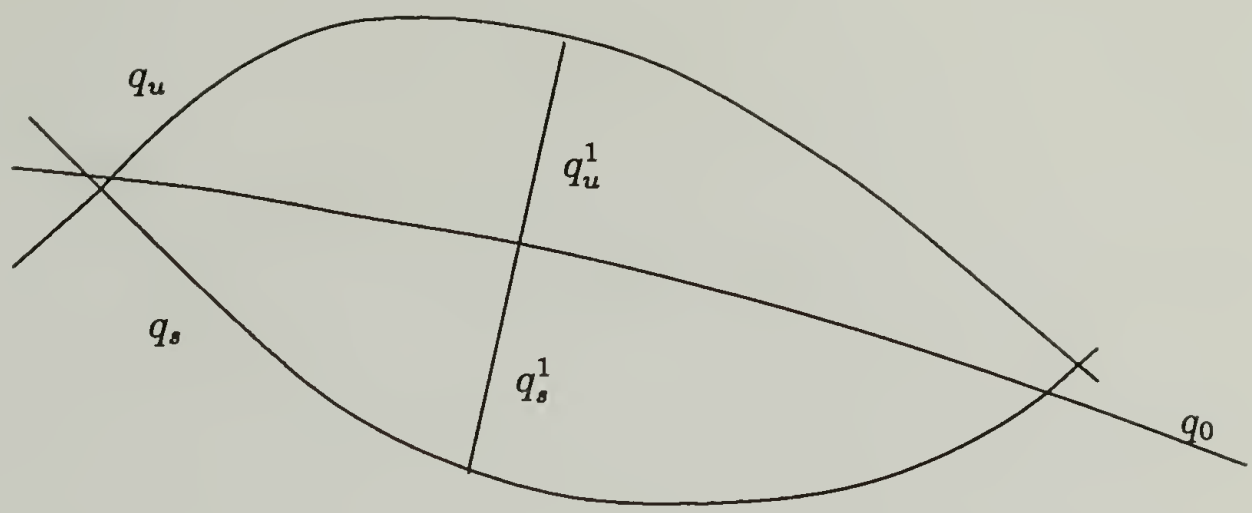

Figure 2.4: Representation of the perturbed manifolds by the unperturbed manifold.

The Melnikov method begins with the assumption that the stable and unstable manifolds of the perturbed system can be expressed as first order perturbations of the unperturbed manifold, i.e. if $q_0(t)$ represents the unperturbed manifold, where t parameterizes the location along it, then the stable and unstable manifolds can be written as:

$$q_s(t) = q_0(t) + \epsilon q_s^1(t) + \mathcal{O}(\epsilon^2) \tag{2.5}$$

$$q_u(t) = q_0(t) + \epsilon q_u^1(t) + \mathcal{O}(\epsilon^2) \tag{2.6}$$

where $q_s^1(t)$ and $q_u^1(t)$ represent the perpendicular distances from stable and unstable manifolds to the unperturbed manifold at position t of the unperturbed manifold. This is shown schematically in figure 2.4. The distance between the manifolds is then

$$d(t) = q_s(t) - q_u(t) = \epsilon[q_s^1(t) - q_u^1(t)] \sim \epsilon M(t) \tag{2.7}$$

where d is the distance and $M(t)$ is the Melnikov function. If a perturbed Hamiltonian system has the form of equation 2.3, i.e.

$$H_{pert}(x, y, t) = H(x, y) + \epsilon G(x, y, t), \tag{2.8}$$

then the Melnikov function is

$$M(t_0) = \int_{-\infty}^{\infty} \{H(q_0(t)), G(q_0(t), t + t_0)\} dt \tag{2.9}$$

where

$$\{H, G\} = \frac{\partial H}{\partial x}\frac{\partial G}{\partial y} - \frac{\partial H}{\partial y}\frac{\partial G}{\partial x} \tag{2.10}$$

which is the Poisson bracket of H and G. The expression $H(q_0(t))$ represents evaluation of the Hamiltonian at position $q_0(t)$ along the unperturbed manifold. This means that H and G are integrated along the unperturbed manifold to evaluate the Melnikov function. An important point is that the Melnikov method is guaranteed to be valid only for small perturbations. Physically it is easy to see why this is true; if the perturbation is large the perturbed manifolds become very wild and it is no longer possible to represent them with the unperturbed manifold.

2.2 The Journal Bearing Flow

The journal bearing or eccentric cylinder geometry is shown in figure 2.5. The flow region is contained in the annulus between two infinitely long cylinders whose central axes are parallel but not coincident, i.e. the cylinders are eccentric. The

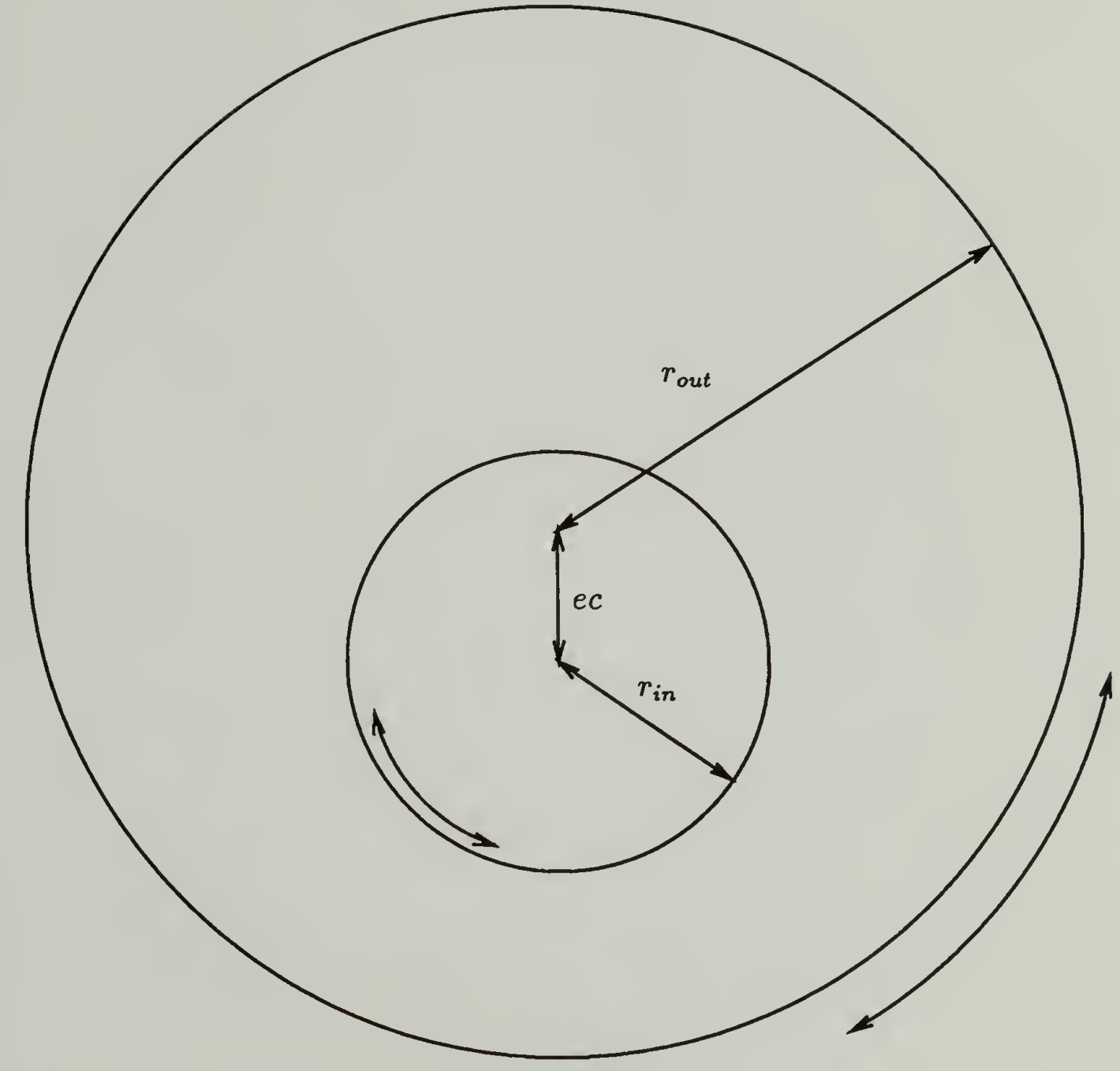

Figure 2.5: Journal bearing geometry. The basic geometry is determined by two parameters, the ratio of the radii of the inner and outer cylinders and the ratio of the distance between the centers of the two cylinders (the eccentricity) to the radius of the outer cylinder.

geometry of the system is completely determined by two dimensionless parameters, the ratio of the radius of the inner cylinder to the radius of the outer cylinder, $r = r_{in}/r_{out}$, and the distance between the centers of the two cylinders, ec, normalized by the radius of the outer cylinder $e = ec/r_{out}$. Note that $0 < r + e < 1$.

If the fluid between the cylinders is incompressible the problem can be solved through the use of the stream function. If we further assume that the flow is steady and inertial effects are negligible then the stream function can be found by solving the biharmonic equation, $\nabla^4\Psi$, using the appropriate boundary conditions. Analytic expressions for the stream function can be found in a variety of sources [17, 18, 19, 20, 21, 22]. We choose the solution presented by Wannier[22] because it is given in rectangular coordinates in contrast to the other solutions which are given in bipolar coordinates. Rectangular coordinates simplify several computational aspects of the problem such as the graphics. Wannier's solution is given in the appendix.

A variety of streamline patterns can be generated in the journal bearing flow. Figure 2.6 shows the basic types of streamline patterns which are possible. The patterns of greatest importance to this work are the co- and counter-rotating cases for $e = 0.3$. These are the flows which are perturbed to generate chaotic flows. Note that the counter-rotating streamline pattern has a hyperbolic point in the narrow gap between the inner and outer cylinders and there is a large recirculation region above the inner cylinder. This is similar to the pendulum example discussed in the

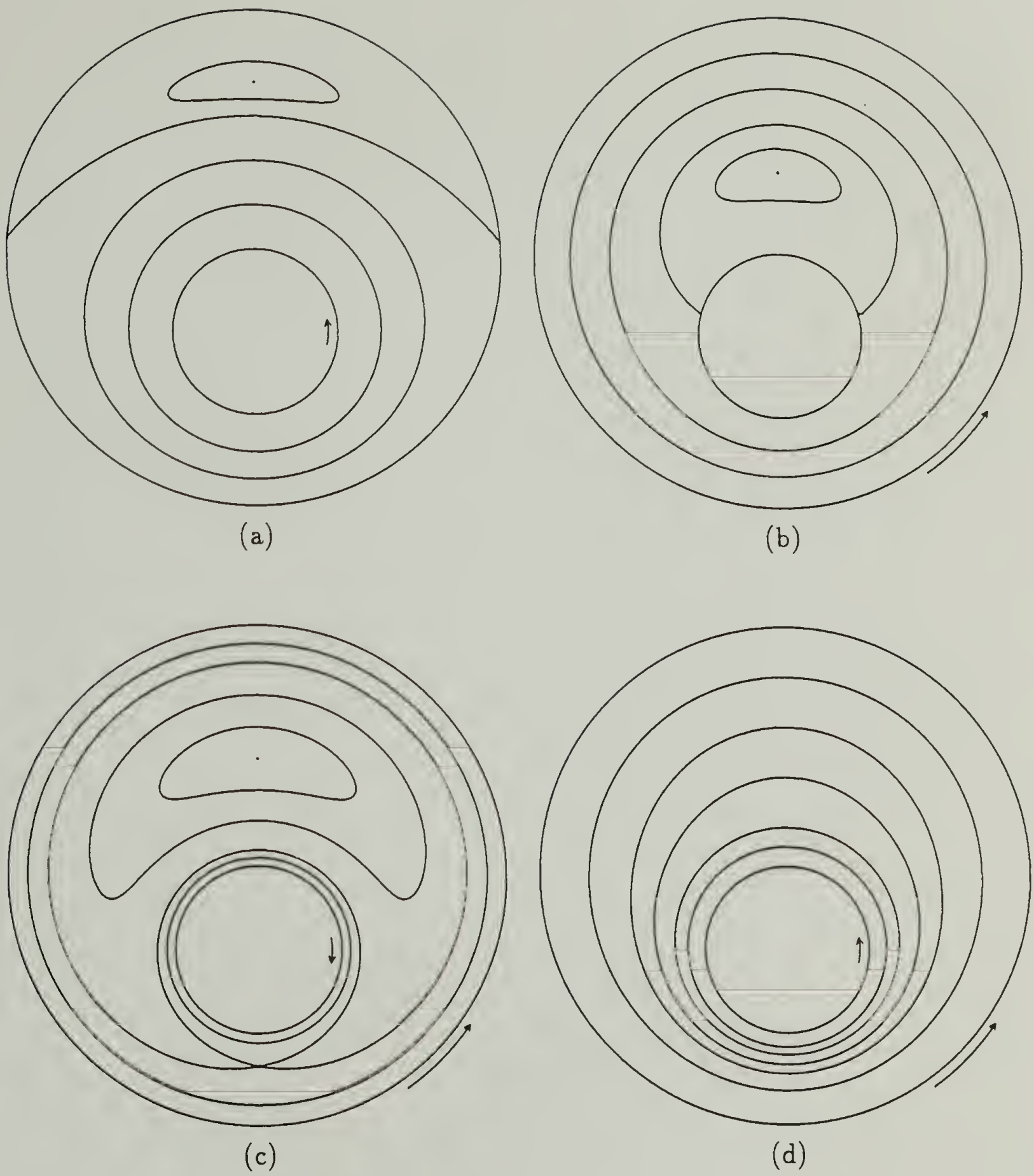

Figure 2.6: Streamline patterns in the eccentric cylinder apparatus. For all plots the ratio of the radii is 1/3. For parts (a)-(d) $e = 0.3$ and for parts (e)-(g) $e = 0.5$. The cylinder velocities are: (a) $v_{out} = 0$, (b) $v_{in} = 0$, (c) $v_{in} = -v_{out}$, (d) $v_{in} = v_{out}$, (e) $v_{out} = 0$, (f) $v_{in} = 0$, and (g) $v_{in} = 3v_{out}$.

Continued, next page.

(e)

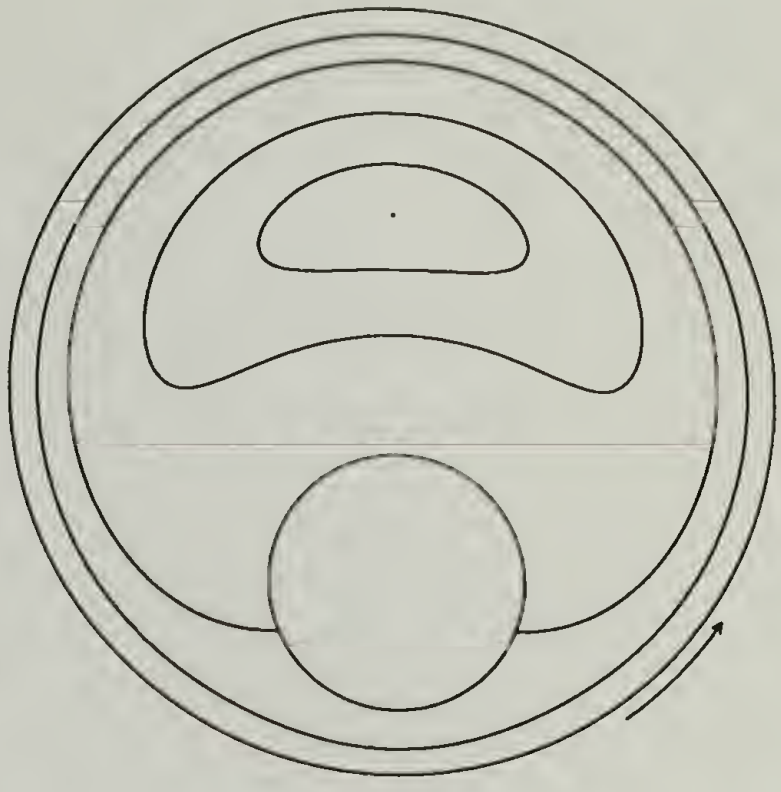

(f)

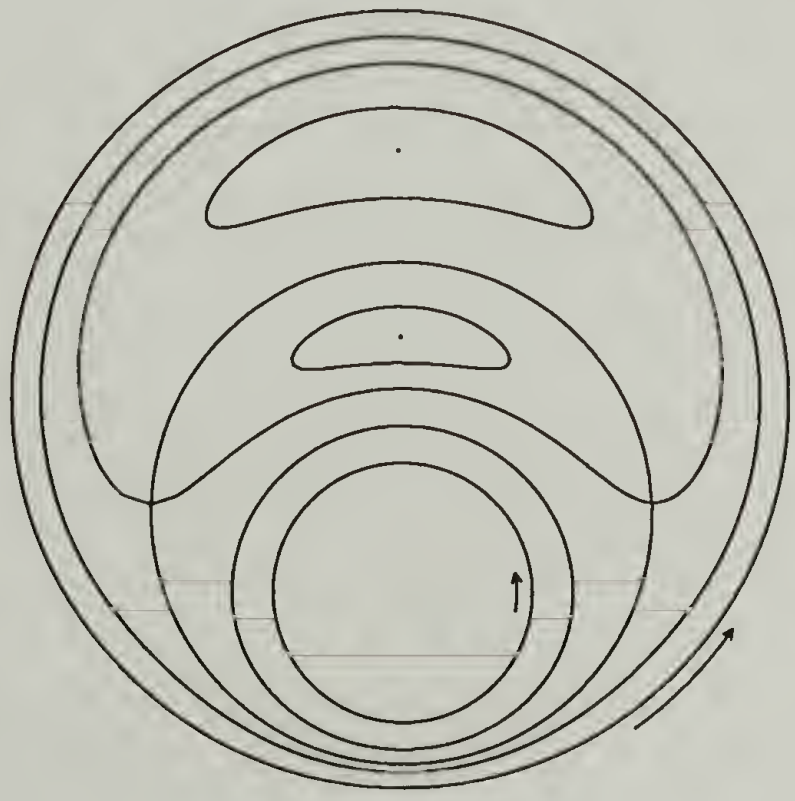

(g)

Figure 2.6: continued.

previous section and so we might expect to find chaos developing in a manner similar to pendulum. On the other hand the co-rotating flow has no stationary points; the streamlines are just circles.

Since the problem is linear, the stream function can be written as a sum of terms due to the motion of the inner and outer cylinders:

$$\Psi(x,y) = \Psi_{in}(x,y)v_{in} + \Psi_{out}(x,y)v_{out}, \tag{2.11}$$

where v_{in} and v_{out} are the angular speeds of the cylinders. Alternatively, if both cylinders are in motion one of the velocities can be divided out, recasting the equations in this form:

$$\frac{\Psi(x,y)}{v_{out}} = \Psi_{in}(x,y)\Omega + \Psi_{out}(x,y), \tag{2.12}$$

where $\Omega = v_{in}/v_{out}$. Note that the steady flow is completely determined by the two geometric parameters, r and e, and Ω. The velocity field is derived from the stream function according to equation 2.1. Since there is an analytic expression for the velocity field, the equations of motion are a pair of coupled ordinary differential equations. The mixing in the flow is determined by the integrated velocity field (the so-called motion). Dividing these equation 2.1 by the velocity of the outer cylinder and setting $d\theta = v_{out}dt$ the equations of motion become:

$$\frac{dx}{d\theta} = -\frac{\Psi/v_{out}}{\partial y}; \; \frac{dy}{d\theta} = \frac{\Psi/v_{out}}{\partial x}; \tag{2.13}$$

Physically, θ is the angular displacement of the outer cylinder and it is clear from this last equation that the position of a fluid element is dependent on the *displacement* θ

of the cylinders and not the actual velocity. When periodic motion of the boundaries is described in the next section this fact will be used to determine the parameter chosen to characterize the period.

2.3 Boundary Motion

A two dimensional Hamiltonian system cannot be chaotic. Therefore, we must add another dimension to the system if there is to be any possibility of chaos. The geometry fixes the number of spatial dimensions so in order to make the system chaotic it must be made time dependent. Strictly speaking when the system is made time dependent there is no longer an exact solution for the velocity field. However, we make a pseudo steady state assumption such that at any instant in time the velocity field is given by the instantaneous velocities of the inner and outer cylinders. In this case the stream function can be written:

$$\Psi(x,y,t) = \Psi_{in}(x,y)v_{in}(t) + \Psi_{out}(x,y)v_{out}(t) \tag{2.14}$$

where $\Psi_{in}(x,y)$ and $\Psi_{out}(x,y)$ are the steady state stream functions due to motion of the inner and outer cylinders respectively [6]. To further simplify the problem we will only consider periodic motion of the boundaries, i.e. the boundary velocities have the property:

$$v_{in}(t) \;=\; v_{in}(t+T)$$

$$v_{out}(t) = v_{out}(t+T) \tag{2.15}$$

where T is the period.

The addition of an explicit time dependence increases the dimension of the system to three; however, as was described in section 2.1, the problem can be reduced to a two dimensional map. When the motion is made periodic the flow is characterized by a new parameter in addition to the parameters which describe the steady flow. Initially it may appear that this new parameter should be T from equation 2.15. However, in the last section we learned that the displacements rather than the actual velocities determined the motion in the system. If T is the time required for the motions of the inner and outer cylinders to repeat themselves (throughout this work the inner and outer cylinders will complete each period of motion at the same time) then the rotation of the inner and outer cylinders during a period is:

$$\theta_{in} = \int_0^T v_{in}(t)dt \tag{2.16}$$

$$\theta_{out} = \int_0^T v_{out}(t)dt$$

Both θ_{in} and θ_{out} need to be specified to fully define the periodic boundary motion. In order to make the connection with the underlying steady flow obvious we choose

to use the parameters

$$\Omega = \frac{\theta_{in}}{\theta_{out}} \tag{2.17}$$

$$\theta \equiv \theta_{out} \tag{2.18}$$

rather than θ_{in} and θ_{out}. In this case Ω is the ratio of the average velocities of the inner and outer cylinders and the steady flow is recovered in the limit of θ going to zero.

There are three periodic waveforms used in this work to generate the cylinder motion; the square wave, the sine wave, and the sawtooth wave. If the average velocities are given by:

$$\begin{aligned} \overline{v}_{in} &= \frac{\theta_{in}}{T} \\ \\ \overline{v}_{out} &= \frac{\theta_{out}}{T} \end{aligned} \tag{2.19}$$

the waveforms obey the following equations:

square wave:

$$v_{in} = \begin{cases} \overline{v}_{in}(1+\epsilon) & 0 \le t < T/4 \\ \overline{v}_{in}(1-\epsilon) & T/4 \le t < 3T/4 \\ \overline{v}_{in}(1+\epsilon) & 3T/4 \le t < T \end{cases}$$

$$v_{out} = \begin{cases} \overline{v}_{out}(1-\epsilon) & 0 \le t < T/4 \\ \overline{v}_{out}(1+\epsilon) & T/4 \le t < 3T/4 \\ \overline{v}_{out}(1-\epsilon) & 3T/4 \le t < T \end{cases} \tag{2.20}$$

sine wave:

$$v_{in} = \overline{v}_{in}(1+\epsilon\cos\frac{2\pi t}{T})$$

$$v_{out} = \overline{v}_{out}(1-\epsilon\cos\frac{2\pi t}{T}) \tag{2.21}$$

sawtooth wave:

$$v_{in} = \begin{cases} \overline{v}_{in}(1-\epsilon(4t/T-1) & 0 \le t < T/2 \\ \overline{v}_{in}(1+\epsilon(4t/T-3) & T/2 \le t < T \end{cases}$$

$$v_{out} = \begin{cases} \overline{v}_{in}(1+\epsilon(4t/T-1) & 0 \le t < T/2 \\ \overline{v}_{in}(1-\epsilon(4t/T-3) & T/2 \le t < T \end{cases} \tag{2.22}$$

The waveforms are shown graphically in figure 2.7. Most of the results presented

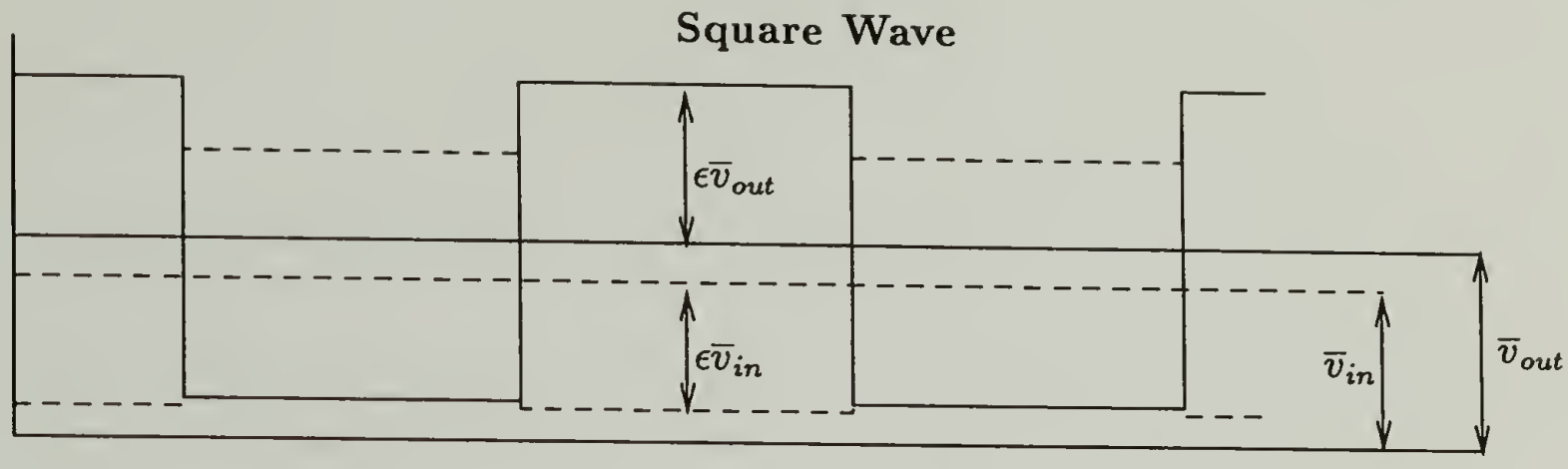

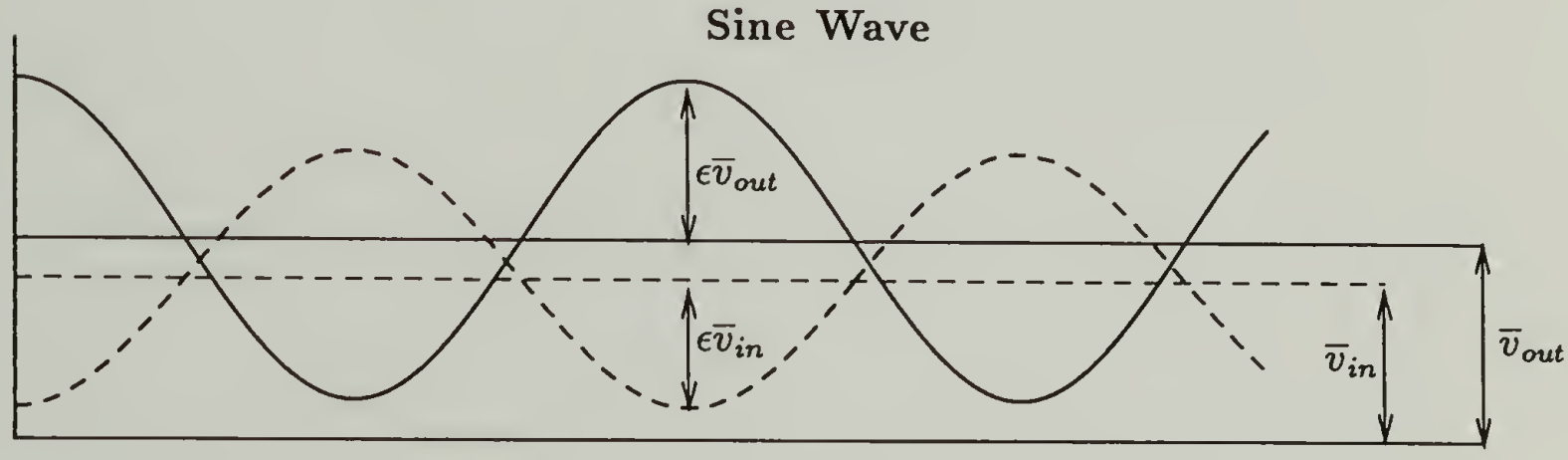

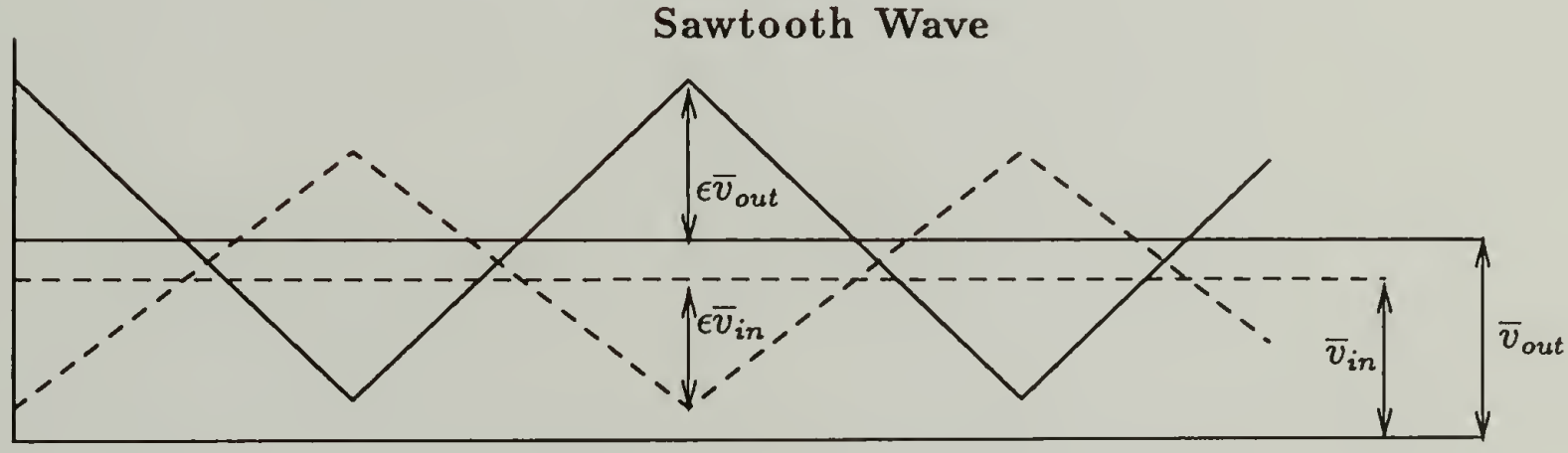

Figure 2.7: Waveforms used to move the inner and outer cylinders.

in this work use the square wave with $\epsilon = 1.0$. In this case the cylinder motions are discontinuous and this simplifies the experiments. It also slightly simplifies the computations. For this protocol the actual wave form of the cylinder velocities is unimportant (provided creeping flow conditions, low Reynolds and Strouhal numbers, are always met). Only their *displacements* affect the results.

The straightforward discontinuous velocity protocol moves one cylinder for its periodic displacement and then move the other for its periodic displacement. Such a protocol was used by [3, 4, 6]. However, the mapping that results from this motion is not symmetric[3] and makes the analyses unnecessarily complicated. If instead of moving the first cylinder its entire displacement per period we initially move it one half of its displacement per period, then move the other cylinder for its periodic displacement, and finally move the first cylinder for the other half of its displacement per period, the resulting map will be symmetric about the line formed by the centers of the two cylinders. A symmetric map simplifies the implementation of several of the methods of analysis, most notably the search for periodic points.

[3]For the journal bearing the motion is symmetric if running the flow forward and reflecting across the line of symmetry (the line running through the centers of the two cylinders) is equivalent to running the flow backward (see [23] for a thorough discussion).

CHAPTER 3

EXPERIMENTS

One of the main factors in choosing to study chaotic mixing the journal bearing flow is that it is a real flow i.e. it can be created experimentally. Building an apparatus consisting of two eccentric cylinders is quite simple. However when the constraints of visualizing the entire flow domain and rotating the cylinders independently according to an arbitrary waveform are added the construction of an apparatus requires a degree of ingenuity.

This chapter describes the experimental aspects of this work. First a description of the apparatus is given followed by a description of the method used to generate the arbitrary (within the limits of the motors) motion of the cylinders. Then the steady flow in the apparatus is compared to the Stokes flow solution. Finally, the results of the chaotic mixing experiments are shown.

3.1 Apparatus

The experimental apparatus was designed in order to accomplish two key objectives. The first is to be able to rotate the inner and outer cylinders independently and at variable speeds according to some arbitrary wave form. The second goal is to be able to view, without obstruction, the entire flow domain. The first objective

is relatively easy to implement; the second objective requires some forethought to implement owing to constraints created by the first objective. However, with the help of a machine designer, Mr. Ed O'brien, we have fabricated an apparatus which meets both of the key objectives.

The experimental system is shown schematically in figure 3.1 and a photograph of the apparatus is shown in figure 3.2. The key element of the design resides in the outer cylinder. The outer cylinder is a stainless steel tube which is 15 *cm* long and has a 15 *cm* inner diameter. Two large bearings fix the cylinder to the frame of the apparatus while a large gear is used to rotate it. The bearings and the gear are all attached to the outer surface of the cylinder so that there is a clear view through the interior of this cylinder. The inner cylinder is a solid cylinder also 15 *cm* long with a 5 *cm* diameter and is connected to an arm extending over the top of the outer cylinder. The arm is attached to the frame with bolts in slotted holes such that the inner cylinder can be positioned anywhere within the outer cylinder. The bottom of the outer cylinder is sealed with a glass plate thereby allowing the flow domain to be viewed from the bottom of the apparatus as well as the top. If the flow is viewed from the top there will be an obstruction caused by the arm which holds the inner cylinder (see figure 3.1(a)). However, the view from the bottom is completely unobstructed and consequently no information is lost when recording experiments on film.

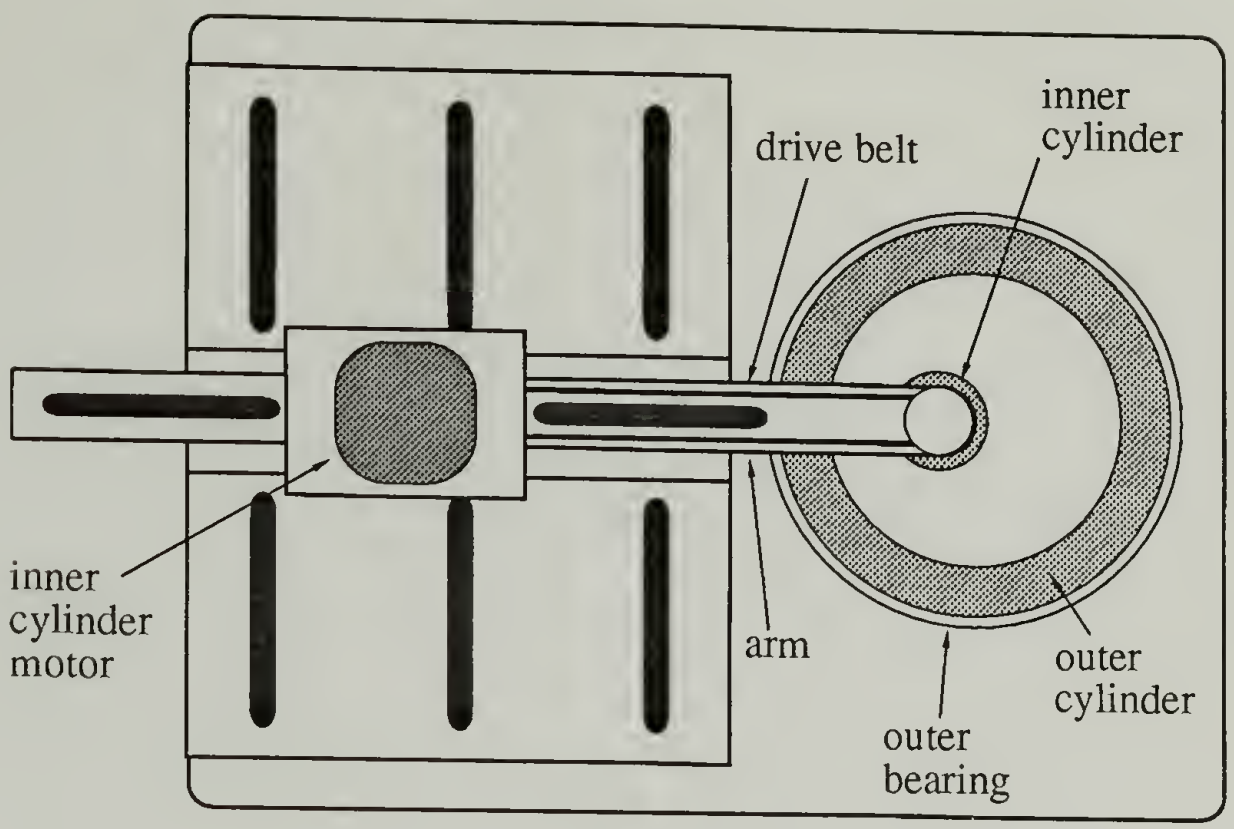

(a)

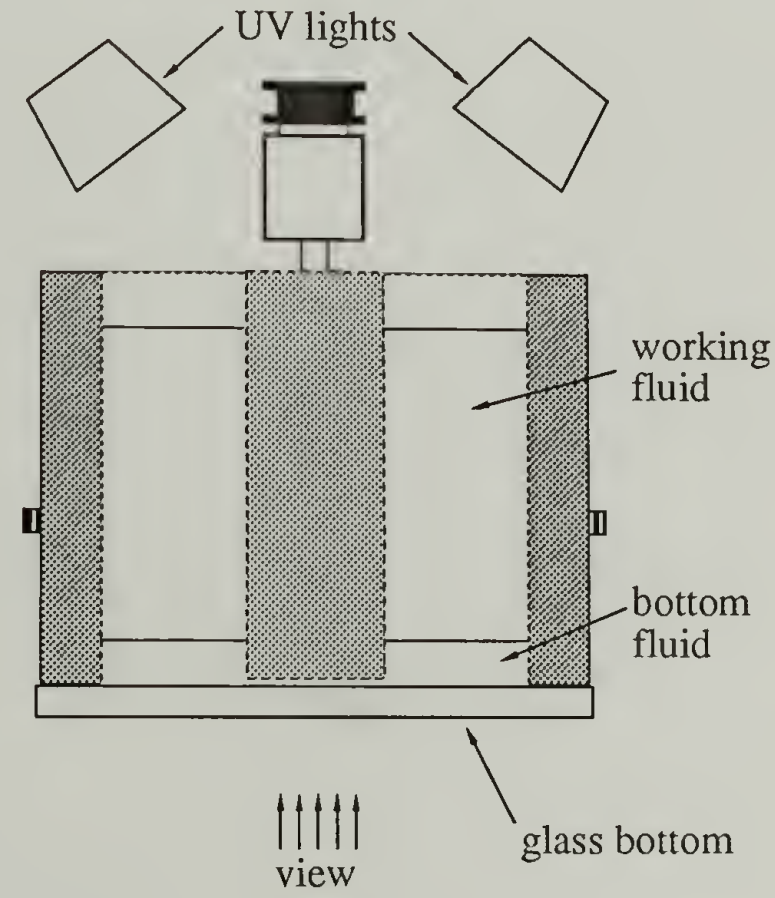

(b)

Figure 3.1: Schematics for the journal bearing apparatus. Part (a) is the view from the top , (b) a cutaway view of the flow region, and (c) is the view from the side.

Continued, next page.

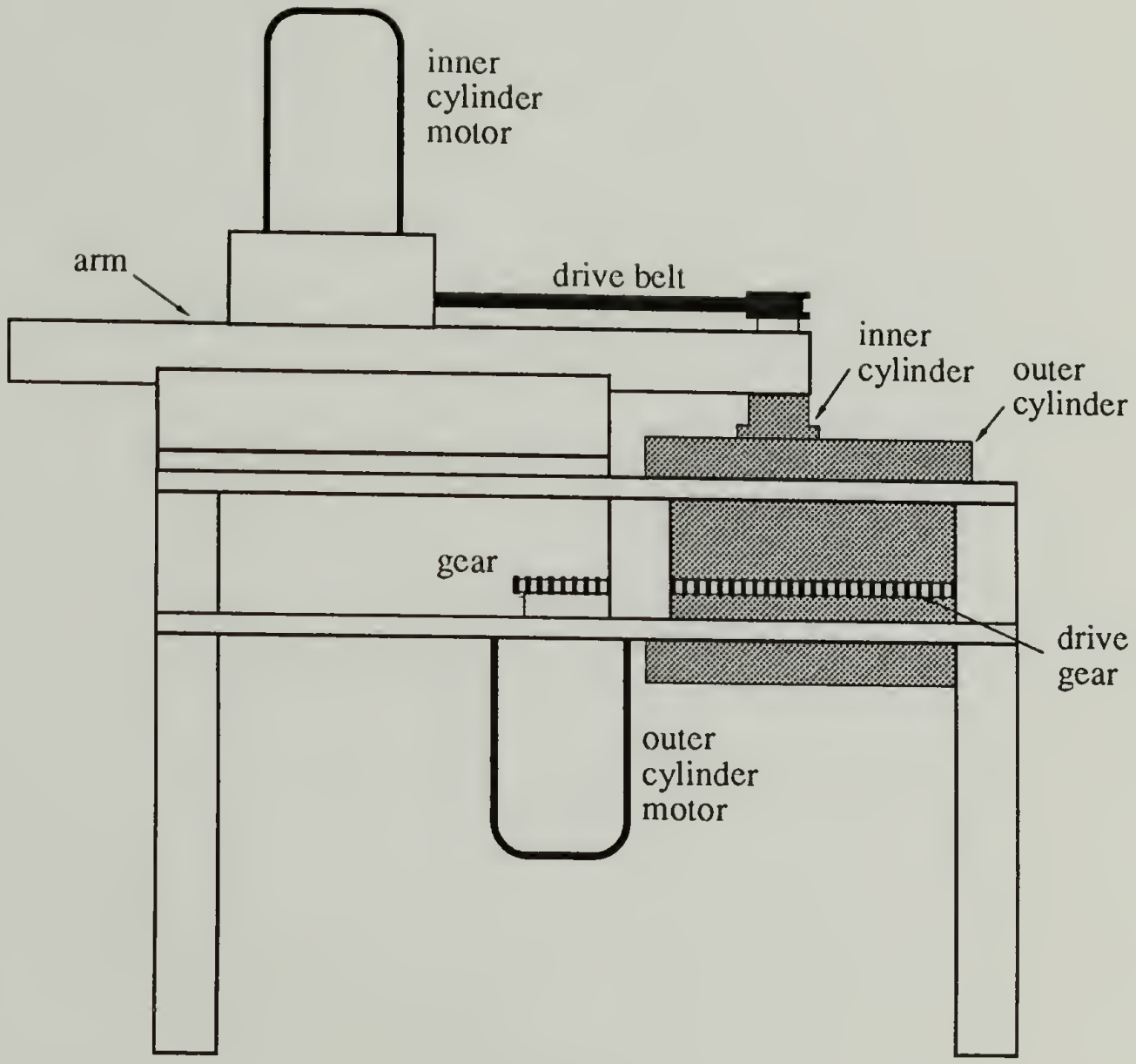

(c)

Figure 3.1: continued

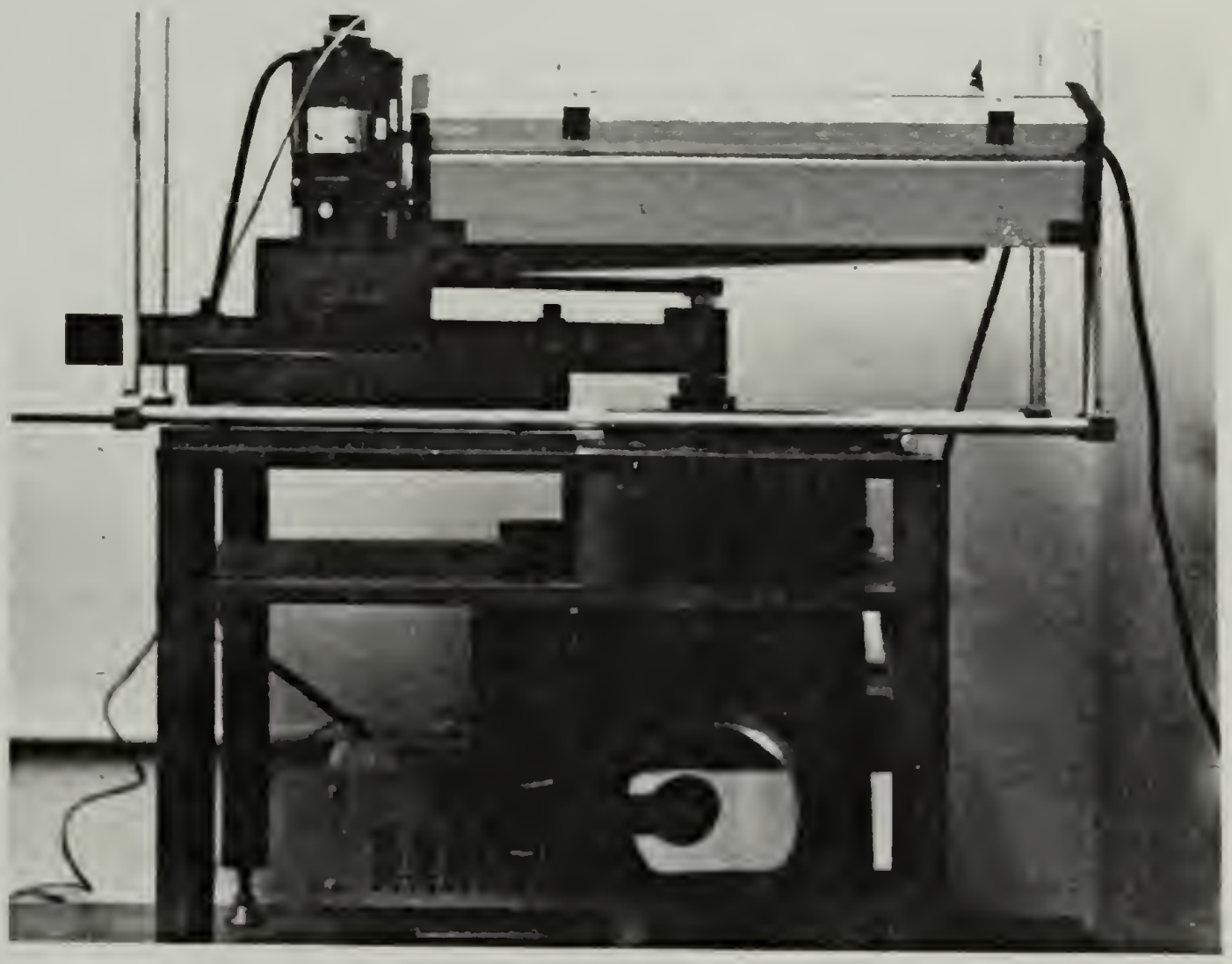

Figure 3.2: Photograph of the experimental apparatus.

The cylinders are rotated by identical motors; Bodine NSH-11D5. The inner cylinder is driven with a timing belt whereas the outer cylinder is driven directly through gears. The gearing of the two cylinders is such that their linear velocities have nearly identical ranges. Tachometers are attached to the motors to monitor their speeds and allow feedback control. The motors are controlled by PC's LIMITED 286 personal computer with a DSP-16 Data Acquisition Processor board from Ariel Corp.

The working fluid is glycerin which has a viscosity of approximately 7 poise and a density of 1.2 g/cm^3. This results in a Reynolds number of 0.8 and a Strouhal number ranging from 0.2 to 0.026 where the length scale is based on the difference in radii of the two cylinders, the velocity scale is based on the sum of the speeds of the cylinders and the characteristic time is the period of the perturbation. The cylinders are only 15 cm deep so in order to eliminate bottom effects the glycerin is floated on a 2 cm thick layer of 1-Iodo-3- methylbutane which has a viscosity of approximately 1-cp and a density of $1.5 g/cm^3$ or FOMBLIN Y-L VAC 06/6 vacuum pump oil which has a density of 1.88 g/cm^3. The upper surface of the glycerin is open to the atmosphere. Experiments have verified that the flow in the glycerin is independent of depth. Therefore the bottom effects are confined to the bottom organic layer and the effects of the upper free surface are negligible.

The basic experiments are performed by marking a region of the flow with a fluorescent dye (Cole-Parmer; type J295-05) dissolved in glycerin and observing how this region deforms when subjected to a specified velocity protocol. The properties of the glycerin with and without the fluorescent dye are nearly identical so effects due to viscosity difference and surface tension can be ignored (in other related work we magnify the effects of surface tension to study drop breakup in chaotic flows). Also, the diffusion coefficient of the dye is quite small ($10^{-8} cm^2/s$) so the spreading of the dye shown in the results is strictly due to convection. To get maximum contrast between the marked and unmarked fluid the flow region is illuminated with long-wave UV light and all visible sources of light are removed. In addition, a UV filter is used on the camera to eliminate any direct UV light. With this technique the dye is highly visible. However, the glycerine also fluoresces slightly blue. This can be eliminated with additional filters but it is useful to allow the glycerine to be seen so that the flow domain is clearly visible.

The experimental results are recorded on color slide film; a picture of the flow region is taken after every period. The film used is Fujichrome ISO 100 color slide film. For the pictures in this thesis black and white prints were made from the color slides. In order to make the prints the color slides were duplicated on to Kodak TMAX ISO 100 black and white print film. The negatives were then printed on

Kodak Polycontrast III RC black and white print paper. For color pictures the color slides were printed directly onto Cibachrome AII color print paper.

3.2 Creation and Control of the Cylinder Motion

The DSP-16 Data Acquisition Processor is actually an entire computer albeit a highly specialized one (see [24] for a thorough description). It has its own microprocessor and memory as well as the analog to digital and digital to analog converters needed to control and drive the motors. The board is geared toward performing digital signal processing with an emphasis on audio digital signal processing. While this is not the function we need the board to perform, there are several features of the board which are particularly applicable to our motor control problem. First, the board has two channels of input and two channels of output to handle stereo sound. This is convenient since we have two motors to independently control. Second, the board is designed to output signals of arbitrary wave forms. This is quite useful for this work since we can easily conduct experiments with any of the waveforms we have explored computationally. And third useful feature is that the AD and DA converters are 16 bit converters resulting in high accuracy both in generating and measuring the motion of the cylinders.

The cylinder velocities are created in the following manner: First the computer approximates the desired waveform by generating a look-up table of values which

are to be converted into voltage and output every 0.01 seconds by the DSP-16. This table is then down loaded to the DSP-16. The microprocessor on the DSP-16 has been programmed to send the wave form to a D/A converter which in turn outputs a voltage to the controller of the appropriate motor. At the same time the motor speeds are determined from the tachometers and converted to digital values and stored on the DSP-16 board for possible later retrieval. These values are also summed to give the total displacement of each cylinder. The entire waveforms are then multiplied by the ratios of desired displacements to actual displacements (the DSP-16 board does this extremely quickly). This results in a simple proportional control scheme. Since the time lag in the control is so great (a whole period) it is useful only in providing the desired rotation of the cylinders and correcting for drift due to fluctuations in the line voltage. However, adjusting the speed of the motors to cause the proper cylinder rotation is the major difficulty in the control so this simple proportional control scheme is more than adequate.

3.3 Steady Flow

Before the experimental results from the time periodic flows are presented we will first verify that the steady flow created experimentally agrees with Wannier's solution for the stream function. Figure 3.3 shows streamlines generated by placing a line of dyed fluid along the symmetry line. When the steady flow is turned on the

(a)

(b)

(c)

(d)

Figure 3.3: Steady state line deformation experiements depicting streamlines in the eccentric cylinder apparatus. For all pictures the ratio of the radii is 1/3. For parts (a)-(d) $e = 0.3$ and for parts (e)-(g) $e = 0.5$. The cylinder velocities are: (a) $v_{out} = 0$, (b) $v_{in} = 0$, (c) $v_{in} = -v_{out}$, (d) $v_{in} = v_{out}$, (e) $v_{out} = 0$, (f) $v_{in} = 0$, and (g) $v_{in} = 3v_{out}$.

Continued, next page.

(e)

(f)

(g)

Figure 3.3: continued.

line of dyed fluid begins to deform according to the streamlines of the flow. In time the dyed line will have deformed until it is nearly coincident with the streamlines. We call these experiments *streamline experiments.*

Figure 3.3 (a)-(d) shows streamlines experiments for $e = 0.3$. The pattern generated when only the inner cylinder is rotated is shown in (a). Similarly (b) shows the case when only the outer cylinder is rotated, (c) shows the pattern when the cylinders are counter rotating with identical linear velocities, and (d) shows the patterns when the cylinders are co-rotating with identical linear velocities. Parts (e)-(g) show streamlines for $e = 0.5$. When these results are compared to the streamlines of the analytical solution shown in figure 2.6 the match is excellent. The only possible discrepancy is the location of the hyperbolic point in the counter-rotating flow (figures 2.6(c) and 3.3(c)) but this is due to optics and not the flow field. Since we view the flow from below, the bottom of the inner cylinder is closer to the camera than the dyed region of fluid and so it will appear to be slightly larger than it really is.

3.4 Time-Periodic Flow

When the motion of the boundaries is made time periodic the flow has a good chance of exhibiting chaotic behavior. We expect the size and shape of the chaotic regions to depend on the flow parameters. As a result, the time periodic flows will

display a much greater range of behavior than the steady flow. We cannot hope to explore all possible behavior in these flows but instead we will present the some of the most significant differences (or, in the case of waveforms, similarities) in the flows.

Figure 3.4 shows the results of deformation experiments where the initial dyed region is located arbitrarily somewhere in the chaotic region[1]. The exact initial location of the drop has no noticeable effect on the results of figure 3.4 provided it is placed in the chaotic region. All the experiments correspond to $r = \frac{1}{3}$, $e = 0.3$, and $\Omega = -3.0$, and to the counter-rotating discontinuous velocity protocol. The only parameter varied is θ, the amount that the cylinders are rotated per period. The values of θ vary from 90° to 720° by increments of 90°.

It is apparent from visual inspection that the amount of area covered by the dye increases with increasing period. This may at first glance appear to violate the area preserving character of the flow. However, this effect is mainly due to high concentration of the dye. As it stretches it appears to maintain a constant fluorescent intensity even though its concentration is decreasing. There is also an effect due to parallax. Since the dye is a three dimensional object it must have some depth. Initially the dye is spherical so there is no parallax. However, as the experiment proceeds the dye is stretched into a narrow ribbon. After a few periods the width of the dye ribbon is (in general) several orders of magnitude less than

[1]Chaotic according to the Poincaré section.

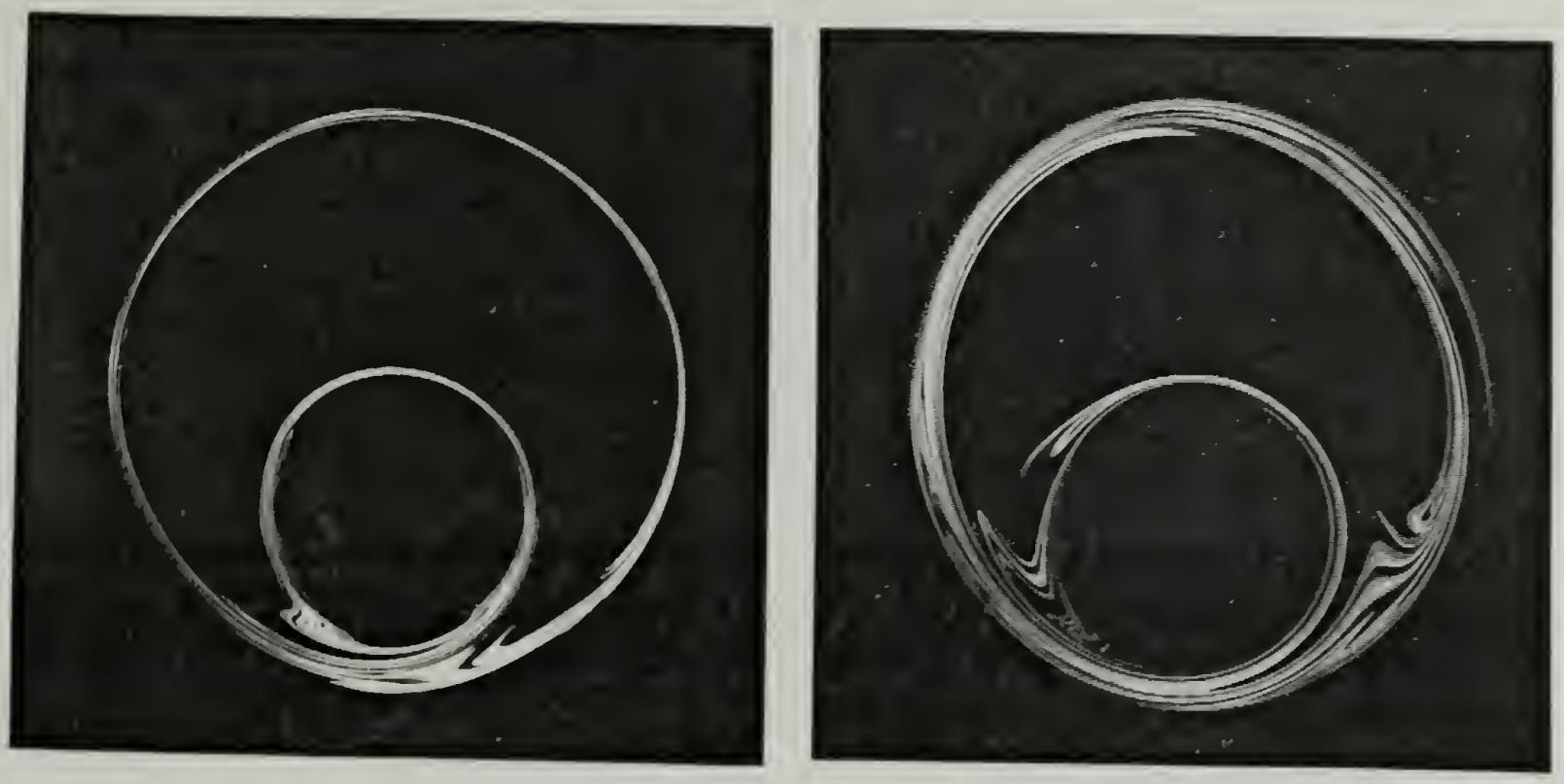

(a) (b)

(c) (d)

Figure 3.4: Deformation experiments for the counter-rotating discontinuous velocity protocol with values of θ ranging from 90° to 720°. The remaining parameters are held constant at $e = 0.3$, $r = 1/3$, and $\Omega = -3.0$. (a) $\theta = 90°$, (b) $\theta = 180°$, (c) $\theta = 270°$, (d) $\theta = 360°$, (e) $\theta = 450°$, (f) $\theta = 540°$, (g) $\theta = 630°$, (h) $\theta = 720°$. (a)-(g) Deformation after 10 periods, (h) deformation after 5 periods.

Continued, next page.

(e)

(f)

(g)

(h)

Figure 3.4: continued.

the depth. Viewing such a ribbon from a finite distance results in an apparent width greater that the actual width. As the dye is stretched the width observed is due to viewing the striations from a position slightly off vertical. This is an unavoidable drawback of the photography. However, these effects can be used to our advantage. This apparent area increase can be measured, thereby providing a quantitative measure of the mixing in the flow (independent measurements of the perimeter and area are proportional for area coverages of less that 50%, [25]). We should also explain that the pictures in figure 3.4 represent an apparent steady state in the mixing process; if the number of periods is increased the large scale aspects of the figures, folds and islands, are nearly unchanged. Obviously it is not a true steady state since the dye will diffuse throughout the entire flow domain. Rather it is a crossover from convection-dominated mixing to diffusion-dominated mixing. In the time scale of our experiments diffusion is unimportant and so the flows appear to be in steady state.

At $\theta = 90°$ the dye spreads over a small region corresponding to the location of the separatrixes for the unperturbed flow. At $\theta = 180°$ the shape of the region which the dye has spread over is identical to $\theta = 90°$ but it is now approximately twice as thick. However, when θ is increased to 270° there is a significant increase in the area coverage. The shape of the chaotic region has also been greatly altered. For $\theta = 90°$ and $\theta = 180°$ there was a single large regular region in the middle of

the flow domain. At $\theta = 270°$ this central island has disappeared. Instead there are two smaller islands, one above the other, on the line of symmetry. It is clear that at $\theta = 270°$ there is something fundamentally different from the previous values of θ.

When θ is increased to 360° the picture becomes similar to $\theta = 90°$ and 180° again; the two islands have disappeared and been replaced by one large central island. The total amount of area that the dye spreads over also appears to have decreased slightly from $\theta = 270°$. At $\theta = 450°$ there is still a central island which is devoid of dye, however it does not appear to have evolved from the $\theta = 360°$ island; it is not centered anywhere near the expected location. Instead it looks as if part of the regular region which was previously next to the outer wall brakes away and is moving in to the chaotic region. At the same time the previous central island has disappeared. This new island continues to shrink in size as θ goes through 540° and 630°. Finally at 720° the only regular region is a thin strip next to the outer wall.

Several other aspects of the problem are worthy of note. The first is the dependence of the behavior near the outer cylinder on the rotation of the outer cylinder. There must always be a regular region next to the outer cylinder, although it may be quite thin, because at some, perhaps infinitesimal, distance from the wall the rotation of the inner cylinder will have a negligible effect on the flow (the same holds true for the effects of the outer cylinder next to the inner wall). But the thickness of this region varies greatly depending on the rotation of the outer cylinder and

does not precisely follow the simple rule that larger period creates more chaos and consequently smaller regular regions. Rather, the key parameter seems to be the 'phase' of the outer cylinder (how close it is to an integer number of rotations per period). For the periods of $\theta = 360°$ and $\theta = 720°$ the outer cylinder moves exactly one and two revolutions per period respectively. Notice that the regular region next to the wall is thicker for these periods than for the periods immediately preceding and following them.

Another aspect is the evolution of the striations and folds as the period is increased. We have stated that the macroscopic picture does not change in a continuous fashion i.e. the region that the dye spreads over does not evolve in a 'linear' fashion with the changing period. However, if we adopt a different viewpoint of the mixing process and focus on the folding and nesting pattern of the dye striations then the pictures do seem to change in a continuous manner; each fold 'folds more' as the period of the perturbation is increased. Each folding pattern can be thought of as local event, affecting its immediate neighborhood. The folds of a particular pattern will propagate through the flow until they 'collide' with the folds of a different pattern. The global picture is then determined by how folds of different patterns are able to fit together. If the folds fit together well the dye will spread over a large region and the chaotic region is large. If the folds start approaching each other at blunt angles there will be gaps where no dye can penetrate; these gaps are the

regular regions. The sizes of the regular islands are determined by the misfit of the folds.

We now turn our attention to the results of moving the cylinders co-rotationally rather than counter-rotationally. It is not clear *a priori* exactly how the time dependent co-rotating flow will behave. We expect that the results should be qualitatively different since the underlying unperturbed flows (streamline patterns 2.6(c) and (d)) are qualitatively different. This is in contrast to the counter-rotating flow where the results, at least for small θ, could have been predicted based on our knowledge of what happens to a manifold when a system is perturbed.

Figure 3.5 shows experimental mixing results for co-rotation of the cylinders according to a discontinuous velocity protocol. The experimental procedure is the same as the one used to produce the results shown in figure 3.4. The flow parameters are $r = 1/3$, $e = 0.3$, and $\Omega = 3.0$. Note that, except for Ω these parameters are identical to those of figure 3.4. The four values of θ used are 180°, 270°, 360°, and 450°. It is apparent that the chaotic region is much larger in the co-rotating flows than in the equivalent counter-rotating flows. In fact, it is difficult to discern any island structures at all in the co-rotating flows. The difference between the co- and counter-rotating results when $\theta = 180°$ (figure 3.5(a) and figure 3.4(b)) is particularly large. For the counter-rotating flow a very large island exists in the middle of the flow whereas in the co-rotating flow the dye is excluded only from a

(a)

(b)

(c)

(d)

Figure 3.5: Deformation experiments for the co-rotating discontinuous velocity protocol with values of θ ranging from 180° to 450°. The remaining parameters are held constant at $e = 0.3$, $r = 1/3$, and $\Omega = 3.0$. (a) $\theta = 180°$, (b) $\theta = 270°$, (c) $\theta = 360°$, (d) $\theta = 450°$. (a) Deformation after 20 periods, (b)-(d) deformation after 10 periods.

strip next to the outer cylinder. As with the counter-rotating flows, the striation patterns in the co-rotating flows appear to evolve in a continuous fashion as θ is increased; each fold of dye observed in the picture for a particular value of θ exists in a sharpened and stretched form in the picture for the next larger value of θ. The mixing in the co-rotating flow for values of $\theta > 450°$ continues to be completely chaotic.

One aspect of mixing in the co-rotating flow worthy of note is the way in which the dye initially evolves. For the first few periods of an experiment the dye stretches very little. Then, all of a sudden, the stretching rate becomes quite large. It is as if there is an induction time before the mixing begins to be effective. As a consequence, even though the dye spreads over a larger region of the flow domain for the co-rotating case, the rate of mixing is relatively slower than for counter-rotation. This is evident from the period number of the results in figure 3.5. The picture corresponding to $\theta = 180°$ was taken after 20 periods of mixing. The dye had spread to an area only half as large after 10 periods. For $\theta = 270°$ the results shown are for 10 periods of mixing but there are still fairly large regions void of dye which will eventually contain dyed fluid. One possible explanation for the apparent induction time existing in the co-rotational and not the counter-rotational flows is that in order for the dye to be stretched it needs to pass near a hyperbolic periodic point with large eigenvalues. There are only one or two such points for small θ. Since

the chaotic region is much larger in the co-rotational flow than in the corresponding counter-rotational flow, the dyed fluid will take, on average, longer in the co-rotating flows to get near the hyperbolic periodic points responsible for rapid stretching.

One last variable we look at experimentally is the effect of the waveform on the mixing. Up to this point the results have been for a discontinuous velocity protocol. We now want to explore the consequences of using some different waveforms. There are two new waveforms we will look at, a sine wave and a sawtooth wave (see section 2.3), in addition to the square wave (discontinuous velocity protocol). Figure 3.6 shows the results of dye deformation experiments for the three waveforms for $\theta = 180°, 270°, 360°$. The remaining parameters are $r = 1/3$, $e = 0.3$, and $\Omega = -3.0$. surprisingly, the results for two of the three values of θ (180° and 360°) are very similar. This is even more surprising since the waveforms produce fairly different pictures for the intermediate value of $\theta = 270°$. Undoubtedly a bifurcation takes place near $\theta = 270°$ causing a rapid change in the behavior of the flow. It is quite possible that the results from the three waveforms are more similar even at $\theta = 270°$ than it may at first appear. This will be discussed in greater detail in section 5.2.

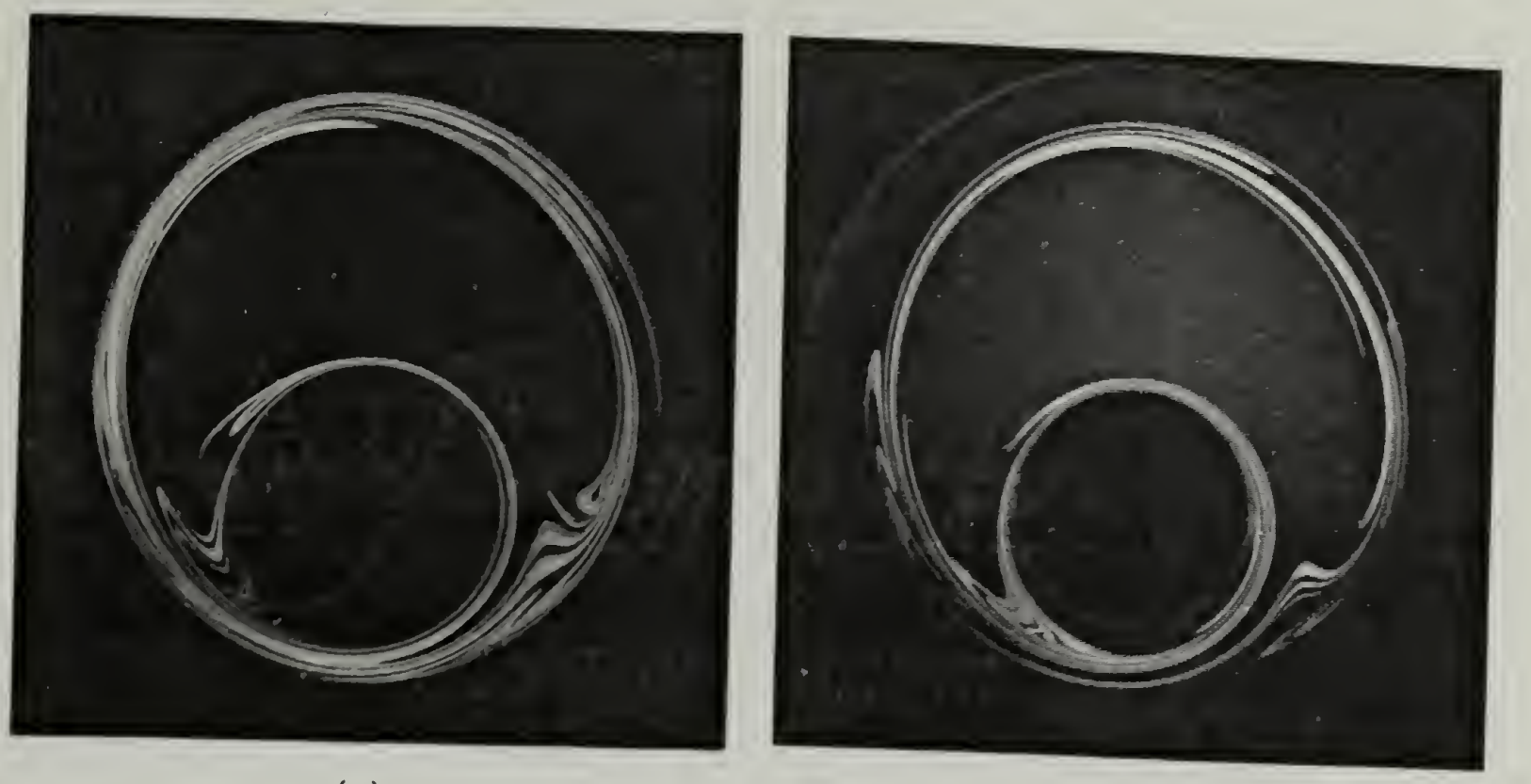

(a) (b)

(c)

Figure 3.6: Deformation experiments for the square, sine, and sawtooth waveforms in a counter-rotating mode of operation. The parameters held constant are $e = 0.3$, $r = 1/3$, and $\Omega = -3.0$ and all experiments are run for 10 periods. (a)-(c) $\theta = 180°$, (d)-(f) $\theta = 270°$, (g)-(i) $\theta = 360°$. (a),(d),(g) square wave; (b),(e),(h) sine wave; (c),(f),(i) sawtooth wave.

Continued, next page.

(d)

(e)

(f)

Figure 3.6: continued.

Continued, next page.

(g)

(h)

(i)

Figure 3.6: continued.

CHAPTER 4

METHODS OF ANALYSIS

In this chapter we examine several methods of analysis for chaotic flows with the goal of determining their usefulness to the study of mixing. Some of these methods come from, or are inspired by, dynamical systems theory while another (stretching) is a method of our own devising. Since the focus of this chapter is to determine the value of these techniques, the number of flow parameters used will be limited. However, the results of this chapter will be applicable to the majority of flow conditions in the journal bearing as well as a majority of two dimensional flows in general.

Throughout the remainder of the thesis the velocity field will be treated as though it can be analytically integrated to give the motion of any point in the flow domain. However, this is not the case; the velocity field must be integrated numerically. Therefore, the numerical method used to integrate the velocity field is briefly discussed here. In the flow domain the stream function and its derivatives are extremely well behaved so virtually any integrator can be used to integrate the velocity field. The one we use is the Bulirsch-Stoer method as given in [26]. This method is quite effective in integrating functions as smooth as the velocity field in the eccentric cylinder flow. All computations are performed in double precision (64 bit floating point numbers). The Bulirsch-Stoer method uses an adaptive step size

which is set by specifying the maximum allowable truncation error. The acceptable truncation error is set at 10^{-10} where the truncation error is determined from the difference in the results produced by successively smaller (and therefore more accurate) step sizes. In the case of the stretching plots the acceptable truncation error is set at 10^{-5} in order to facilitate faster computations.

4.1 Poincaré Sections

A carefully constructed Poincaré section shows the long time behavior of trajectories of all initial conditions. In a typical Poincaré section (e.g. figure 4.1) we see that a trajectory has one of two distinct types of behavior. With the first type of behavior all of the points of a trajectory lie on a smooth surface. This is the type of behavior that one expects from unperturbed Hamiltonian systems so it is usually referred to as a 'regular' trajectory. With the second type of behavior the points of a trajectory are scattered throughout some area of the Poincaré section. There is no apparent structure to the trajectory with this type of behavior (although this is in part due to some shortcomings of Poincaré sections), and so it is called 'chaotic'.

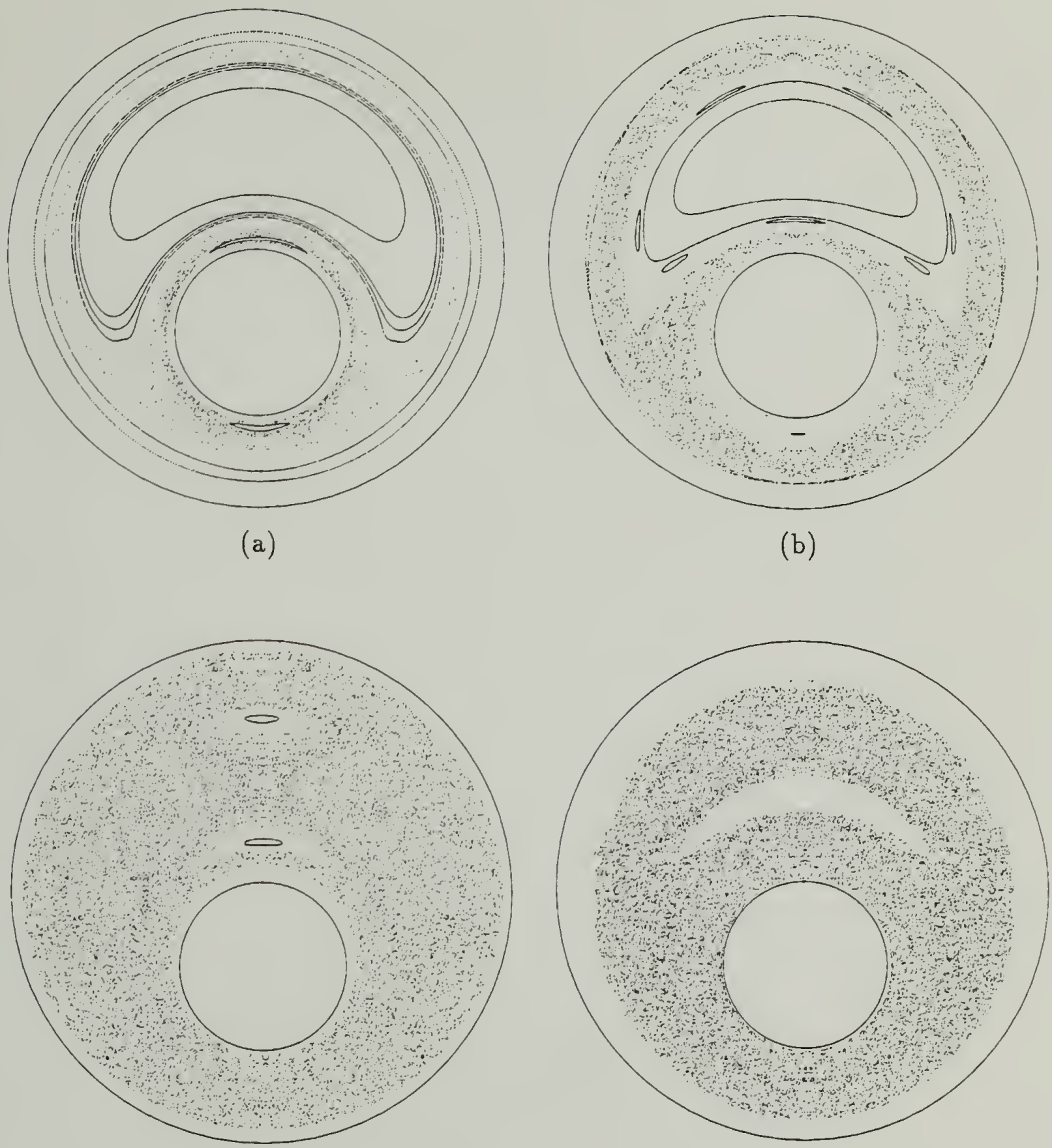

Figure 4.1: Poincaré sections for counter-rotating square wave flow. Flow parameters are $e = 0.3$, $r = 1/3$ and $\Omega = -3.0$ throughout and (a) $\theta = 90°$, (b) $\theta = 180°$, (c) $\theta = 270°$, (d) $\theta = 360°$, (e) $\theta = 450°$, (f) $\theta = 540°$, (g) $\theta = 630°$, (h) $\theta = 720°$.

Continued, next page.

(e)

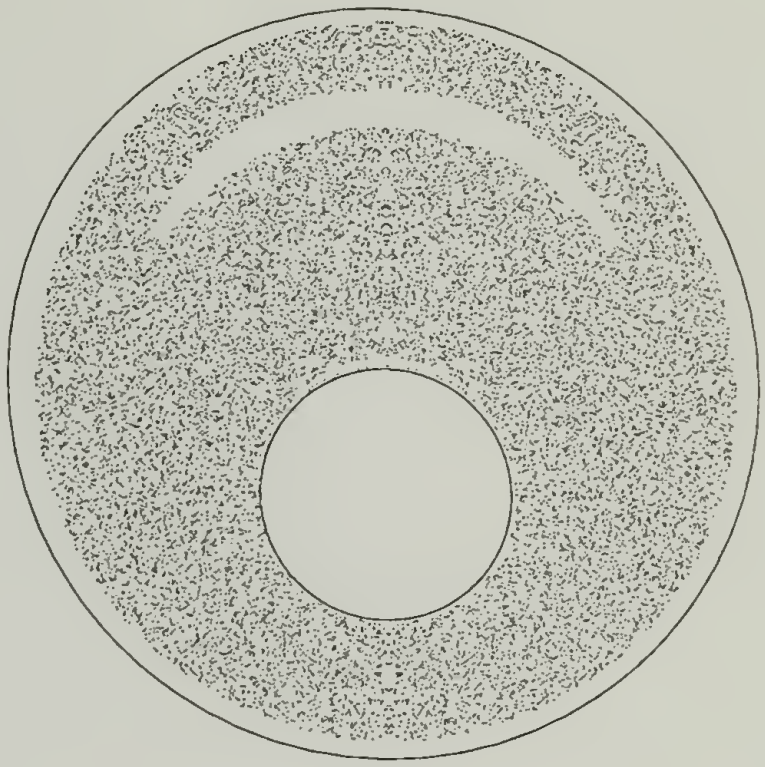

(f)

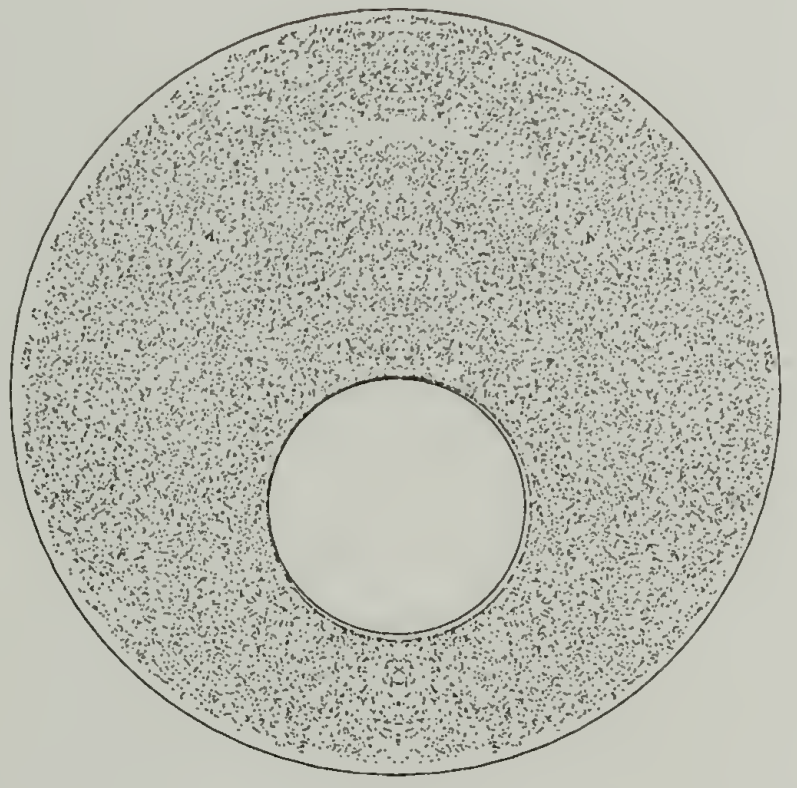

(g)

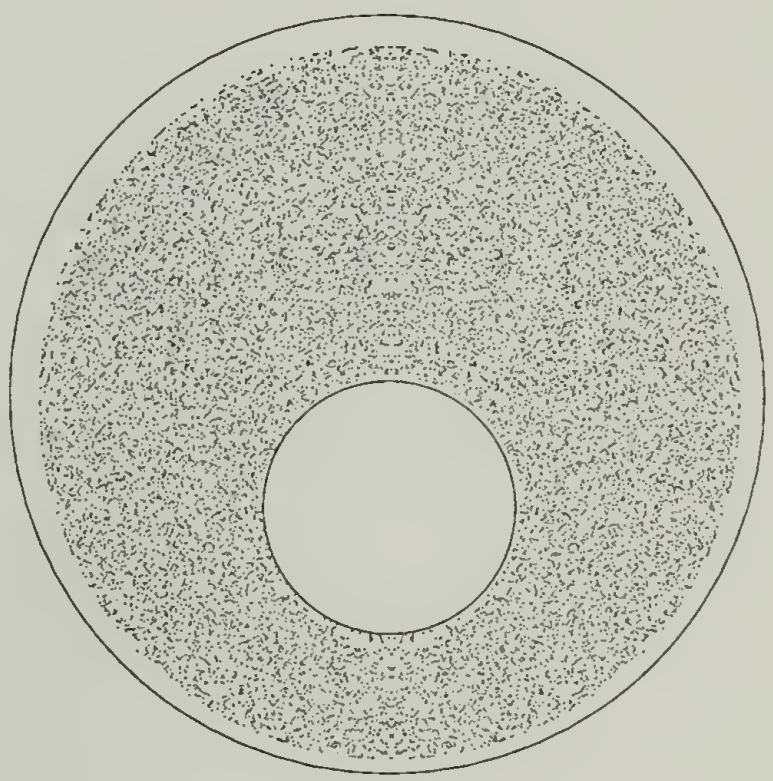

(h)

Figure 4.1: continued.

4.1.1 Agreement Between Poincaré sections and Experiments

Figure 4.1 shows the Poincaré sections with values of θ from 90° to 720°. The other parameters are $e = 0.3$, $r = 1/3$, $\Omega = -3.0$ and they are held constant. Comparing the Poincaré sections to the experiments shown in figure 3.4 we see that for all eight values of θ the region which the dye spreads over is completely contained in the chaotic regions of the Poincaré sections. However, the converse is not true; the dye does not completely cover the chaotic region of the Poincaré section. This is due to the much lower number of periods in the experiments (10 or fewer) compared to the Poincaré sections (1000+ periods). In theory if one ran an experiment for as many periods as the Poincaré section the dye should spread out over the entire chaotic region. In practice it is not feasible, or in fact useful, to run an experiment for so many periods. The goal is to characterize the mixing ability of a flow. Therefore we are interested in the behavior after just a few periods (order of magnitude 10). The question we must answer is 'what can the Poincaré section tell us about the short time behavior of the system?' A Poincaré section does not give precise information about where a particular set of initial conditions (such as a drop of dye) will go but the Poincaré section shows regions where initial conditions are forbidden from entering regardless of how many periods the experiment is run. If dye is placed in the chaotic region it will not go into any regular regions. If dye is

placed in a regular region it stays within the regular region (experience tells us that a blob placed in a regular region stretches very little) and never enters the chaotic regions or other regular regions.

4.1.2 Drawbacks

Hindered Communication

Incorrect analysis can result if the Poincaré section data are not properly examined. Generally Poincaré sections are shown with trajectories of many initial conditions on the same plot. Since the plots are usually done in black and white there is no way to differentiate between the trajectories (points) corresponding to different initial conditions. Since regular orbits tend to appear as closed curves each initial condition in a regular region will have its own distinct orbit and therefore is difficult to misinterpret. However, chaotic orbits show up as a haze of points scattered over an area. Parts of a chaotic region can have hindered communication with other parts of the chaotic region. In a Poincaré section made with several different initial conditions on the same plot it is not possible to differentiate between chaotic regions where all initial conditions sample the entire region in a uniform manner and chaotic regions where initial conditions can get trapped in a subspace of the chaotic region for some length of time. The amount of time that a trajectory spends in such a subspace determines the extent to which the communication is 'hindered'.

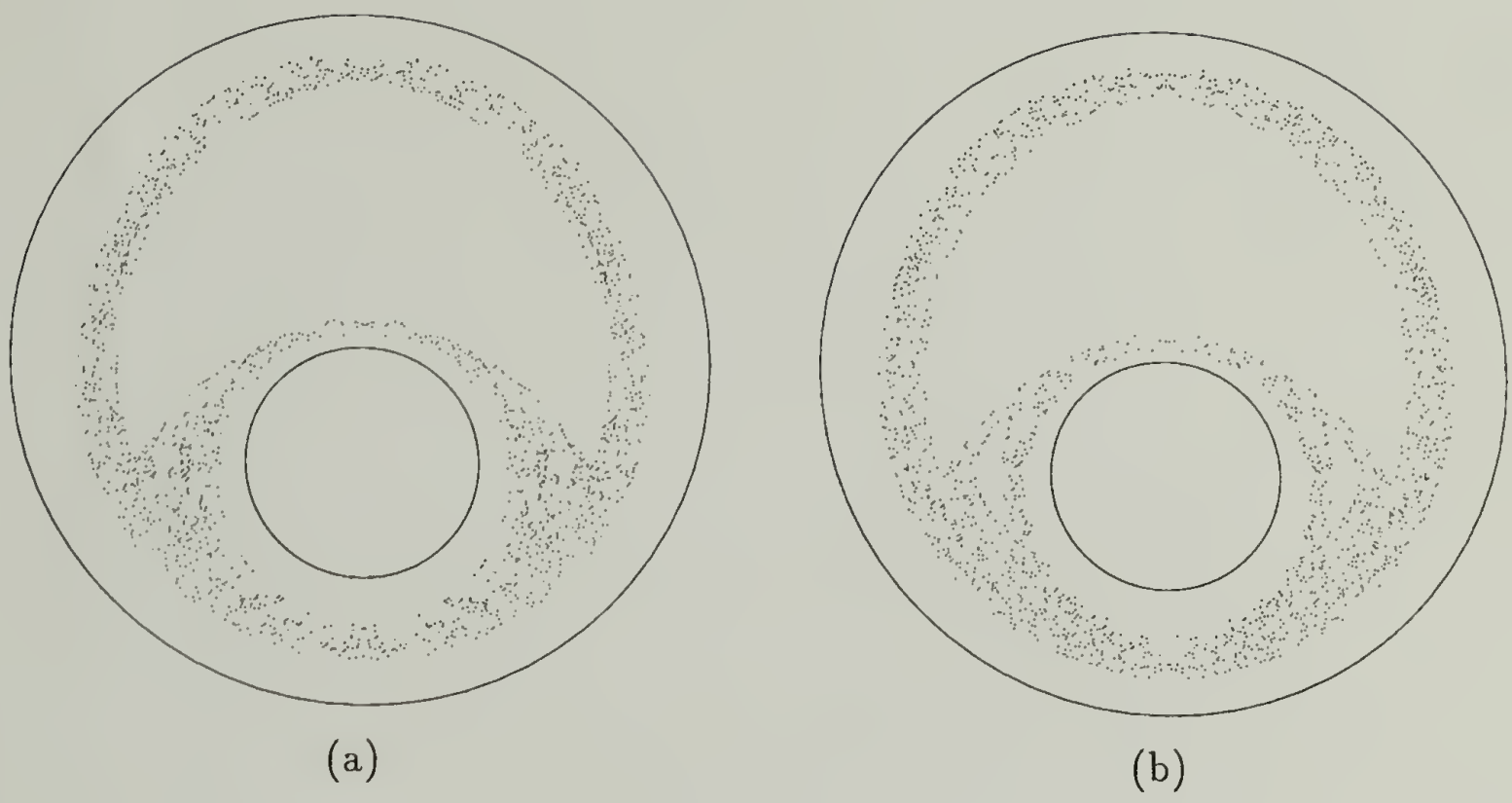

Figure 4.2: Non-homogeneity in the chaotic region.

An example is given in figure 4.2. Figures 4.2 (a) and (b) are individual trajectories in the chaotic region of figure 4.1(b) which corresponds to $\theta = 180°$. Careful examination reveals that there are regions of high concentration of points on either side of the inner cylinder in figure 4.2(a) whereas these same regions are devoid of any points in figure 4.2(b). When they are combined, as in figure 4.1(b), the chaotic region appears uniformly covered by the trajectories.

For some applications hindered communication between different parts of a chaotic region may be unimportant. However, for mixing we are interested in short time behavior and in this case barriers which only hinder communication on a long time scale may keep regions completely separate for the time scale we are interested

in. Therefore it is imperative that the Poincaré section data are properly analyzed. This can be accomplished in one of two ways. The first is to look at the Poincaré section of each initial condition separately as is done in figure 4.2. Any non-uniformity in the chaotic regions will become obvious. A better way of doing this if one has the luxury of some sort of color graphics device is to give each initial condition its own color. Non-uniformities in chaotic regions can be spotted easily in such color plots.

Bifurcation in Central Island

Conversely, not every type of behavior in a Poincaré section has a useful meaning in terms of mixing. For example, figure 4.3 shows the bifurcation and appearance of a chain of period 4 islands in the central period-one island. The size of the period 4 islands grows very quickly with a very small change in θ (from 149° to 150°). This might lead to the belief that small inaccuracies in our control of the experiment can lead to very large changes in the mixing picture. However, figure 4.4 clearly demonstrates that this is not the case. The figure shows the evolution of a line consisting of two colors, red and white, placed through the center of the regular region. The colors show the orientation of the line and demonstrate that the line rotates with a period of approximately 4 (it would be difficult to differentiate between period 2 rotation and period 4 if the line were made of just one color). Further insight can be gained because the tip of the red segment was placed in the chaotic region. This provides a dramatic contrast between behavior in the regular

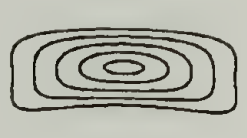

(a)

(b)

(c)

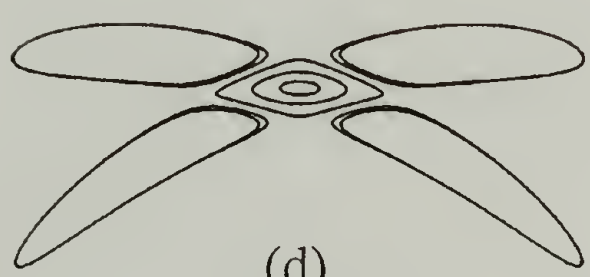

(d)

(e)

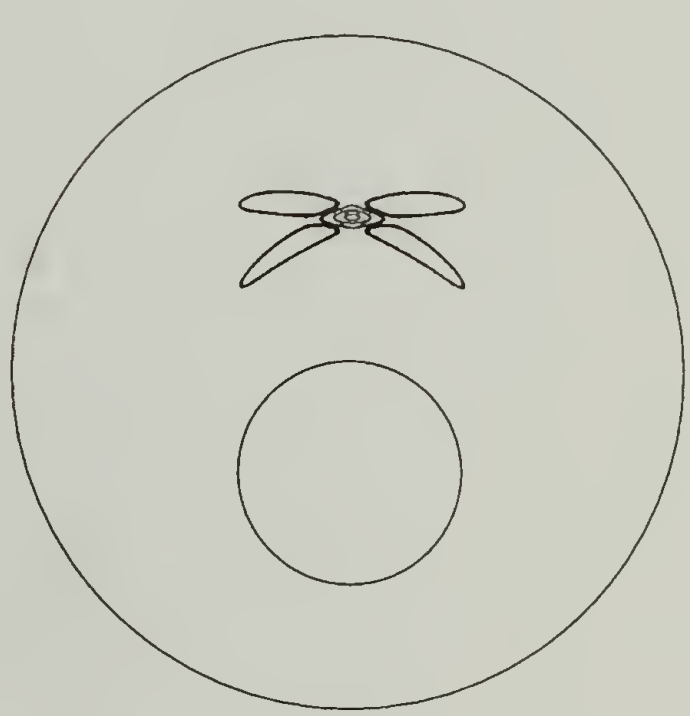

(f)

Figure 4.3: The appearance of period 4 orbits in the center island.

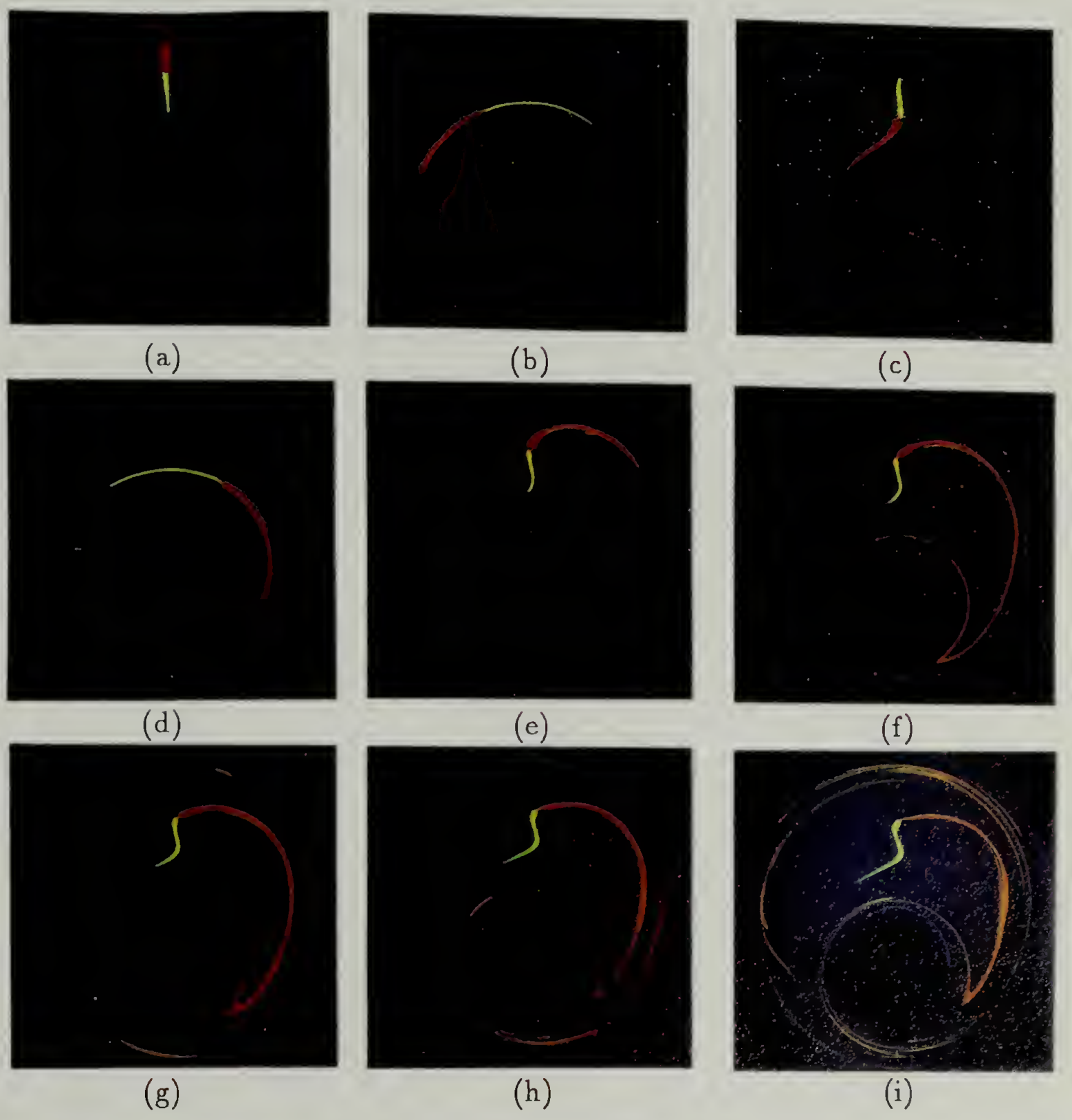

Figure 4.4: Experiment demonstrating the near solid body rotation in the regular region and the difference in stretching between the regular and chaotic regions. Part (a) shows the initial placement of the two colored filament, (b)-(e) show periods 1, 2, 3, 4 respectively, and (f)-(i) show periods 8, 12, 16, 20.

and chaotic regions. The portion of the line in the central island tends to move as a solid body, stretching very little even after twenty periods. The portion of the line in the chaotic region behaves in a substantially different manner. It stretches and folds after a few periods, elongating to many times its initial length after twenty periods.

The conclusion is that the period four islands which appear in the central island have a long time scale associated with them (it can take more than 1000 periods to make one rotation about some of the orbits of the period 4 islands) and therefore the dramatic changes seen in the Poincaré sections will only be seen experimentally at very high periods. Since we are interested in mixing, long time behavior is unimportant and so this behavior in the central island is unimportant. Further analysis of the regular regions for different parameter conditions support the conclusion that regular regions do not mix (i.e. deform blobs of dye). Regular regions can be thought of as dead zones where any dye initially placed in them will stretch very little if at all.

(Lack of) Rate Information

If our ultimate goal is to describe mixing in real applications, rate information is of prime importance. However, it is not possible to determine rate information from Poincaré sections. This flaw is fundamental to Poincaré sections and so it is necessary to develop other methods which can provide this information. Another

area of interest where Poincaré sections provide no information is in describing the shape of the striation patterns, e.g. folds, in a chaotic region. A first step towards both of these objectives is to locate the most important (low order) periodic points of the flow.

4.2 Periodic Points

One can think of finding periodic points as a minimization problem. A periodic point of a map is a solution to the equation

$$\mathbf{f}^n(\mathbf{x}) = \mathbf{x}, \tag{4.1}$$

where $\mathbf{f}^n(\mathbf{x})$ is the nth iteration of the map. The point $\mathbf{x}$ is a period m point if it is a solution to equation 4.1 for $n = m$ but not a solution for any $n < m$. This definition suggests that a straightforward way to find periodic points is to find stationary points of equation 4.1. There are numerous methods which will find solutions to such an equation. A simple method is to define a function

$$d(\mathbf{x}) = \|\mathbf{f}^n(\mathbf{x}) - \mathbf{x}\|^2 \tag{4.2}$$

which has the properties of being positive definite and having global minima at the periodic points. This is a standard idea for locating extrema of a vector field. In the context of a map d has a simple interpretation, it is the distance between a point and its image after n periods. When d is zero the point has been mapped back to

itself and therefore must be a periodic point. To find the zeros of d one can follow its gradient down to a minimum. While in general this method cannot guarantee that the minima found are global minima, the method appears to be quite adequate for our problem (every minimum we have found has been a periodic point).

Without any additional information this method leads to a search for periodic points in two dimensions. However, the symmetry of the mapping places severe restrictions on the locations of periodic points. Period 1 periodic points must mainly fall on the line of symmetry. If a period 1 periodic point was not on the line of symmetry there would have to be a matching period-one periodic point one the other side of the symmetry line and although there is nothing preventing this, it is rarely observed in practice. Therefore, we can find most of the period-one periodic points just by searching the line of symmetry. Thus, we have reduced the two dimensional search to a one dimensional search. Periodic points of higher period must always occur in chains. For example, a period five periodic point must occupy four other positions before it returns to its initial location. The periodic point can only go to these four other positions or uniqueness will be violated. Therefore these four other positions are also periodic points of period five. Together, this set of periodic points forms a 'chain'. We can simplify the search for periodic points of odd period using arguments similar to those given for the period-one case. There is always an unpaired point in an odd chain of periodic points and this point will

almost certainly fall on the line of symmetry. If this point is located we can map it forward enough times to locate the rest of the points in the chain. Thus we can reduce the search for odd period periodic points to just a search of the line of symmetry.

Even-period periodic points present a greater difficulty since it is possible for all members of a chain to lie off of the line of symmetry. However, in many cases points of a chain of even period will lie on the axis of symmetry (there must be an even number of points on the line of symmetry) and in these cases the chain can be found in a manner analogous to the odd period chains. When none of the points lie on the line of symmetry the search for chains of even period periodic points can still be simplified but we must use an additional piece of information to do so. Our mapping is derived from a continuous flow and therefore when a point is moving to its new location during the period it must follow a continuous path. Since chains of even period periodic points lie symmetrically across the line of symmetry there must be a path which crosses the line of symmetry at some intermediate time during the period. It turns out that this intermediate time is exactly half way through the period. Therefore, if we search the line of symmetry at this time we can locate those even period periodic points which never lie on the axis of symmetry after whole periods. Again, the search for periodic points is reduced from two dimensions

to one dimension. This is one of the great benefits of using a mapping which is symmetric.

The character of the periodic point is determined from the eigenvalues of the Jacobian of the mapping $\mathbf{f}^n(\mathbf{x})$ evaluated at the periodic point. Here $\mathbf{f}$ is the same as in equation 4.1 and if the periodic point is period n it is necessary to computed the Jacobian of the n^{th} iteration of the map in order to properly classify the periodic point. Since the map is area preserving the character of the periodic point can be determined from the trace of the Jacobian. If the trace is greater than two the point is hyperbolic and it will stretch nearby fluid elements. If the trace is less than two the point is elliptic and it will tend to rotate nearby fluid elements.

4.2.1 Agreement Between Periodic Points and Poincaré Sections (and Experiments)

Figure 4.5 shows plots of the periodic points superimposed upon the associated Poincaré section. The circles represent elliptic periodic points and the X's represent hyperbolic periodic points. The agreement between the location of the periodic points and the various types of behavior in the Poincaré sections is remarkable. Every island surrounds an elliptic periodic point of the appropriate period. On the other hand, there is very little basis on which to judge the agreement between the hyperbolic periodic points and the Poincaré sections. This is due to an inherent

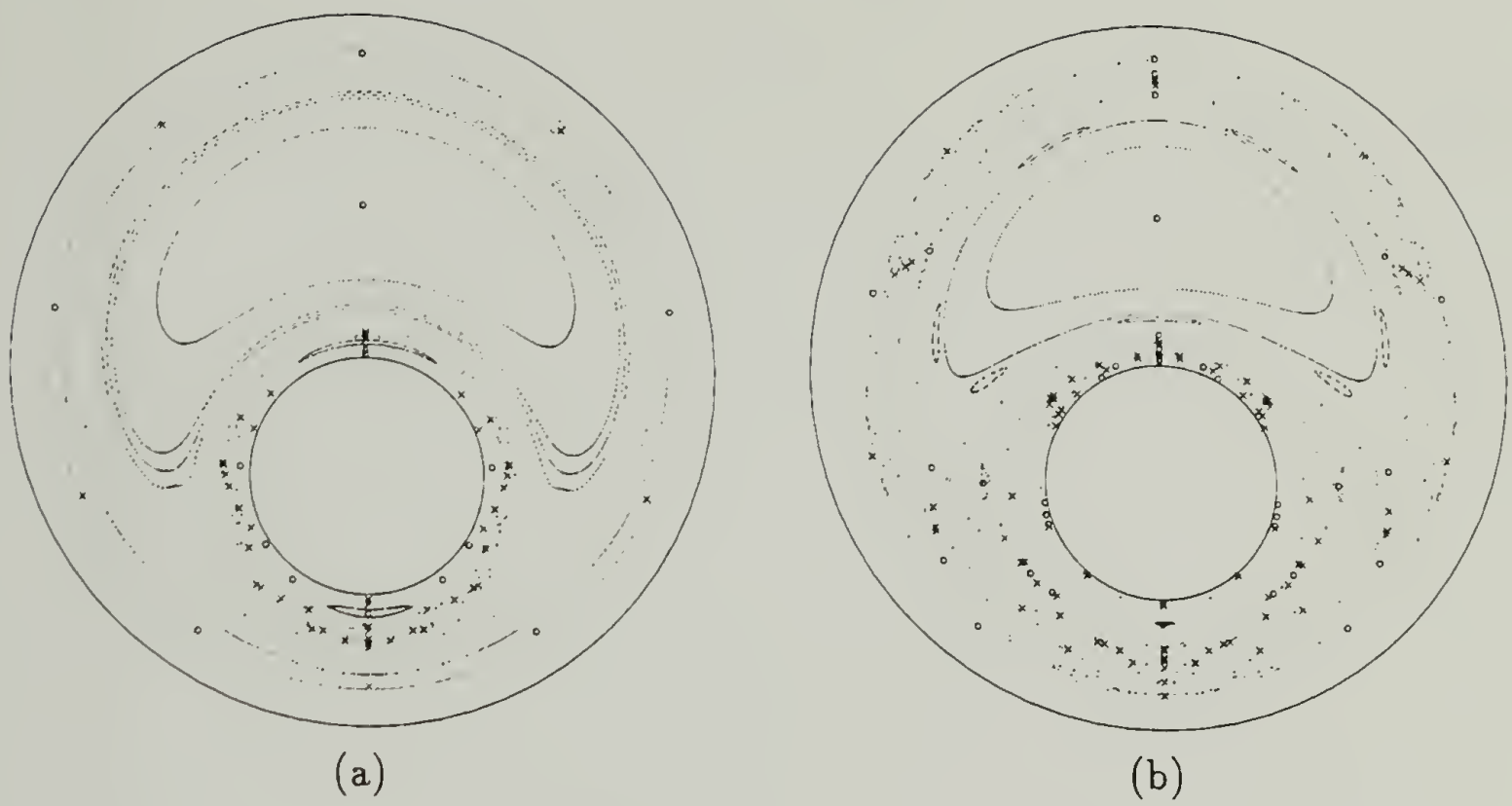

(a) (b) (c) (d)

Figure 4.5: Periodic points up to period 5 for counter-rotating square wave flow. Flow parameters are $e = 0.3$, $r = 1/3$ and $\Omega = -3.0$ throughout and (a) $\theta = 90°$, (b) $\theta = 180°$, (c) $\theta = 270°$, (d) $\theta = 360°$, (e) $\theta = 450°$, (f) $\theta = 540°$, (g) $\theta = 630°$, (h) $\theta = 720°$.

Continued, next page.

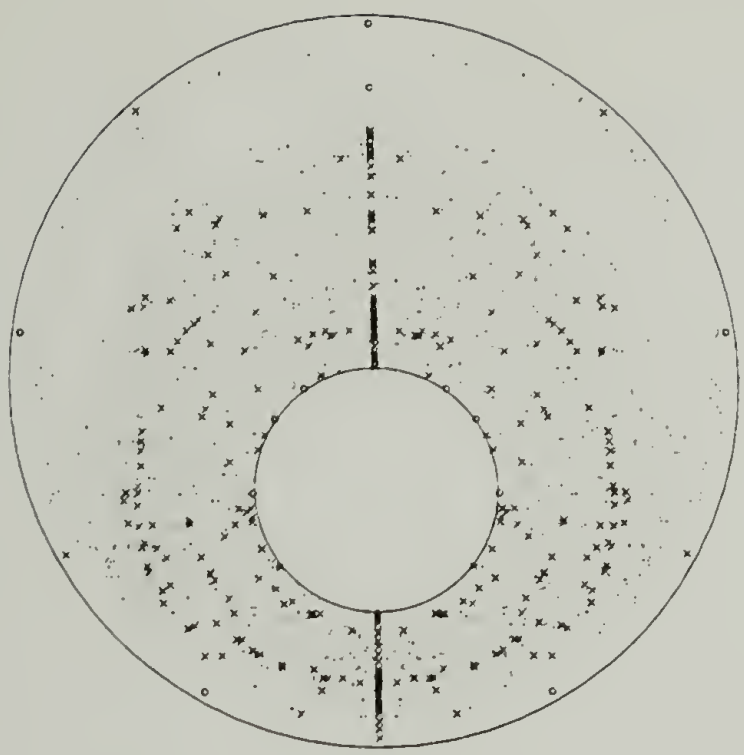

(e)

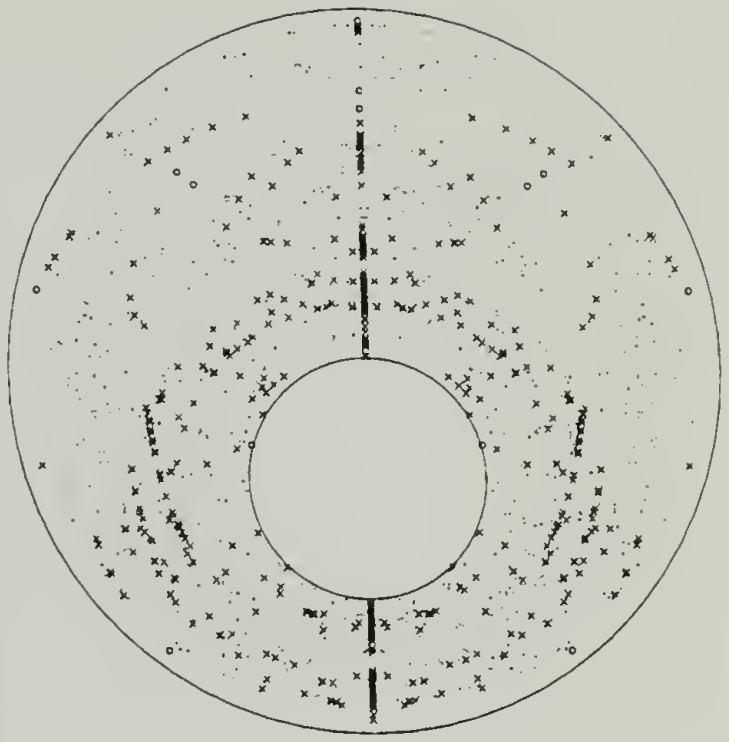

(f)

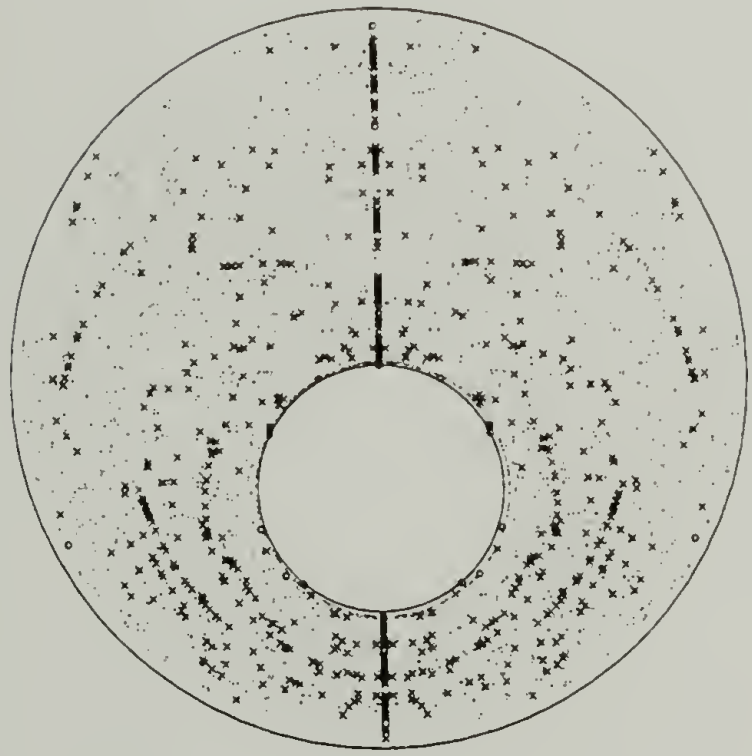

(g)

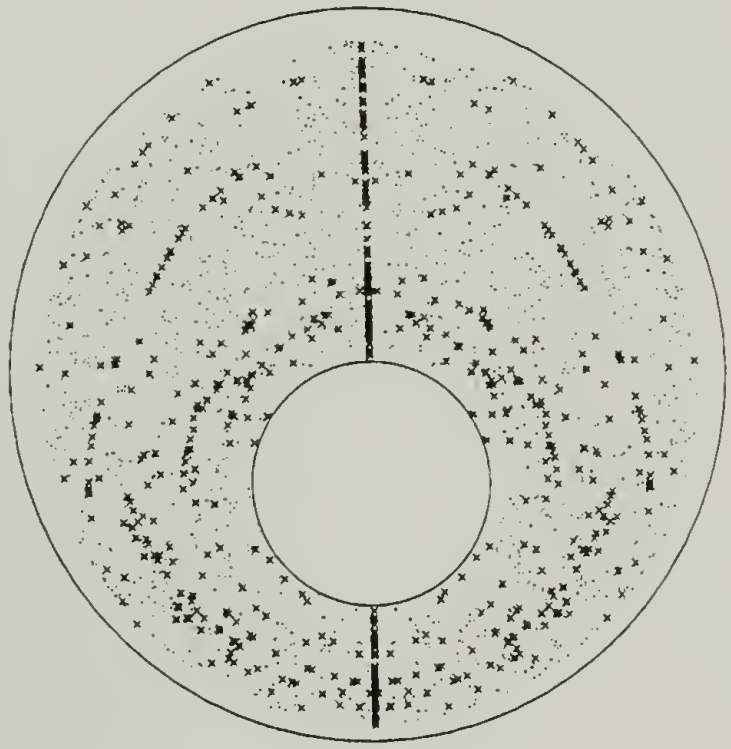

(h)

Figure 4.5: continued.

flaw of Poincaré sections; Poincaré sections give no information on structure in the chaotic regions (experiments do). However, there are instances where comparisons can be made. For the case $\theta = 180°$ there is a chain of period 5 islands with period 5 elliptic points in the middle on the outer edge of the chaotic region. In between these islands there is a chain of period 5 hyperbolic points. This is precisely the type of behavior predicted by the Poincaré-Birkhoff theorem (see for example, [14, p. 169]) which describes the way in which rational orbits break down into sequences of hyperbolic and elliptic periodic points.

4.2.2 Agreement Between Eigendirections of Periodic Points and Striations in Experiments.

There are several things which can be learned directly from the periodic points. The largest eigenvalue (in absolute value) of the mapping, $\mathbf{f}$, evaluated at a hyperbolic periodic point gives an indication of the rate of stretching in the neighborhood of the periodic point. Indeed, the eigenvalue seems to be a reasonable measure of the rate along the entire unstable manifold of the hyperbolic periodic point. Since the manifold tends to stretch through out the entire chaotic region the eigenvalue may give a good indication of the mixing rate throughout the chaotic region. Also, the eigenvalues of a periodic point vary with θ proportionally to the variation of the

mixing rate with θ. This can be used to predict the difference in mixing rate for two values of θ based on the difference in the eigenvalues of a particular periodic point.

We can get an idea of the alignment of the striations in the chaotic region by plotting the eigendirection associated with the maximum (in absolute value) eigenvalue of hyperbolic periodic points. Such plots are shown in figure 4.6. It is clear when comparing figure 4.6 to the experiments shown in figure 3.4 that the eigendirections do give a very good indication of the direction of the striations in the neighborhood of the periodic points. Unfortunately the periodic points are not distributed uniformly throughout the chaotic region. Some areas have a plethora of periodic points whereas other areas are completely void. This makes it impossible to speculate on the complete striation structure so some other method must be used to obtain such a picture.

4.3 Manifolds

The manifolds of the periodic points can be of great use in determining the shape of the dye striations in the chaotic region. In order to find the unstable manifold of a particular hyperbolic periodic point we can simply surround the point with a circle and then 'turn on' the flow. The circle will deform but will always surround a segment of the unstable and stable manifolds. As the number of periods increases the length of the stable manifold surrounded decreases whereas the length

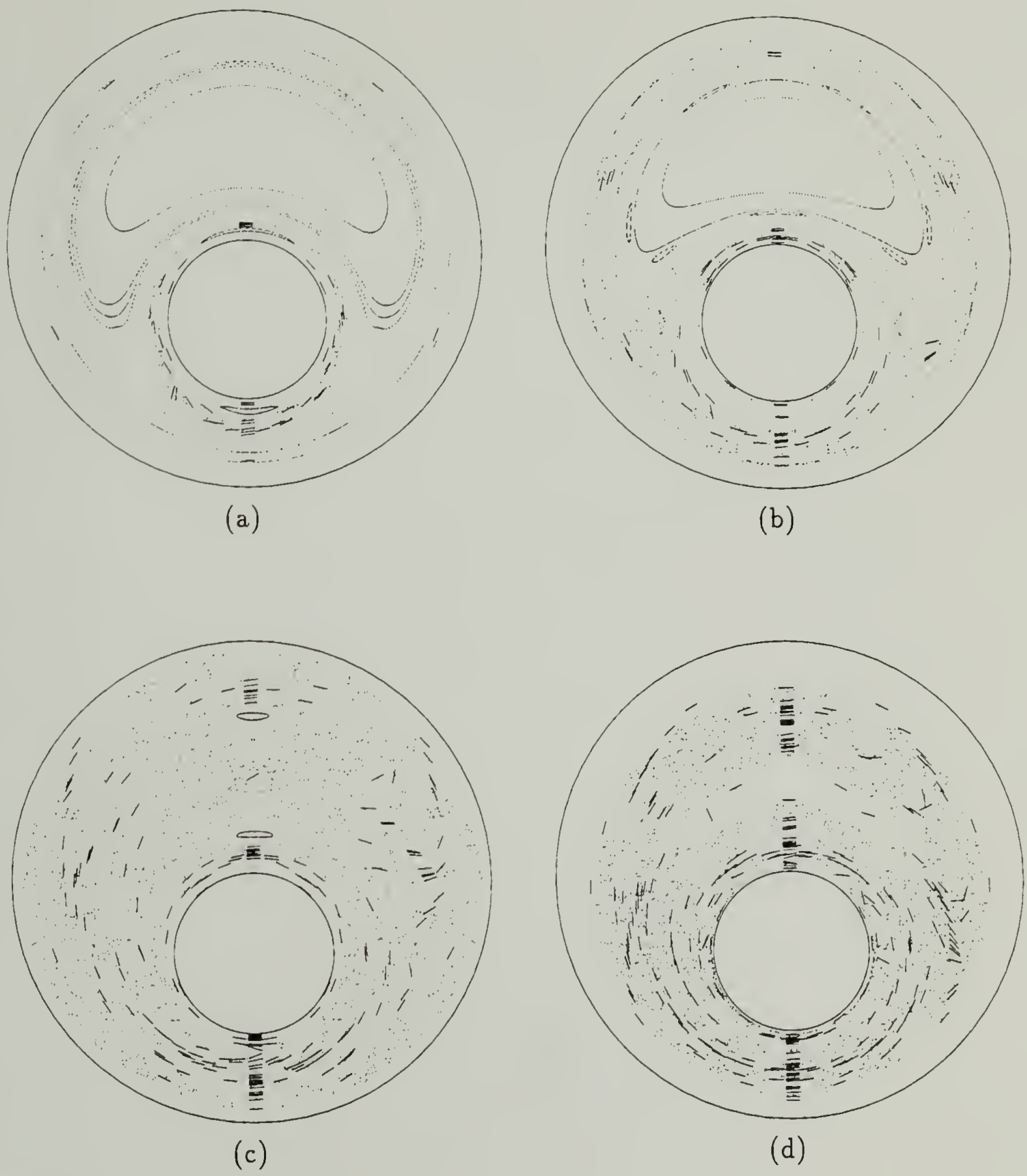

(a) (b) (c) (d)

Figure 4.6: Eigendirections of the hyperbolic periodic points up to period 5 for counter-rotating square wave flow. Flow parameters are $e = 0.3$, $r = 1/3$ and $\Omega = -3.0$ throughout and (a) $\theta = 90°$, (b) $\theta = 180°$, (c) $\theta = 270°$, (d) $\theta = 360°$, (e) $\theta = 450°$, (f) $\theta = 540°$, (g) $\theta = 630°$, (h) $\theta = 720°$.

Continued, next page.

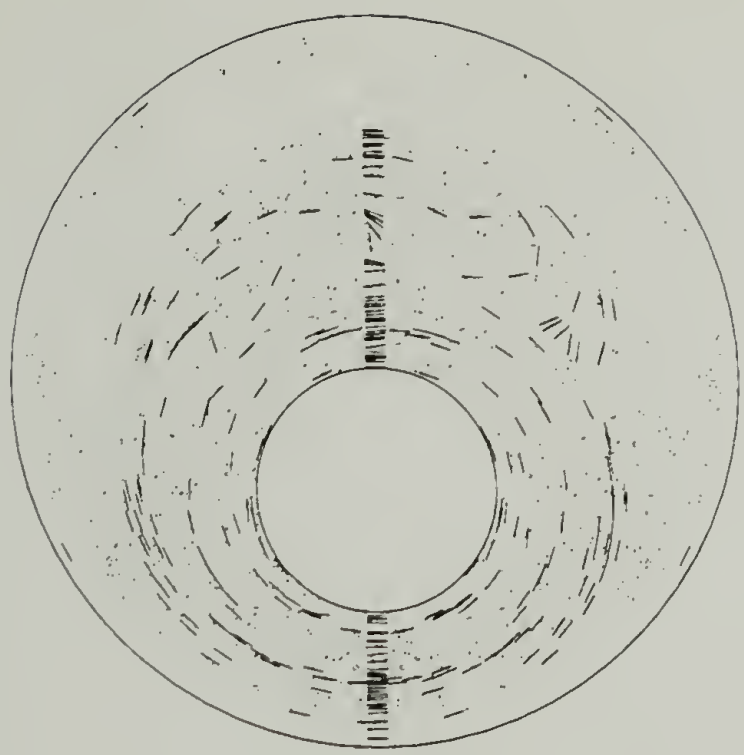

(e)

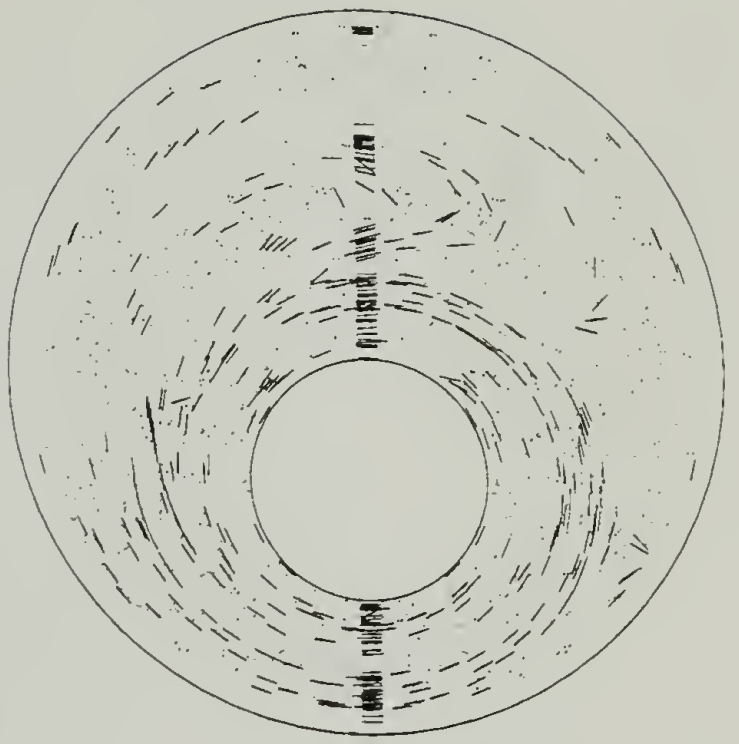

(f)

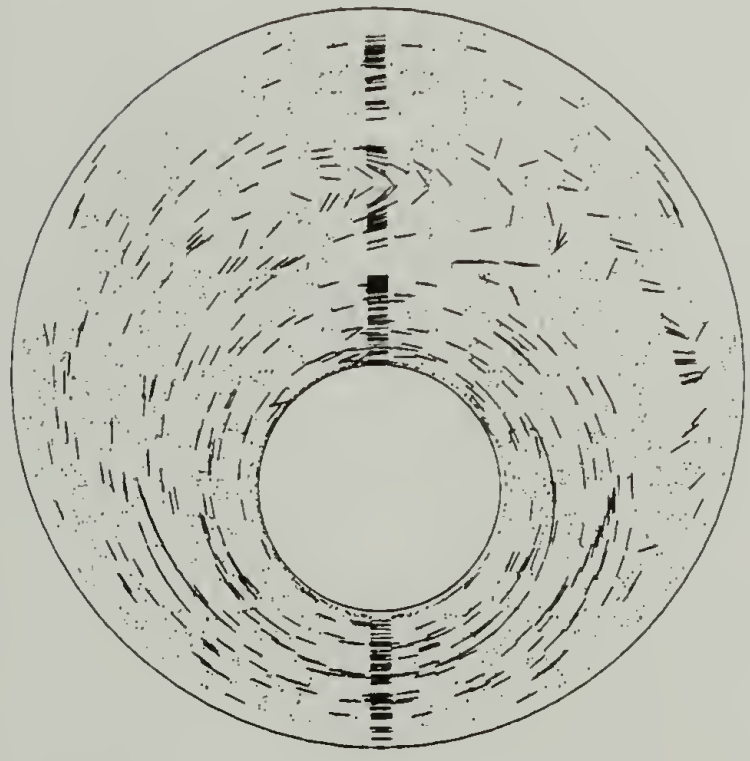

(g)

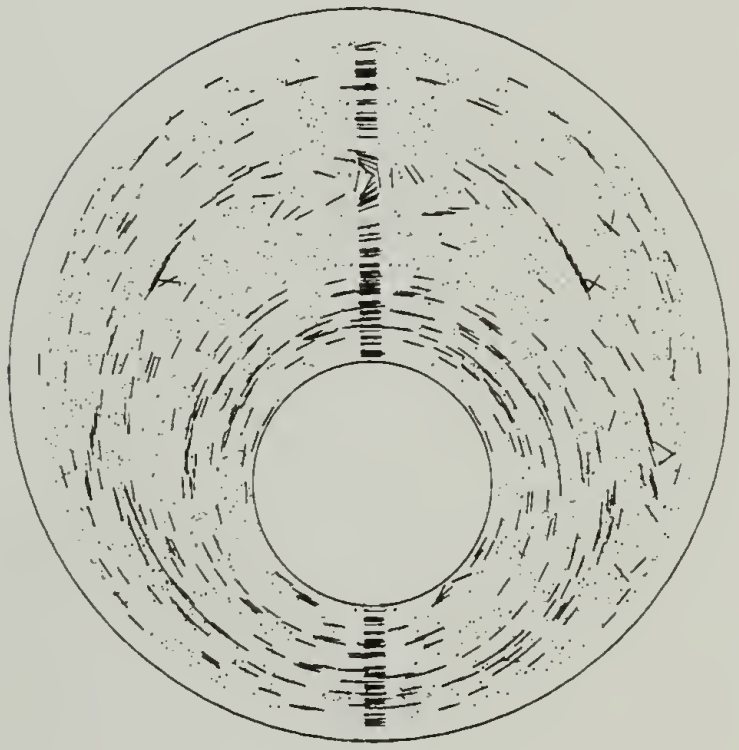

(h)

Figure 4.6: continued.

of the unstable manifold surrounded increases. After a certain number of periods (depending on the eigenvalues of the periodic point and the initial radius of the circle surrounding the periodic point) the circle will appear as a single curve surrounding part of the unstable manifold. Note that manifolds are infinitely long and this method will only show a segment of the unstable manifold.

In order to make this method computational, the circle surrounding the periodic point must be represented as a collection of discrete points. Therefore we do not compute the deformation of circle but rather the deformation of a circle of points. Figure 4.7 shows manifolds of the period-one hyperbolic point corresponding to the saddle point of the steady flow generated using this method. One complication which arises very quickly is that the distance between points becomes so large that the resolution in our representation of the manifold is not acceptable and we can no longer determine where the manifold is. Such a complication is inherent to the method of computation because we are interested in stretching the circle several orders of magnitude larger than its initial radius. Obviously this causes the distance between points to increase by several orders of magnitude as well. There are at least two possible methods of dealing with this problem. The first is to make the initial distance between points very small. This means that we must use a very large number of points in the initial circle. This is not very efficient because the stretching is non-uniform and it is very difficult to determine *a priori* how much each pair of

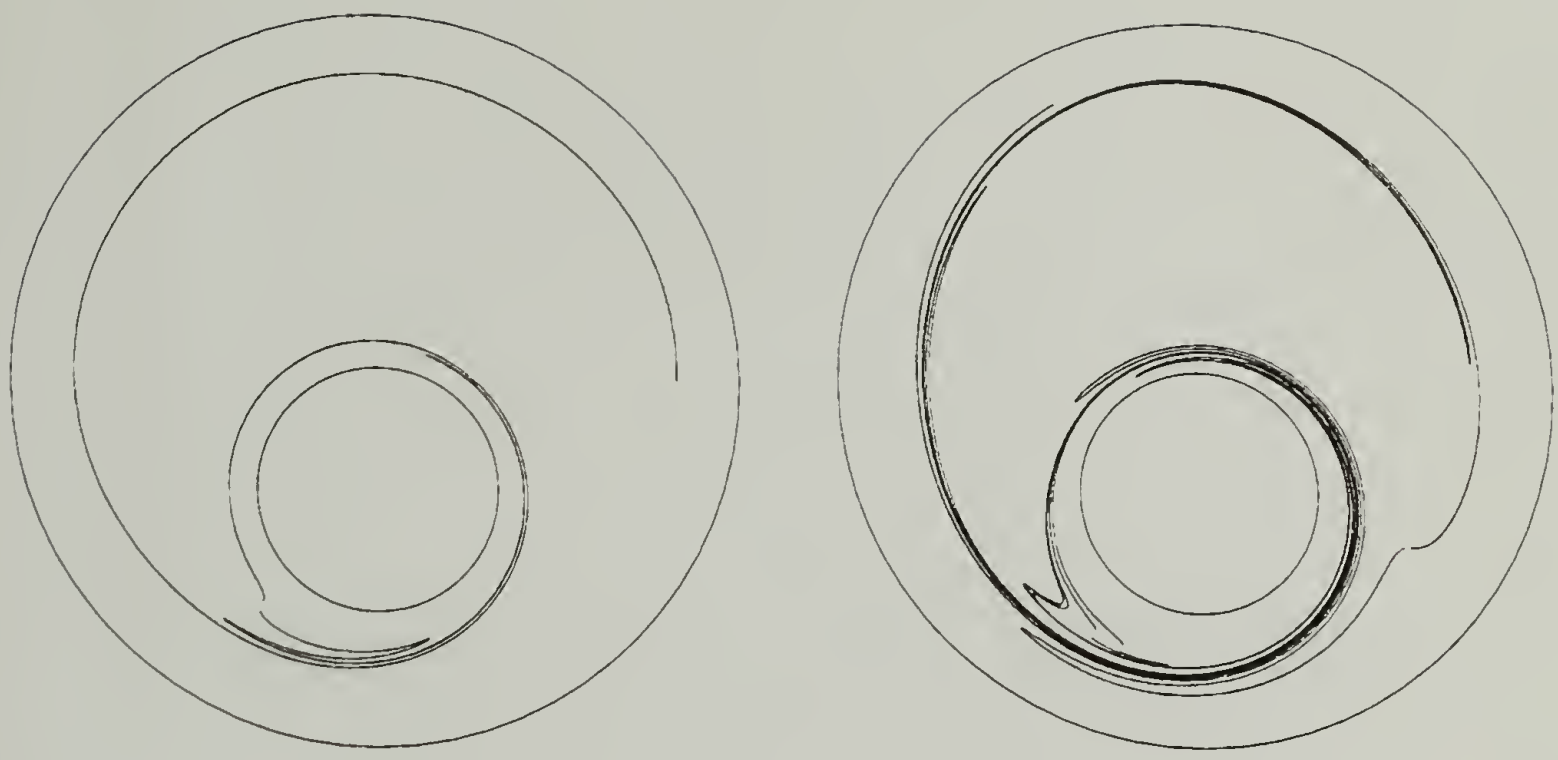

Figure 4.7: Manifolds for counter-rotating square wave flow. Flow parameters are $e = 0.3$, $r = 1/3$ and $\Omega = -3.0$ throughout and (a) $\theta = 90°$, (b) $\theta = 180°$, (c) $\theta = 270°$, (d) $\theta = 360°$, (e) $\theta = 450°$, (f) $\theta = 540°$, (g) $\theta = 630°$, (h) $\theta = 720°$.

Continued, next page.

(e)

(f)

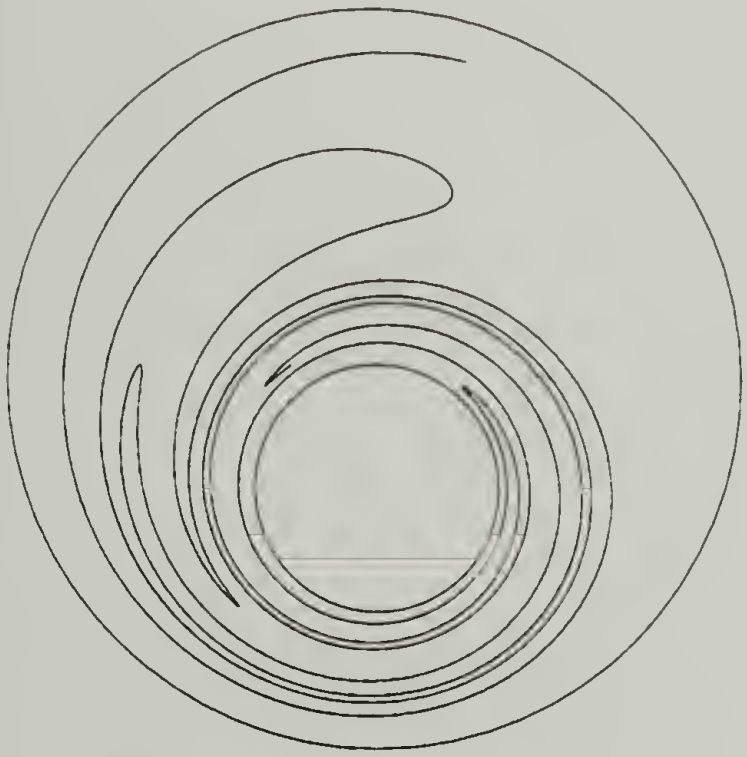

(g)

(h)

Figure 4.7: continued.

points will separate. To insure that no two points spread too far apart we must use an excessive number of points. A much better way to deal with the 'resolution problem' is to add extra points dynamically, as needed. With this method we save time and storage space by avoiding computations with unnecessary points. We have implemented this second method in our manifold algorithm. Even using the second method the number of points necessary to represent the manifold increases geometrically and for the particular example shown in figure 4.7 it was excessively time consuming to run the algorithm for more than three or four periods, depending on the value of θ and the initial radius of the circle. In any event, displaying a larger segment of the manifold than we have shown would tend to obscure rather than clarify the results.

A comparison between figure 3.4 and figure 4.7 demonstrates the very good agreement between the shape of the striations and the shape of the manifolds. The dye has many more folds than the sections of the manifolds shown here but that is because the dye is allowed to evolve for many more periods (the experiments not only evolve for more periods, 10 compared to 3 or 4, but the initial radius of the drop is some orders of magnitude greater than the initial radius of the circle). Pictures of the dye after a short number of periods show patterns which are strikingly similar to the manifold plots. The 'shape' that the dye will adopt becomes apparent after a very few periods; subsequent periods merely 'fill in' the picture. Undoubtedly if

we were to plot a very long length of the manifold it would look nearly identical to the dye deformation experiments.

In addition to computing the locations of the manifolds the behavior of the manifolds can be studied. One analytical method which exists for studying manifolds is the Melnikov method. This method was described in section 2.1. The method is valid only for small perturbations and therefore must be used with extreme care in the analysis of mixing. If the perpendicular distance between the manifolds becomes multivalued the Melnikov method is no longer valid (for example if one of the manifolds has a 'kink' in it). In fact, there is always some neighborhood of a hyperbolic periodic point within which the Melnikov method can no longer accurately approximate its manifolds. However, [27] have shown that useful information about the mixing can be gained if the Melnikov method is valid for as little as one 'lobe' (a lobe is the area enclosed by the segments of the stable and unstable manifolds between neighboring zeros of the Melnikov function) of the intersection of the stable and unstable manifolds. Viewing plots of the unstable and stable manifolds (not shown) we have determined that the Melnikov method may be useful (i.e. there is at least one lobe without 'kinks' in it) for values of θ up to about 180°. Since the region of most interest (i.e. best mixing) occurs well beyond 180°, the Melnikov method is of little direct use to our mixing studies. However, in the next chapter we

describe how the Melnikov method can be used to measure the relative perturbation strengths of different waveforms.

4.4 Stretching

A necessary condition for mixing to occur is that fluid elements must be stretched. In the experiments shown in figure 3.4 the initial drops have been stretched to a length several orders of magnitude greater than their initial radius. A natural question to ask in this context is 'where does most of the stretching occur?' The results presented so far would suggest that the stretching is highly non-uniform throughout the flow domain. To determine the stretching consider an infinitesimal fluid element (a point in the flow domain). The stretching of an infinitesimal vector of arbitrary initial orientation located at the element (at this point) can be computed if one knows the deformation tensor. The deformed infinitesimal vector at some later time t is given by:

$$d\mathbf{x}(t) = \mathbf{F}(t) \cdot d\mathbf{X}, \tag{4.3}$$

where $d\mathbf{X}$ is the initial vector, $d\mathbf{x}(t)$ is the deformed vector, and $\mathbf{F}$ is the deformation tensor. To find $\mathbf{F}$ we solve the following set of differential equations:

$$\dot{\mathbf{F}} = (\nabla \mathbf{v})^T \cdot \mathbf{F}, \; \dot{\mathbf{x}} = \mathbf{v} \tag{4.4}$$

with initial conditions

$$\mathbf{F}_{t=0} = \mathbf{I}, \; \mathbf{x}_{t=0} = \mathbf{X} \tag{4.5}$$

where $\mathbf{x}$ is the location of the fluid element initially located at $\mathbf{X}$, $\mathbf{v}$ is the velocity, and $\mathbf{I}$ is the identity matrix. One detail should be emphasized. The fluid element is convected by the flow so the gradient of the velocity field is time dependent. The equations of motion for the fluid element must simultaneously be solved to compute $(\nabla \mathbf{v})^T$. The length stretch is defined as the ratio of the magnitudes of $d\mathbf{x}$ and $d\mathbf{X}$:

$$\lambda = \|d\mathbf{x}\|/\|d\mathbf{X}\|. \tag{4.6}$$

Ideally we would like to have a closed form solution for $\mathbf{F}$, and hence an expression for λ, as a function of position and time. In practice, we are unable to find such a closed form solution and so we must compute $\mathbf{F}$ numerically. This means that we can only determine λ at discrete points in the flow domain. In order to determine the stretching field we discretize or pixelate the flow and approximate the stretching in a pixel as the stretching of a single point within the pixel. Note that this assumes the stretching is relatively homogeneous within a pixel. Such an assumption is adequate for the type of results shown here. A value of stretching is arbitrarily chosen above which the stretching is considered 'good' and any pixel with stretching larger than this value is colored white. This value is called the 'cutoff value'. Note that although the choice is arbitrary, the results are relatively insensitive to it over a very large range of values (generally at least an order of magnitude). Pixels whose values of stretching are less than the cutoff value are colored black.

There is one further detail which must be resolved. We must choose whether to plot the stretching as a function of initial location or final location, i.e we can plot how much a point initially located in a particular pixel will stretch or how much a point currently located in a particular pixel has stretched. The results shown here show the stretching as a function of final location; however, as a consequence of the symmetry of the system it can be shown that plots according to initial location and final location are symmetric with respect to each other. Note that if we plot the results as a function of final position there is no information on the initial position of the points. Likewise, a plot of the results as a function of initial position would give no information about the final position.

Figure 4.8 shows the results of the stretching computations plotted according to final position. It is significant that there is no information in the plots indicating where the points originated. The plots only show how much each point has stretched after some number of periods and then only up to some cutoff value. There may be points which stretch several orders of magnitude more than the cutoff value but this information is hidden by the plotting method. In light of these provisos let us compare the stretching results to the Poincaré sections. For all cases the white regions (where the amount of stretching is large) lie within the chaotic regions as marked by the Poincaré sections. This is exactly what we expect.

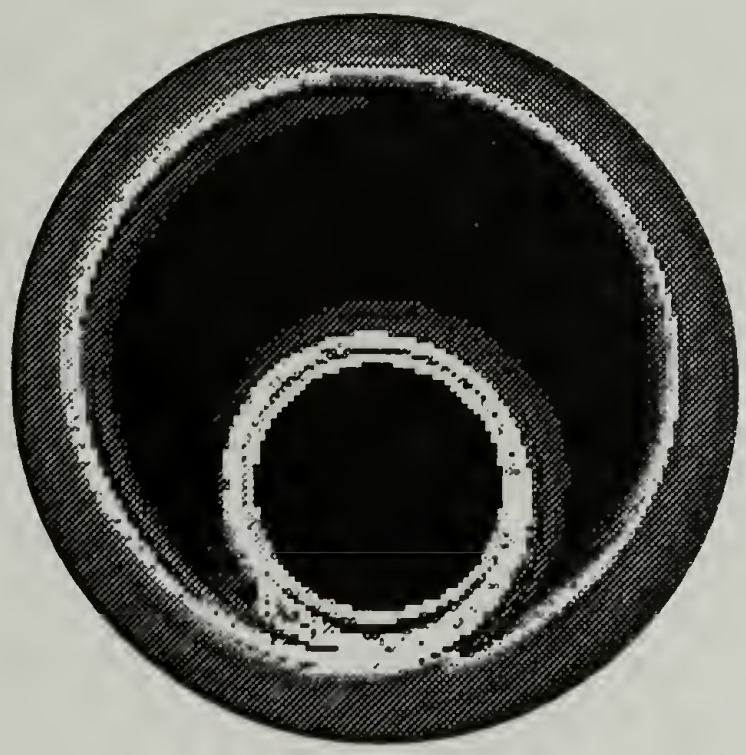

(a)

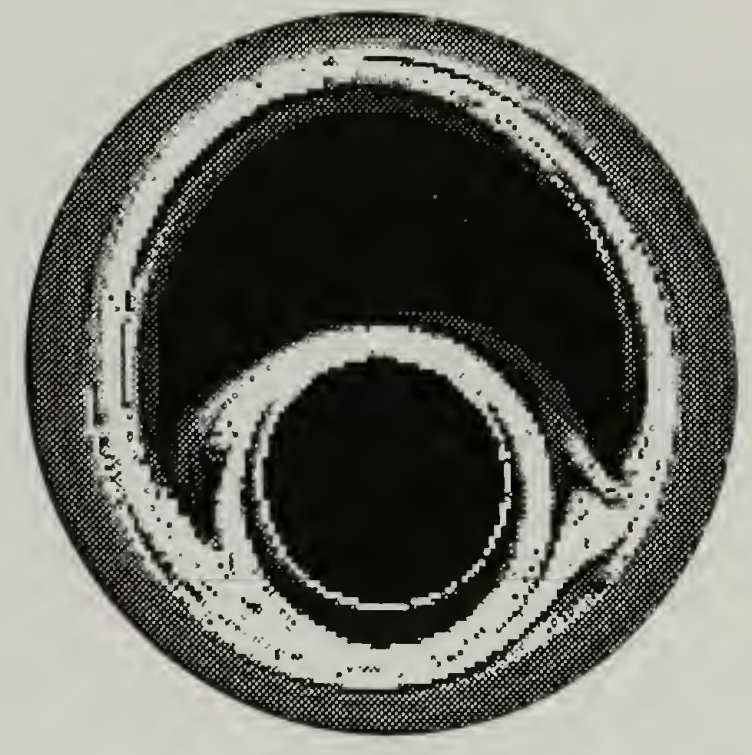

(b)

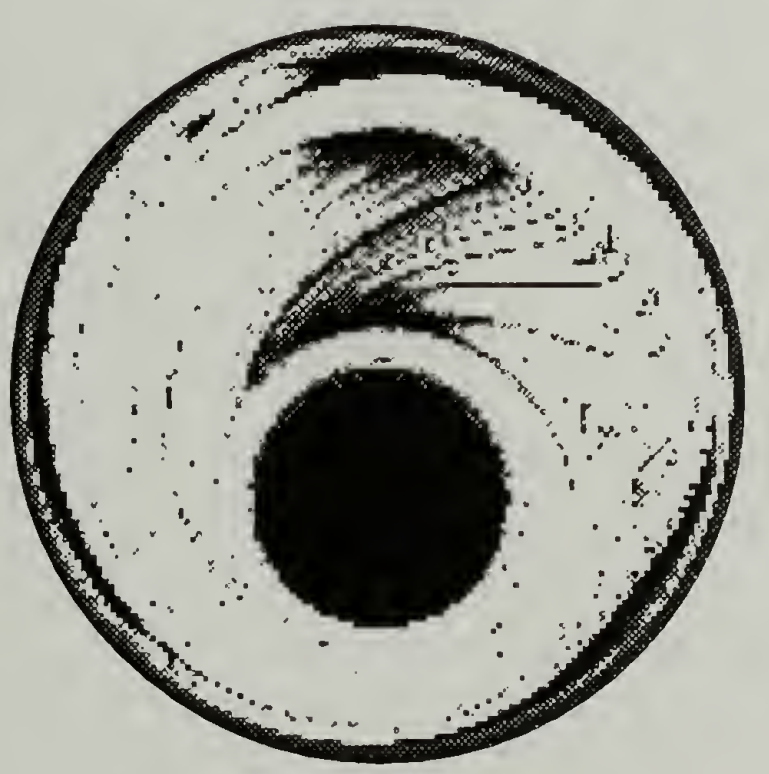

(c)

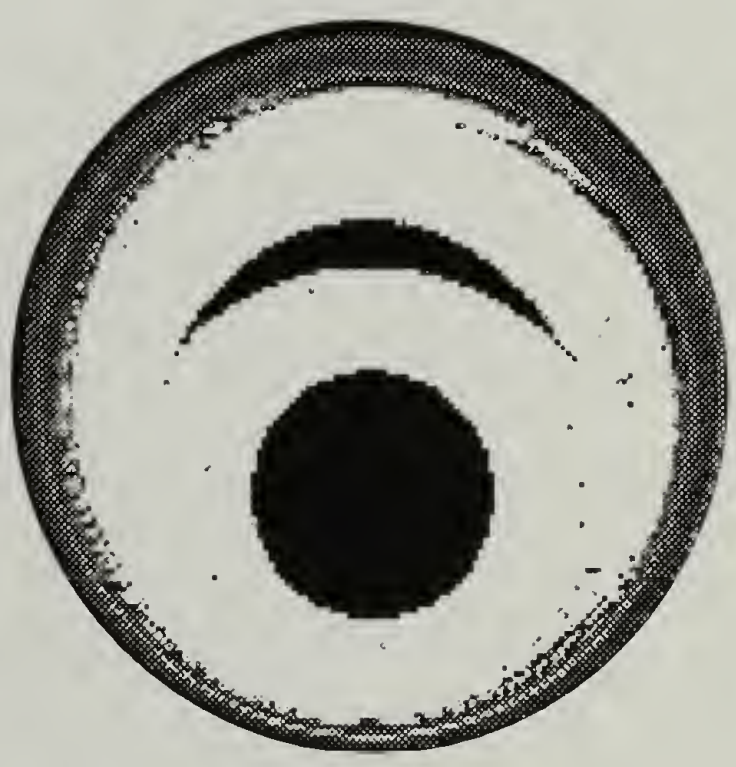

(d)

Figure 4.8: Stretching plots for counter-rotating square wave flow. Flow parameters are $e = 0.3$, $r = 1/3$ and $\Omega = -3.0$ throughout and (a) $\theta = 90°$, (b) $\theta = 180°$, (c) $\theta = 270°$, (d) $\theta = 360°$, (e) $\theta = 450°$, (f) $\theta = 540°$, (g) $\theta = 630°$, (h) $\theta = 720°$.

Continued, next page.

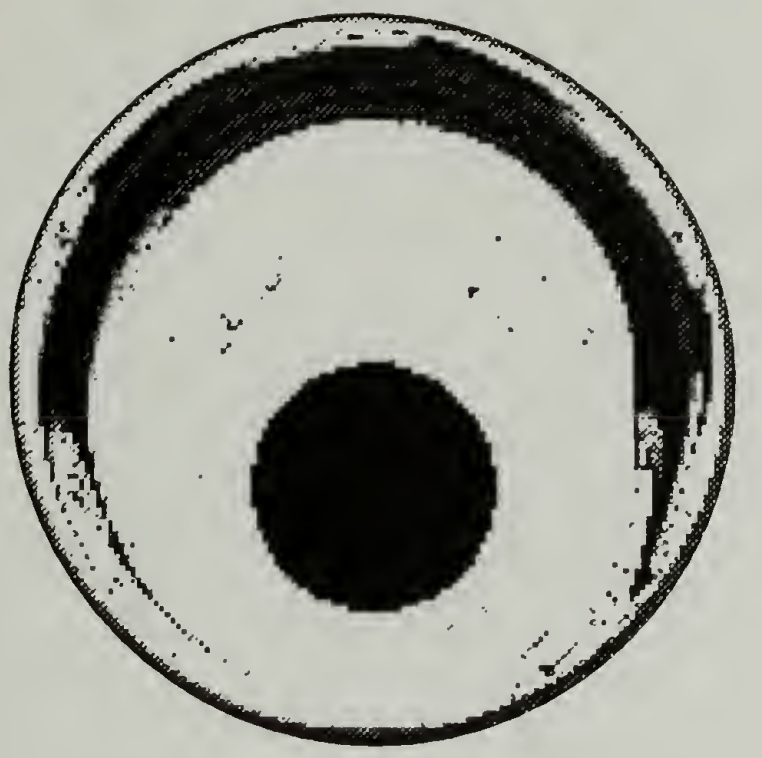

(e)

(f)

(g)

(h)

Figure 4.8: continued.

When the stretching plots are compared with the experiments (figure 3.4) something quite unexpected becomes evident; the regions of high stretch in the stretching plots match, to within their limited resolution, the regions that dye spreads over in the experiments. This correlation is remarkable because the stretching computations and the experiments show completely different types of results. The experiments show the evolution of a continuous set of initial conditions (the initial drop of dye) whereas the stretching computations show the degree of stretching in the flow domain but contain no information about initial location. Further studies have shown that the agreement between experiments and stretching computations is valid even for a very short number of periods, two or so, where the dye covers only a small fraction of the chaotic region. There must be some underlying reason behind this remarkable match of such dissimilar processes. This issue will be explored in greater detail in the next chapter.

CHAPTER 5

MIXING IN THE JOURNAL BEARING

In the previous chapter we focused on information provided by various computational techniques to probe the mixing ability of a flow; the journal bearing served as a model system to help us examine their usefulness. In this chapter we use these techniques to examine three aspects of chaotic behavior in the journal bearing. First we discuss the large difference in the mixing ability of co-rotating and counter-rotating flows, then we explore the apparent similarity in the dynamics produced by different waveforms and finally we examine the limits and underlying reason for the agreement of the stretching plots and dye deformation experiments.

5.1 Co-rotation vs. Counter-Rotation

One of the features of the journal bearing geometry is the variety of flow types which can be created in it. The computations presented so far have all been for the counter-rotating discontinuous velocity protocol. While this limitation was relatively unimportant in the previous chapter, where we were concerned with the connection between experiments and various computational techniques, experiments have demonstrated large differences between co- and counter-rotating modes of operation which merit further exploration.

Figure 5.1 shows Poincaré sections for the co-rotating chaotic flow. It is evident that the chaos is much more widespread for every value of θ than in the corresponding counter-rotating flows (figure 4.1 (a)-(d)). In fact, for $\theta \geq 180°$ the flows appear to be nearly globally chaotic. There is no point in showing Poincaré sections beyond $\theta = 360°$ since there is no apparent structure beyond that point.

The streamline portraits shown in figure 2.6 suggest that the chaotic behavior for the co- and counter-rotating cases might be different. Because the counter-rotating flow has a hyperbolic stationary point and the co-rotational flow has none we might naively expect that the counter-rotating flow would be more chaotic than the co-rotating flow. After all, the manifolds of a hyperbolic point will split apart even with an infinitesimal perturbation and create a chaotic region. There is no such hyperbolic point in the velocity field of the co-rotating flow. However, even though chaos first appears near hyperbolic points in systems that have them, nothing is implied about the chaotic behavior of systems without any hyperbolic points.

One possible explanation of difference in chaotic behavior between the co- and counter-rotational flows is that the elliptic points rather than the hyperbolic points determine the degree of chaotic behavior. This leads to an alternative way to view a globally chaotic flow; that is as a flow where islands are absent rather than a flow where chaos exists throughout the flow domain i.e. we should focus on the existence of islands rather than the presence of chaos. The steady counter-rotating

(a)

(b)

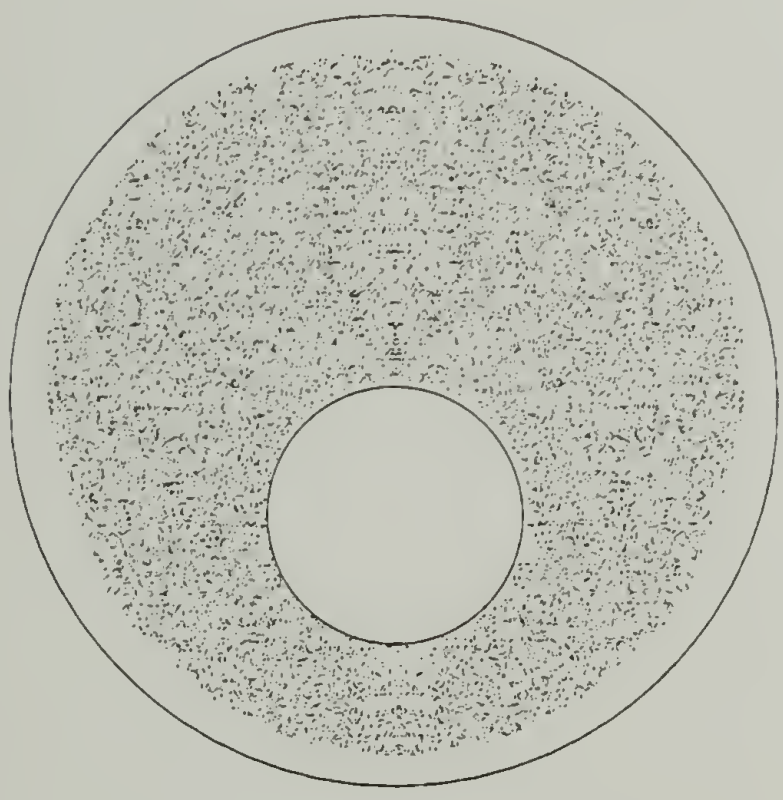

(c)

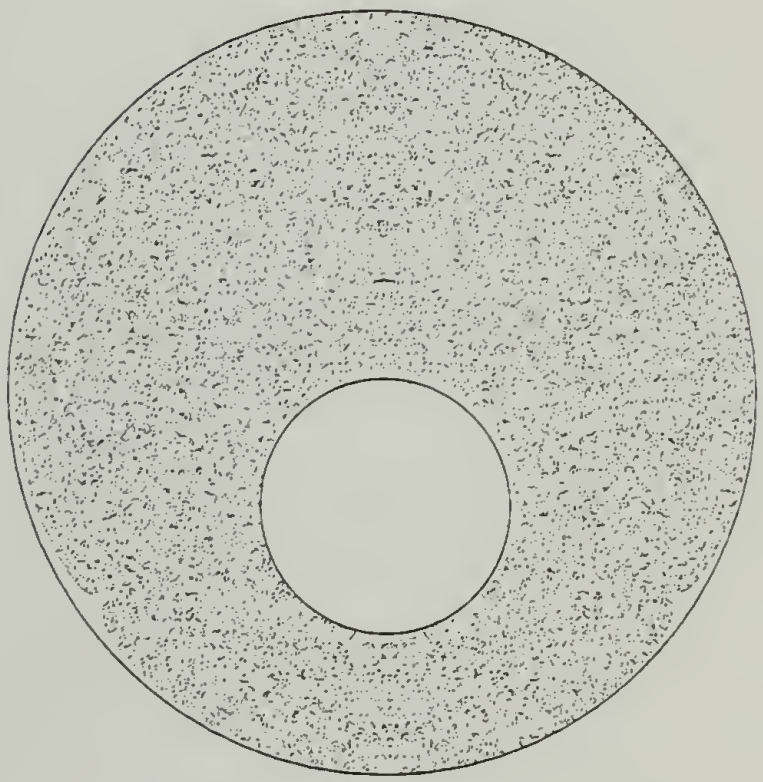

(d)

Figure 5.1: Poincaré sections for co-rotating square wave flow. Flow parameters are $e = 0.3$, $r = 1/3$ and $\Omega = 3.0$ throughout and (a) $\theta = 90°$, (b) $\theta = 180°$, (c) $\theta = 270°$, (d) $\theta = 360°$.

flow has an elliptic stationary point as well as a hyperbolic stationary point. When the flow is perturbed a chaotic region quickly forms near the hyperbolic point and its manifolds but the elliptic point has an island of regular behavior surrounding it. The steady state streamlines for the counter-rotational flow show that there is a large recirculation region surrounding the elliptic point. This recirculation region can be thought of as a 'built in' island and it takes a large perturbation before this island is destroyed. However, the co-rotating case has no such limitation.

Another explanation of the difference between co- and counter-rotation begins with the assumption that only a small region of the flow domain actually mixes the fluid and that this region is the same for the co- and counter-rotating flows. This is probably a reasonable assumption for the discontinuous velocity protocol since at any moment in time the two flows are identical to within a reflection across the symmetry line. Then the extent of the mixing will be determined by how well fluid gets moved into and out of the 'mixing' region. It is clear from the streamline portraits that the co-rotational flow will do a better job of moving fluid around than the counter-rotational flow.

5.2 Similarity of Different Waveforms

In the previous section we made reference to the steady flows corresponding to the co- and counter-rotating chaotic flows in an effort to explain differences in mixing

behavior. In this section we look at the effect of different waveforms on the mixing. Our results suggest that the underlying steady flow is closely related to the chaotic flows. This is rather surprising since the perturbations are of $\mathcal{O}(1)$. We find that the dynamical behavior of the flows created by the three waveforms is quite similar. We then attempt to improve their agreement.

Figure 5.2 shows Poincaré sections for the square wave, sine wave, and sawtooth wave as given in equations 2.20-2.22. For all three waves $\epsilon = 1.0$, $\Omega = -3.0$, and $\theta = 180°$. Quite unexpectedly, the results for the three waveforms are almost indistinguishable. However, this is not always the case. Figure 5.3 shows Poincaré sections for the same parameters as figure 5.2 except for $\theta = 270°$. In this case the results for three waveforms appear to be vastly different. Since we might intuitively expect that larger values of θ will result in a greater difference between the waveforms this is not surprising. However, when $\theta = 360°$, figure 5.4, the plots are again very similar, although not as similar as $\theta = 180°$. Fortunately the relatively larger difference in the Poincaré sections for $\theta = 270°$ has a simple explanation. Varying θ slightly in the 270° region results in large changes in the Poincaré sections and also in the rest of the methods of analysis. So small differences between the waveforms produce large differences in the Poincaré sections in this region. Similar results were observed experimentally, shown in figure 3.6.

(a)

(b)

(c)

Figure 5.2: Poincaré sections for the square, sine, and sawtooth waveforms. The flow parameters are $e = 0.3$, $r = 1/3$, $\theta = 180°$, and $\Omega = -3.0$. (a) square wave , (b) sine wave, (c) sawtooth wave.

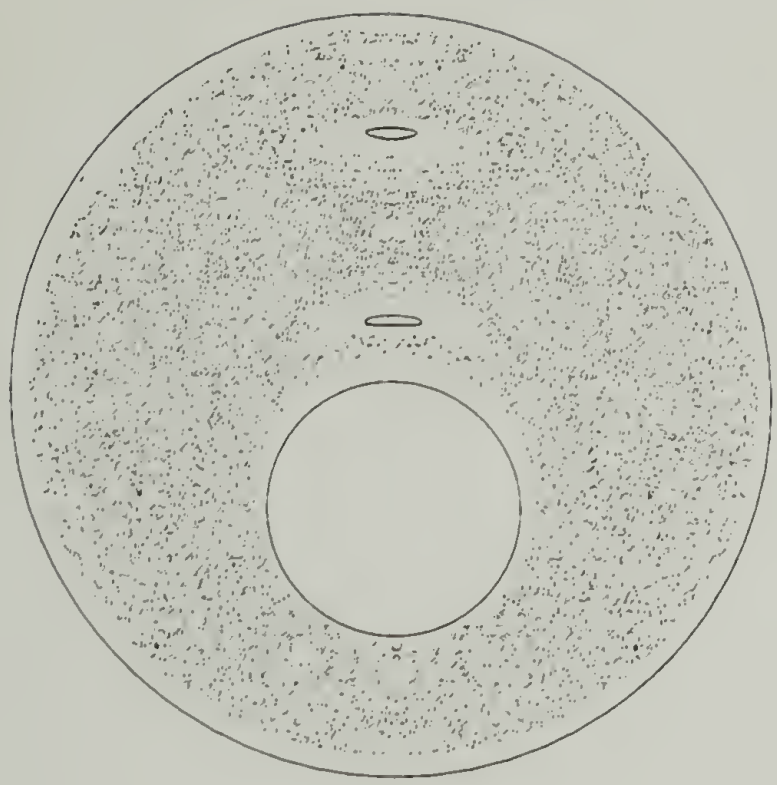

(a)

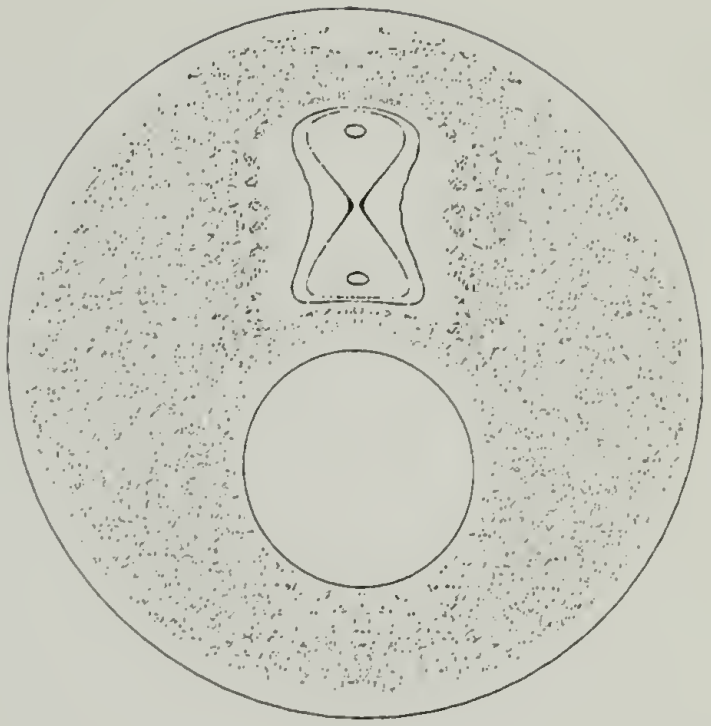

(b)

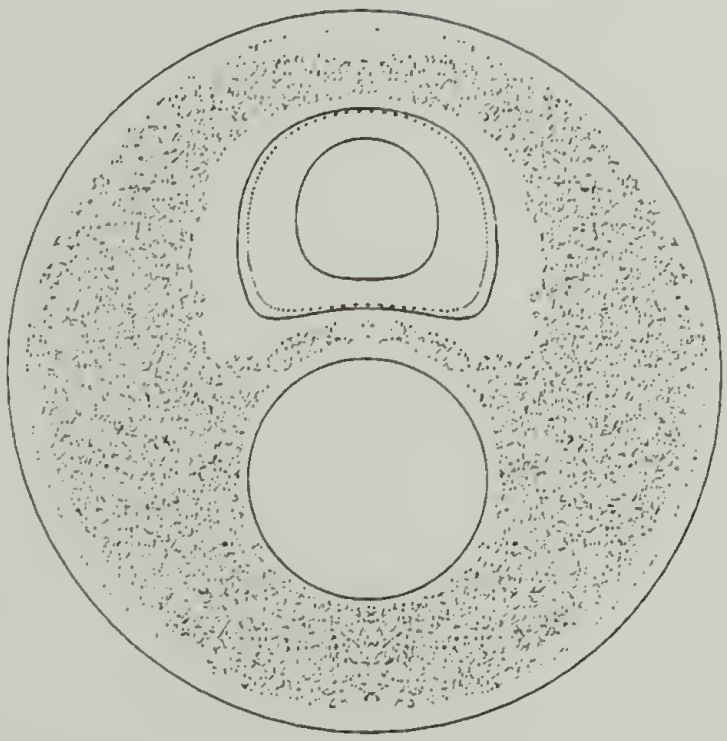

(c)

Figure 5.3: Poincaré sections for the square, sine, and sawtooth waveforms. The flow parameters are $e = 0.3$, $r = 1/3$, $\theta = 270°$, and $\Omega = -3.0$. (a) square wave , (b) sine wave, (c) sawtooth wave.

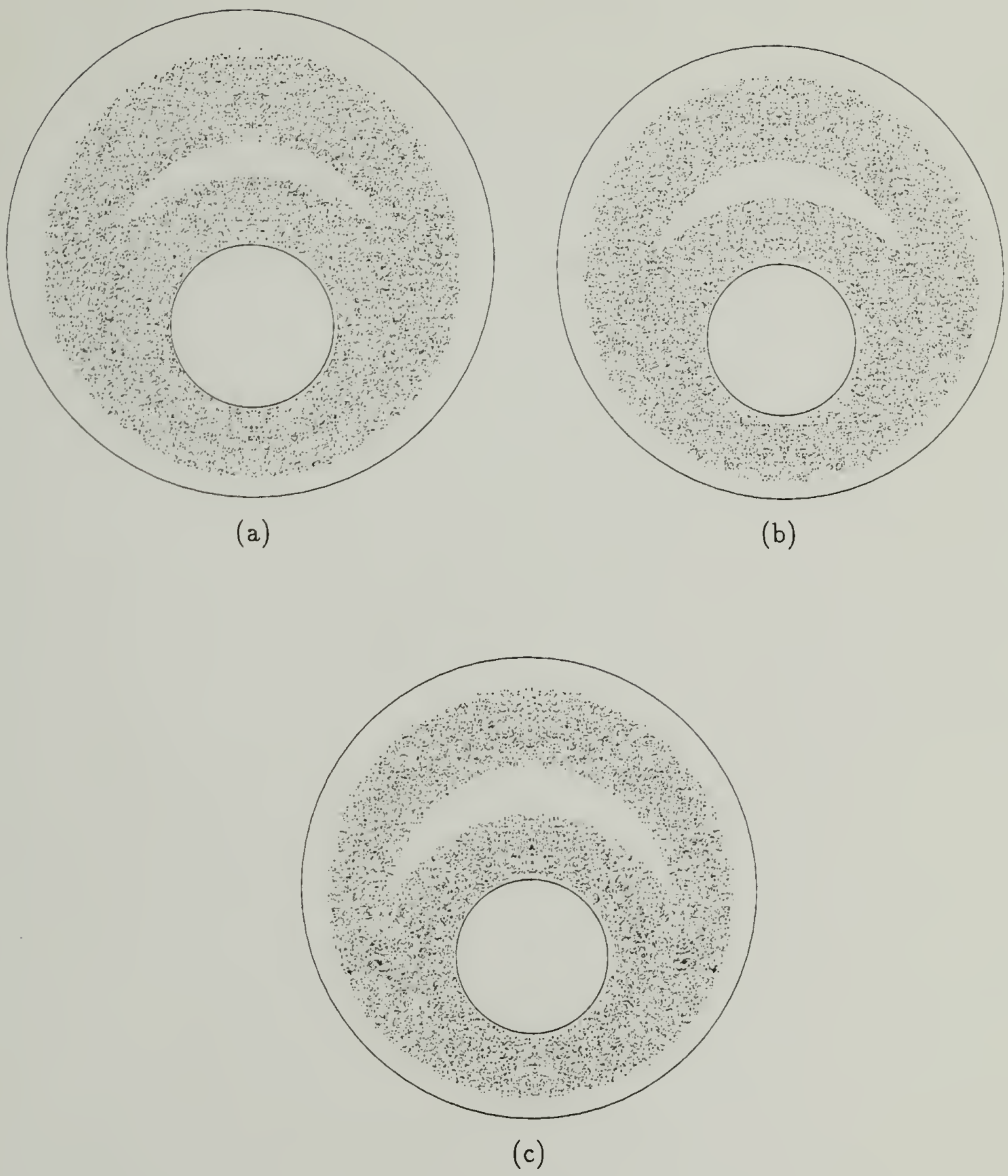

Figure 5.4: Poincaré sections for the square, sine, and sawtooth waveforms. The flow parameters are $e = 0.3$, $r = 1/3$, $\theta = 360°$, and $\Omega = -3.0$. (a) square wave , (b) sine wave, (c) sawtooth wave.

The implication of the similarity of the waveforms is that the system is less perturbed than might be expected with an apparent perturbation strength of 1. This might have been anticipated based on the steady state streamline patterns for the individual cylinders motions (figure 2.6 (a),(b)). Changing the velocities of the cylinders is a relatively weak method of perturbing the system. It is, however, the only physically realizable perturbation we have at our disposal. The streamlines for the inner cylinder motion are aligned quite closely with the streamlines for the outer cylinder motion in most areas of the flow. As a result, only fluid elements in a small region of the flow will follow a very different path depending on weather the inner cylinder or outer cylinder is moving. The real perturbation at any point in the flow could be defined as the imposed perturbation multiplied by the sine of the angle between the streamlines for the individual cylinder motions. Since the streamlines are nearly parallel in many regions of the flow the actual perturbation is substantially less than the imposed perturbation strength. This explanation applies to the discontinuous velocity protocol but velocity protocols where both cylinders are in motion at the same time lead to even smaller actual perturbations.

If the system truly is close to the unperturbed state then we should be able to express the effects of the waveforms as a first order perturbation of the steady flow. If this is true then there will be a parameter which can be adjusted to make the results from the waveforms identical for the entire range of parameters. Specifically,

we should be able to make the Poincaré sections for the three waveforms match for $\theta = 270°$. There are then two questions we wish to address. First, does a parameter exist which can be tuned to make the results from the waveforms match? And second, can we devise some scheme to pick the 'tuning' based on properties of the waveforms and the flow?

Initially it might appear that θ is the parameter to adjust[1]. However, changing θ changes the underlying unperturbed flow; the distance a fluid element travels along its streamline is proportional to θ. For a particular choice of θ some points in the flow will be convected back to their original position after an integer number of periods have elapsed. In dynamical systems terminology these points follow periodic orbits. The significance of these orbits is that they tend to be the first orbits (along with the manifolds of any hyperbolic points) to become chaotic. If θ is changed the location of these orbits is changed and hence the region that the chaotic behavior grows out of is changed. A better choice of perturbation parameter is ϵ of equations 2.20-2.22. In this case the underlying system is preserved when the parameter is changed.

The inherent perturbation due to the three waveforms is different. For the square wave the cylinder velocities are always ϵ away from the average velocities. For the sine wave the average deviation is $(2/\pi)\epsilon$ and for the sawtooth wave it is $(1/2)\epsilon$. The square wave should therefore be more chaotic than the sine wave which, in

[1]Or at least it would have appeared so if equations 2.20-2.22 had been written with $\epsilon = 1$. The only place where $\epsilon \neq 1$ is in this section.

turn, should be more chaotic than the sawtooth wave. We are seeking values of ϵ which will make the waveforms produce nearly identical behavior. We will use the Poincaré sections of figure 5.3 as our indicator of how close the different waveforms are to each other since the system is very sensitive to changes in parameter values in this region.

Three methods are used in an attempt to make the waveforms equivalent. They are the average deviation, the lead term in the Fourier expansion of the waveforms, and the Melnikov method. They are arranged in ascending order of success and difficulty of implementation.

5.2.1 Average Deviation

The first method is based on making the average deviations from the mean velocity the same. Using the sine wave as reference, we set $\epsilon = 2/\pi$ for the square wave, $\epsilon = 1$ for the sine wave, and $\epsilon = 4/\pi$ for the sawtooth wave. Figure 5.5 shows the Poincaré sections obtained for the three waveforms with the prescribed values of ϵ. The sine and sawtooth waves match quite well but the square wave is far different. The Poincaré sections for $\theta = 180°$ and $\theta = 360°$ appear virtually unaffected by this change of ϵ (i.e. we haven't destroyed the correspondence between the waveforms in the cases where they already appeared to match). This method of matching the waveforms appears to be unsuccessful.

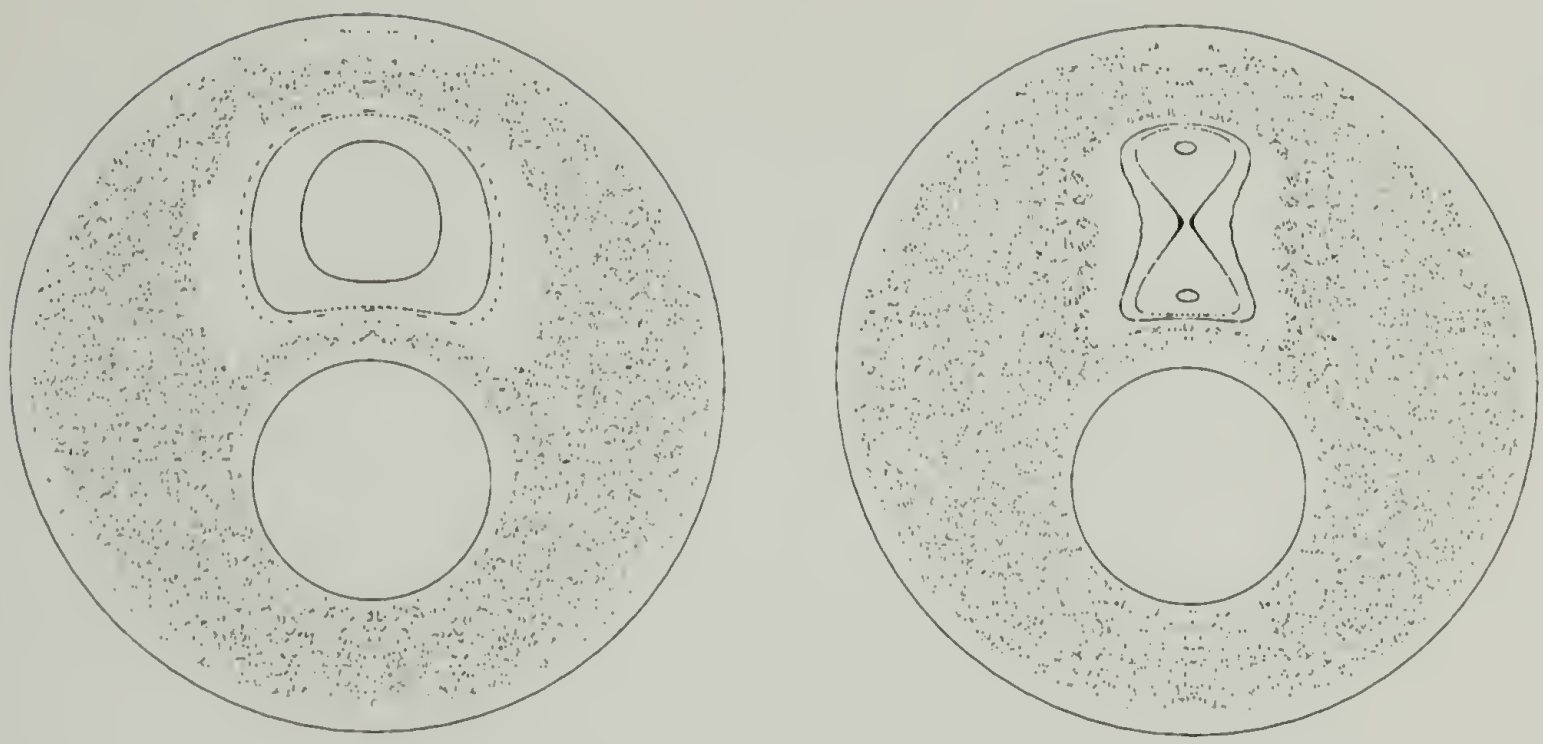

(a)

(b)

(c)

Figure 5.5: Match of Poincaré sections using average deviation to adjust ϵ. The flow parameters are $\theta = 270°$ and $\Omega = -3.0$. (a) square wave with $\epsilon = \frac{2}{\pi} = 0.6366$, (b) sine wave with $\epsilon = 1.0$ (used as reference), (c) sawtooth wave with $\epsilon = \frac{4}{\pi} = 1.2734$.

5.2.2 Fourier Series

The second method is based on replacing the square and sawtooth waveforms with the first term in their Fourier series representations. Before we proceed further some simplification of terminology is in order. The three types of cylinder motion share a common form:

$$\begin{aligned} v_{in} &= \overline{v}_{in}(1 + \epsilon f(t)) \\ v_{out} &= \overline{v}_{out}(1 - \epsilon f(t)) \end{aligned} \tag{5.1}$$

where $f(t)$ depends on the waveform. To match the waveforms we first express the $f(t)$'s in terms of their Fourier series representations. We have:

square wave:

$$f_{sq}(t) = \frac{4}{\pi} \sum_{k=0}^{\infty} \frac{-1^k}{2k+1} \cos \frac{2\pi(2k+1)t}{T} \tag{5.2}$$

sine wave:

$$f_{sin}(t) = \cos \frac{2\pi t}{T} \tag{5.3}$$

sawtooth wave:

$$f_{saw}(t) = \frac{8}{\pi^2} \sum_{k=0}^{\infty} (2k+1)^{-2} \cos \frac{2\pi(2k+1)t}{T} \tag{5.4}$$

We then truncate the Fourier series after the first term. We thus have

$$v = \overline{v}(1 + C\epsilon \cos \frac{2\pi t}{T}) \tag{5.5}$$

for all waveforms where C depends on the waveform. Given the values of C we then choose ϵ's such that $C\epsilon$ is a constant. If once again we set $\epsilon = 1$ for the sine wave, then $\epsilon = \frac{\pi}{4}$ for the square wave and $\epsilon = \frac{\pi^2}{8}$ for the sawtooth wave. Figure 5.6 shows the Poincaré sections for the specified values of ϵ. The agreement between the three waveforms is extremely good; trial and error manipulation of the ϵ's could not yield better results. We have now shown that ϵ can be tuned to make the agreement between the waveforms quite good and we have apparently found a systematic method to properly tune ϵ. To make sure this is correct, we next look at another choice of operating conditions. Figure 5.7 shows the three Poincaré sections for the co-rotational flow with $\theta = 360°$. The perturbation of the sawtooth wave is chosen to be the reference. Clearly the Poincaré sections do not match. Apparently truncating the Fourier series representation of the waveforms does not always provide the proper value for tuning ϵ.

5.2.3 Melnikov Method

One idea for matching the waveforms begins by finding some method for measuring the relative magnitude of the chaos that the waveforms generate. Then the ϵ's can be tuned so that each flow has the same 'amount' of chaos. The separation between the stable and unstable manifolds of a hyperbolic periodic point can be

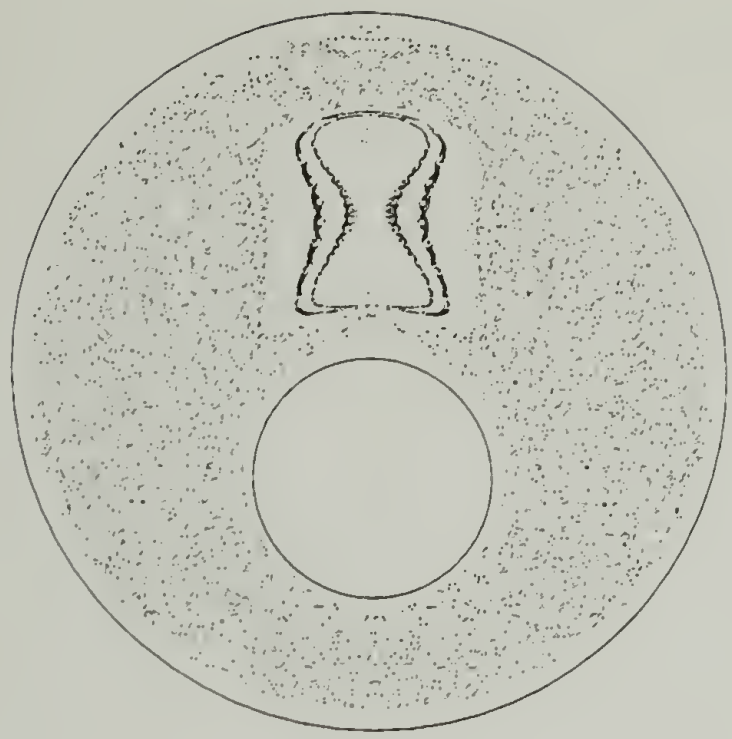

(a)

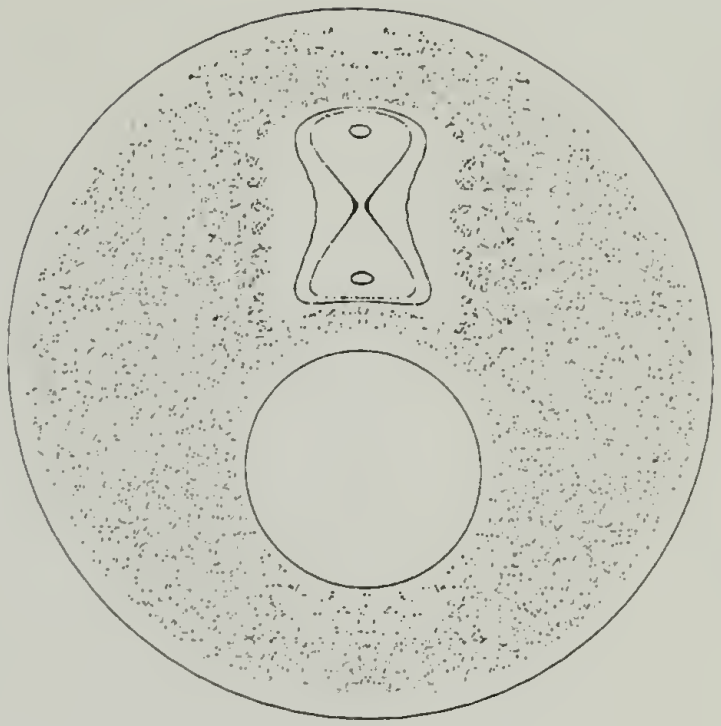

(b)

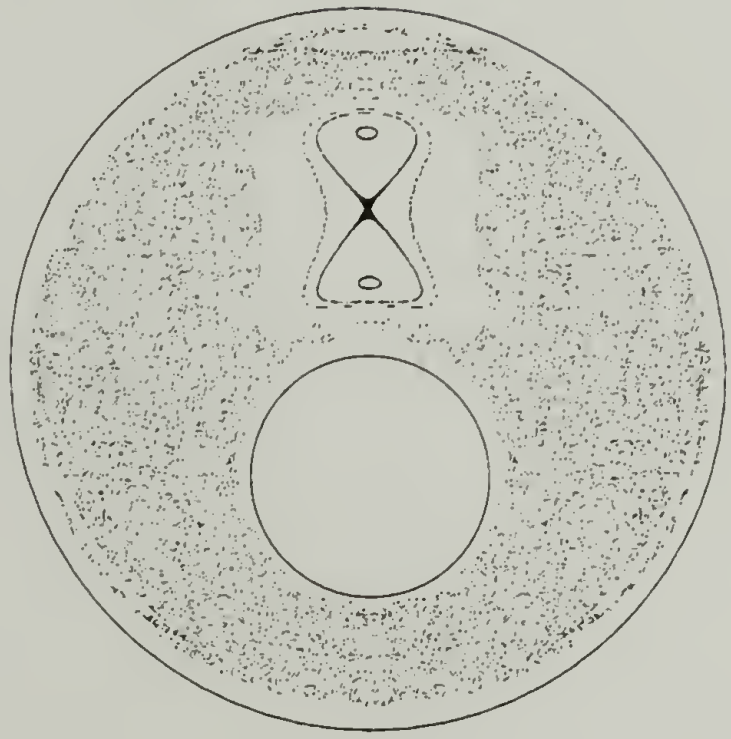

(c)

Figure 5.6: Match of Poincaré sections using the lead term in the Fourier series to adjust ϵ. The flow parameters are $\theta = 270°$ and $\Omega = -3.0$. (a) square wave with $\epsilon = \frac{\pi}{4} = 0.785$, (b) sine wave with $\epsilon = 1.0$ (used as reference), (c) sawtooth wave with $\epsilon = \frac{\pi^2}{8} = 1.2337$.

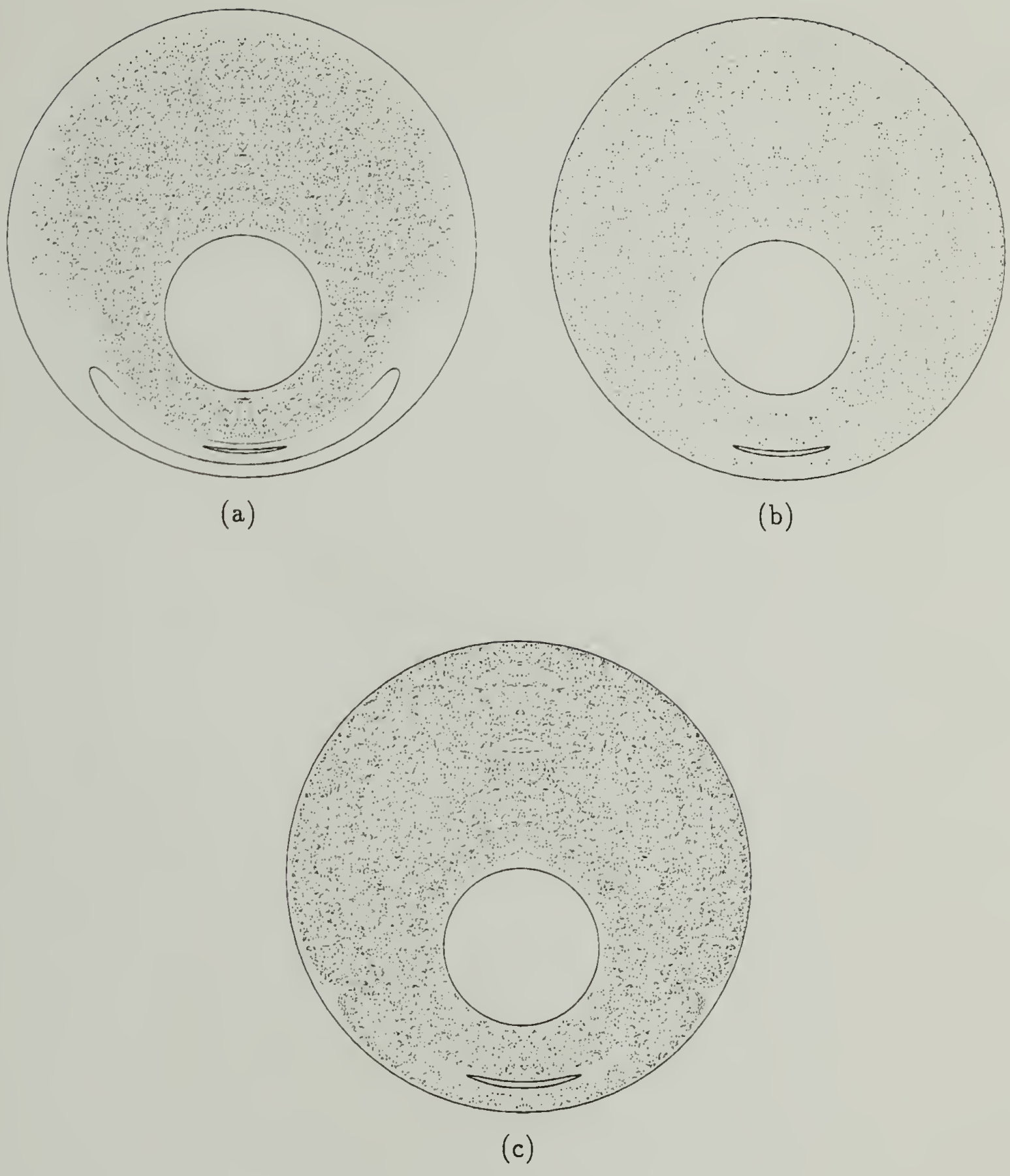

(a) (b) (c)

Figure 5.7: Match of Poincaré sections using the lead term of the Fourier series to adjust ϵ. The flow parameters are $e = 0.3$, $r = 1/3$, $\theta = 360°$, and $\Omega = 3.0$. (a) square wave with $\epsilon = \frac{2}{\pi} = 0.6366$, (b) sine wave with $\epsilon = \frac{8}{\pi^2} = 0.8106$, (c) sawtooth wave with $\epsilon = 1.0$ (used as reference).

used to quantify the relative magnitude of chaos in the system. This has the advantage of being based on some actual property of the dynamical system rather than abstractly on some properties only of the waveforms. Also, we have a method for determining this distance based only on the waveforms and the steady state flow, the Melnikov method.

In order to apply the Melnikov method we split the stream function into a perturbed and unperturbed part. Using equation 5.1 and equation 2.11 we have

$$\Psi(x,y,t) = \Psi_{in}(x,y)\overline{v}_{in}(1+\epsilon f(t)) + \Psi_{out}(x,y)\overline{v}_{out}(1-\epsilon f(t)). \tag{5.6}$$

Rearrangement yields

$$\begin{aligned}\Psi(x,y,t) &= \Psi_{in}(x,y)\overline{v}_{in} + \Psi_{out}(x,y)\overline{v}_{out} \\ &\quad +\epsilon[\Psi_{in}(x,y)\overline{v}_{in}f(t) - \Psi_{out}(x,y)\overline{v}_{out}f(t)].\end{aligned} \tag{5.7}$$

The Melnikov function given in equation 2.9 is

$$M(t_0) = \int_{-\infty}^{\infty}\{H(x,y), G(x,y,t+t_0)\}dt \tag{5.8}$$

where in our case

$$H(x,y) = \Psi_{in}(x,y)\overline{v}_{in} + \Psi_{out}(x,y)\overline{v}_{out} \tag{5.9}$$

and

$$G(x,y,t) = \overline{v}_{in}f(t)\Psi_{in}(x,y) - \overline{v}_{out}f(t)\Psi_{out}(x,y). \tag{5.10}$$

Evaluating the Poisson bracket (see equation 2.10) using equations 5.9 and 5.10 for H and G we find

$$\{H, G\} = -2\overline{v}_{in}\overline{v}_{out} f(t)[\frac{\partial \Psi_{in}(x,y)}{\partial x}\frac{\partial \Psi_{out}(x,y)}{\partial y} - \frac{\partial \Psi_{in}(x,y)}{\partial y}\frac{\partial \Psi_{out}(x,y)}{\partial x}]. \quad (5.11)$$

Substitution into 5.8 yields:

$$M(t_0) = \int_{-\infty}^{\infty} -2\overline{v}_{in}\overline{v}_{out} f(t+t_0)[\frac{\partial \Psi_{in}(x,y)}{\partial x}\frac{\partial \Psi_{out}(x,y)}{\partial y} - \frac{\partial \Psi_{in}(x,y)}{\partial y}\frac{\partial \Psi_{out}(x,y)}{\partial x}]dt. \quad (5.12)$$

The Melnikov method requires that $f(t)$, the time dependent part of the waveforms, be continuous and have continuous first derivatives. Therefore we use the Fourier representations of $f(t)$ given in equations 5.2-5.4 to calculate the Melnikov functions. The Melnikov function has the general form

$$M(t_0) = \sum_{i=1}^{\infty} C_i M_i \sin\frac{2\pi i t_0}{T} \quad (5.13)$$

where the C_i are the coefficients of the Fourier series for the different waveforms. The M_i are given by:

$$M_i = \int_{-\infty}^{\infty} -2\overline{v}_{in}\overline{v}_{out} \sin(\frac{2\pi i t}{T})[\frac{\partial \Psi_{in}(x,y)}{\partial x}\frac{\partial \Psi_{out}(x,y)}{\partial y} - \frac{\partial \Psi_{in}(x,y)}{\partial y}\frac{\partial \Psi_{out}(x,y)}{\partial x}]dt \quad (5.14)$$

where the position (x, y) is located along the unperturbed manifold and is parameterized by t. In order to determine the perturbation strength of the flow we evaluate equation 5.13 setting the sin terms equal to 1.

For the counter-rotating flow the evaluation of the M_i's in equation 5.14 is straight forward. We choose one of the manifolds (it does not matter which one) of the hyperbolic point in the steady flow and numerically compute the M_i's. When the M_i's are computed we find M_1 to be several orders of magnitude greater than the rest of the M_i's. This means that the adjustments to the ϵ's calculated from the Melnikov method are identical to those calculated from the lead terms in the Fourier series.

In the case of the co-rotating flow there is no hyperbolic point or manifold to evaluate the Melnikov function along. Instead we can use the subharmonic Melnikov function [13] to generate our measure of the chaos in the system. In this case the equations for our M_i's become

$$M_i = \int_0^T -2\overline{v}_{in}\overline{v}_{out}\sin(\frac{2\pi it}{T})[\frac{\partial\Psi_{in}(x,y)}{\partial x}\frac{\partial\Psi_{out}(x,y)}{\partial y} - \frac{\partial\Psi_{in}(x,y)}{\partial y}\frac{\partial\Psi_{out}(x,y)}{\partial x}]dt \tag{5.15}$$

where (x, y) are now evaluated along a period one periodic orbit in the steady flow (note that this is the reason for the new limits of the integral). When we evaluate these integrals for the co-rotating flow we find that the first few M_i's are similar in magnitude as opposed to the counter-rotating case where M_1 dominated. We find for the co-rotating flow that the adjusted perturbations should be $\epsilon = 0.745$ for the square wave and $\epsilon = 0.85$ for the sine wave based on $\epsilon = 1.0$ for the sawtooth wave.

Figure 5.8 shows the Poincaré sections for the three waveforms with the values

(a)

(b)

(c)

Figure 5.8: Match of Poincaré sections using the Melnikov method to adjust ϵ. The flow parameters are $e = 0.3$, $r = 1/3$, $\theta = 360°$, and $\Omega = 3.0$. (a) square wave with $\epsilon = 0.745$, (b) sine wave with $\epsilon = 0.85$, (c) sawtooth wave with $\epsilon = 1.0$ (used as reference).

of the perturbations prescribed above. The results are in good agreement. It appears that the Melnikov method has provided a procedure to determine the relative perturbations needed to match the results of the waveforms as well as possible. The agreement is somewhat surprising given the fact that the perturbations are not small However, it is also clear from figure 5.8 that there are some differences between the waveforms. Apparently the systems are perturbed enough so that a simple first order correction cannot make them identical.

5.3 Agreement Between Stretching Plots and Experiments

One of the most surprising results of chapter 4 was the agreement between the stretching plots and the experiments. As has already been stated this is highly surprising given their vastly different nature. It is inconceivable that this is completely fortuitous; there must be some single underlying reason which produces both structures. In this regard there are two questions which merit some exploration. First, the stretching plots shown in figure 4.8 are quite coarse. It may be that the stretching plots will only indicate the grossest features of the striation patterns in the experiments. So the first question to what level of detail do the stretching plots and experiments agree? The second question is simply: What is causing this agreement? However, before these questions are addressed we will look more closely at the evolution of $\mathbf{F}$, the stretching tensor. Our findings here will help to simplify the

computations in the more detailed stretching plots and also add to the explanation of the agreement between the stretching plots and experiments.

5.3.1 Evolution of the Orientation of $d\mathbf{X}$

In 4.4 we computed the stretching by calculating $\mathbf{F}$, the deformation tensor and then using it to determine the amount of stretching experienced by a number of infinitesimal vectors with different initial orientations. The stretching for a particular point was taken to be the average of the stretching of the different initial vectors located at that point. However, rather quickly the stretching becomes quite large and since $\mathbf{F}$ must preserve area one of the eigenvalues of $\mathbf{F}$ also becomes quite large while the other one becomes equally small (since they are inverses of each other). This implies that an initial vector of any initial orientation should, after sufficient time, adopt the orientation of the eigenvector corresponding to the largest eigenvalue. It also implies that the stretching measured is directly proportional to the largest eigenvalue of $\mathbf{F}$.

To determine how quickly an infinitesimal material vector will orient itself with the eigenvector of the largest eigenvalue of $\mathbf{F}$ we perform a very simple computation: We follow the evolution of two, initially perpendicular infinitesimal vectors. Note that these vectors are linearly independent and therefore any other vector can be expressed as a linear combination of these two. If these two vectors become nearly

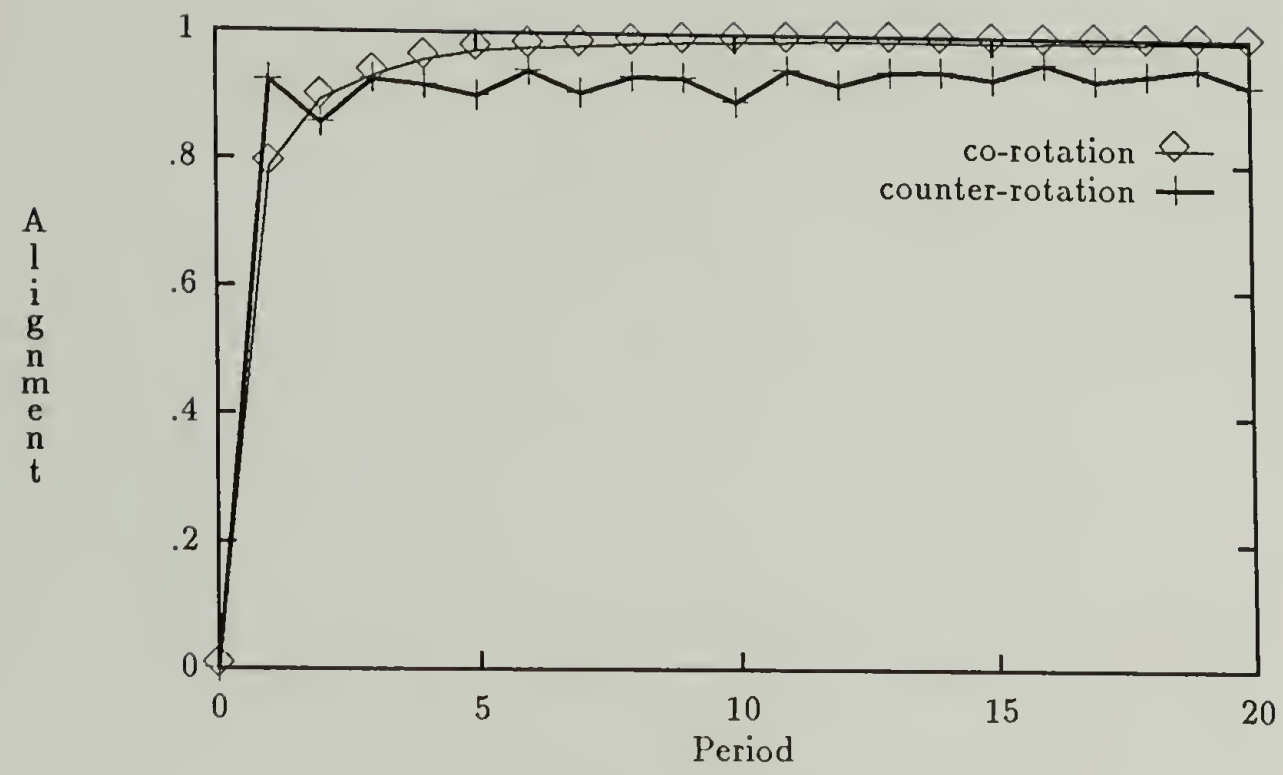

Figure 5.9: Alignment of infinitesimal material vectors for co- and counter-rotating flows at $\theta = 180°$.

coincident then virtually every initial orientation will be coincident with them. In order to determine the degree of alignment between the two initially orthogonal vectors we define a measure

$$M = \frac{a \cdot b}{\|a\|\|b\|} \tag{5.16}$$

which is nothing more than the expression for the cosine of the angle between the two vectors. As this quantity approaches 1.0 the vectors become coincident. In order to compute the average alignment in a flow we average M over 2674 (this number is the result of laying a 64×64 grid over the flow domain and throwing away the points that lie outside the flow domain) initial positions throughout the flow domain. Figure 5.9 shows a plot of average M vs. period for the co- and counter-rotating flows of $\theta = 180°$. M is the average alignment of 2674 initial positions. The plot

shows that the alignment in the co-rotating flow increases monotonically to 1 in a very few number of periods. The alignment in the counter-rotating flow shows an even more rapid initial increase than for the co-rotating flow. However, it appears to asymptote at a level below 1. Recall that there are large regular regions in the $\theta = 180°$ counter-rotating flow. We would expect that infinitesimal material vectors would align much more slowly in regular regions and so the behavior in the counter-rotating flow is not surprising.

5.3.2 Detailed Stretching Plots

In order to determine the degree of agreement between stretching plots and the striation patterns in the experiments we conducted computations according to the following prescription. First, a 0.2 by 0.2 (based on an outer cylinder radius of 1.0) square subregion of the flow was picked out which contained 'interesting' striation patterns in the experimental results. The region picked out depends on the choice of operating conditions but it is always along the symmetry line. This allows us to switch between stretching plots based on initial location and stretching plots based final location simply by reflecting across the symmetry line[2]. The region is then subdivided into a 900×900 grid and an initial infinitesimal vector is placed at each grid point. From the previous section we know that the initial orientation

[2]We can actually do this for any region but the initial and final regions will be different in general.

is relatively unimportant when determining the stretching so instead of calculating **F** we just follow one infinitesimal vector. This cuts the computation time roughly in half but has the slight disadvantage of introducing some minor artifacts into the stretching plot. Since the computations take 1-2 hours on a CRAY-2 halving the computation time is highly advantageous.

Once the stretching values are computed all 810000 (900×900) values are put into a list and sorted according to size. The list is then split up into 256 parts and a shade of gray is assigned to each range of stretching values. The grid locations containing the largest stretching values are shaded white and the locations corresponding to the smallest stretching values are shaded black. Grid locations with intermediate stretching values are shaded with the appropriate level of gray. Since the region where the stretching plot is being computed is symmetric about the line of symmetry we can plot stretching either as a function of final position or initial position by simply reflecting the plot across the line of symmetry. If we plot the stretching as a function of final position we can determine where most of the stretching ends up but the plot gives no indication of where the points originated. On the other hand if we plot the stretching as a function of initial position we can determine where the points with a given amount of stretching originated but there is no information about where the points end up.

As an example consider the counter-rotating square wave flow with $\theta = 270°$. Within this flow we focus on the region between the two vertically aligned islands. Figure 5.10 shows the full stretching plot at these parameter values (this is the same as figure 4.8(c)) where the box marks the region in which we will make a detailed stretching plot. The equivalent dye deformation experiment is shown in figure 3.4(c). Figure 5.11 shows the detailed stretching plot and the corresponding enlarged region of the experiment. There is excellent agreement among the striation patterns in both pictures. The agreement between the pictures suggests that there must be some underlying phenomenon which creates the patterns in both results.

5.3.3 Agreement Between High Stretching Regions and Stable Manifolds

One possible explanation for the agreement between the stretching plots and experiments is that the manifolds are responsible for both structures. We have already seen the good agreement between the manifolds and the overall structure in the experiments. Now we wish to look at the connection between the manifolds and the stretching plots. In order to do this we concentrate only on the highest stretching regions of the stretching plot. We generate a new stretching plot in exactly the same manner as in the previous section but instead of assigning shades of gray to each pixel we mark the pixels with the highest 6.25% of stretching values with black and

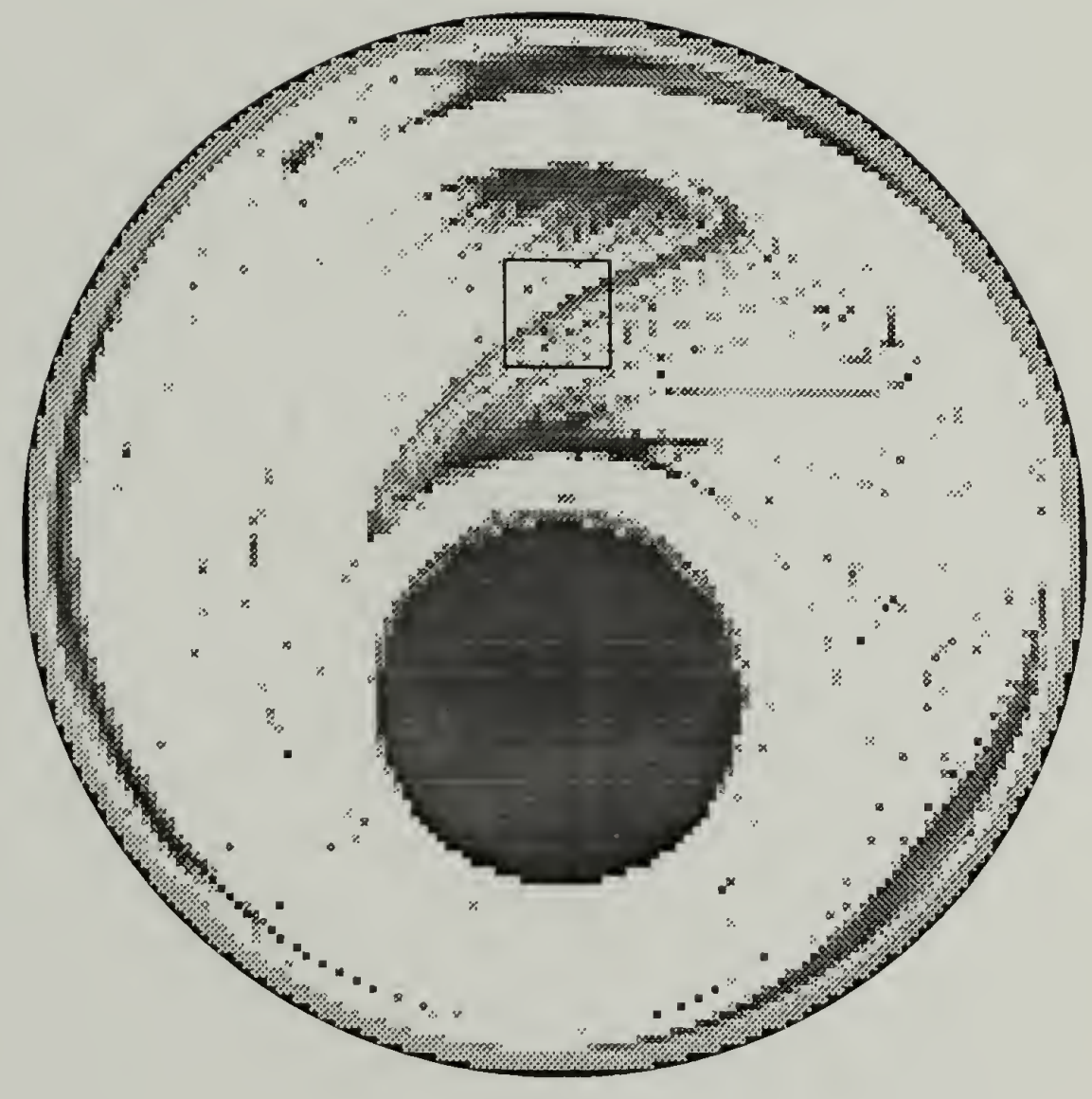

Figure 5.10: Stretching plot with location of region where detailed stretching computation will be performed. Parameters for the flow are $r = 1/3$, $e = 0.3$, $\theta = 270°$, and $\Omega = -3.0$.

(a)

(b)

Figure 5.11: Agreement in detail between stretching plots and experiments. The flow parameters are $r = 1/3$, $e = 0.3$, $\Omega = -3.0$, and $\theta = 270°$. (a) shows the stretching plot and (b) shows the corresponding experiment.

ignore the remainder of the pixels. A plot of this type is shown in figure 5.12(a). The highest stretching regions form a striation pattern very much like the pattern observed in the experiments.

Since our hypothesis is that the manifolds are the reason for the agreement between the stretching plots and experiments we make a plot of the manifolds in the same region of the flow as the highly detailed stretching plot is made. Figure 5.12(b) shows the stable manifolds for the two hyperbolic periodic points with the largest eigenvalues. We plot the manifolds of two hyperbolic periodic points because they have very similar eigenvalues. There is an almost exact correspondence between the highest stretching regions and the stable manifolds. The reason that the stable manifolds are used is because the stretching plot is done as a function of initial position. One further point of note is that the manifolds and stretching plot correspond to the same number of periods. The conclusion to be drawn from this result is that in order for a point to experience a large amount of stretching it must pass close to a hyperbolic point.

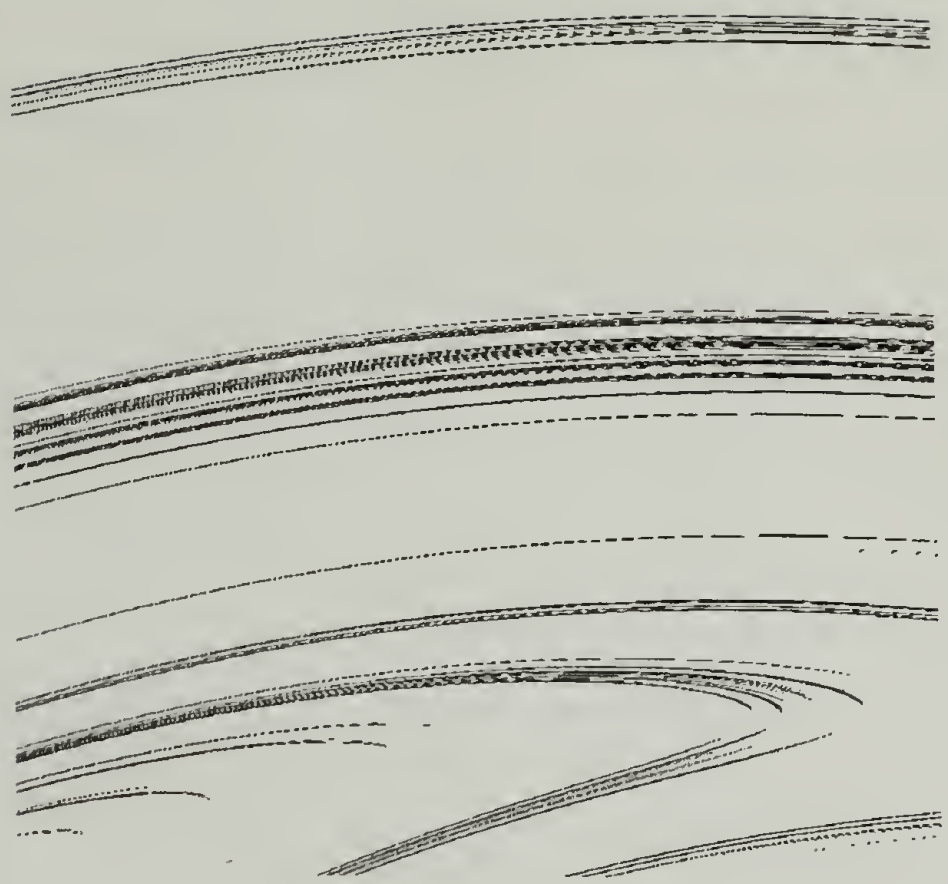

(a)

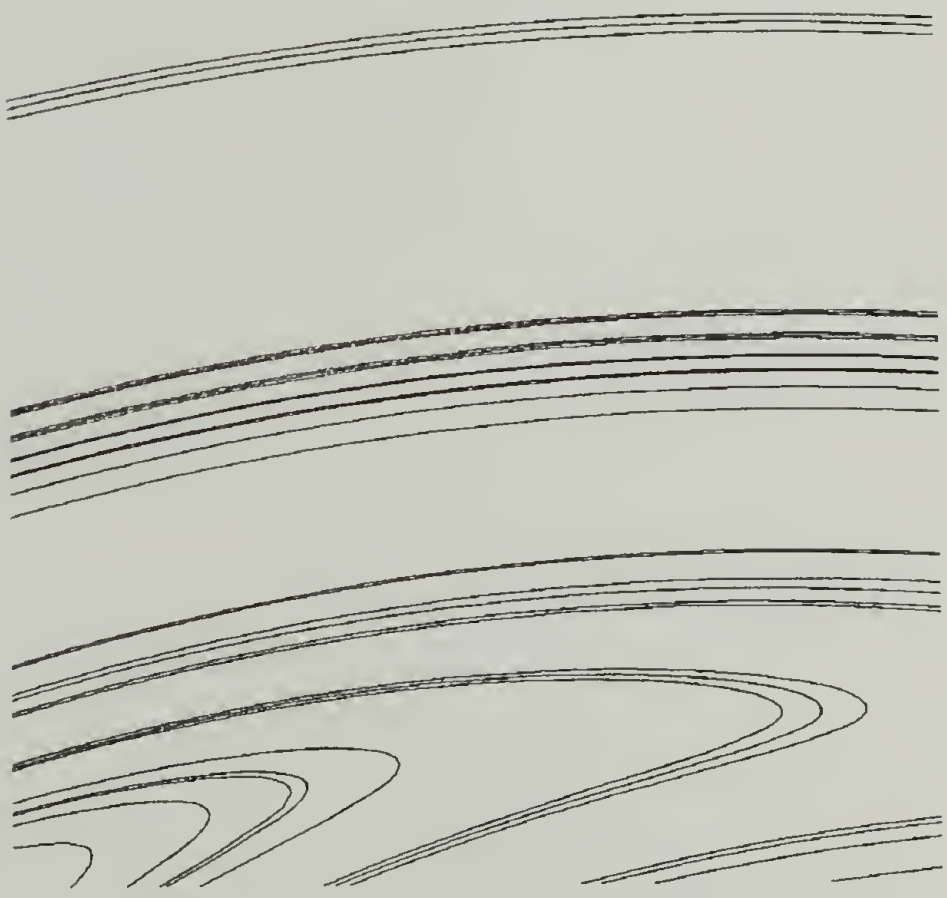

(b)

Figure 5.12: Comparison of high stretching region with the manifolds. (a) shows the regions with the largest 6.25% of stretching. (b) shows the unstable manifolds of the periodic points with largest eigenvalues.

CHAPTER 6

DISCRETIZED VELOCITY FIELD

The journal bearing flow affords us the luxury of an analytic expression for its stream function. However, it is rare to have an exact expression for the velocity field in flows of practical interest. Quite often the velocity field must be determined with a finite element or finite difference technique. The purpose of this chapter is to determine whether or not the computational techniques developed in chapter 4 yield meaningful results if the velocity field is discretized. To examine this problem we divide up the flow domain into finite elements and use them to determine the velocity field. Rather than solve the finite element problem numerically, the discretized velocity field is generated by assigning the velocity from the exact solution to the nodes of the discretized flow domain. This allows us to eliminate any errors due to an inexact solution and study only the effects of a discretized representation of the velocity field.

6.1 Construction of the Elements

For our purposes the major criterion for choosing a method of discretization is the ability to locate which element contains a particular point. This is in contrast to standard finite element problems where the discretization of the domain is chosen

to facilitate a numerical solution. However, since we use the exact velocity field to determine the velocities at the nodes rather than by some numerical technique, out major concern is searching rather than numerically solving a partial differential equation.

The general algorithm used to discretize the flow domain is first to divide the domain into a series of eccentric rings and then divide each ring into triangular elements such that the vertices of the triangles are on the edges of the rings (i.e. each ring is one row of elements wide).

Before explaining exactly how the flow domain is divided up into elements it is instructive to examine the equations Wannier [22] used to describe the locations of the cylinders. Basically the transformation from bipolar to rectangular coordinates is used to describe the location of the inner and outer cylinders. Figure 6.1 shows the coordinate system used. The y-axis is put through the centers of the two cylinders. The centers of the inner and outer cylinders are distances d_{in} and d_{out} respectively from the origin. The quantities d_{in} and d_{out} are chosen such that

$$d_{in}^2 - r_{in}^2 = d_{out}^2 - r_{out}^2 = s^2. \tag{6.1}$$

Note that we must have

$$d_{out} - d_{in} = e. \tag{6.2}$$

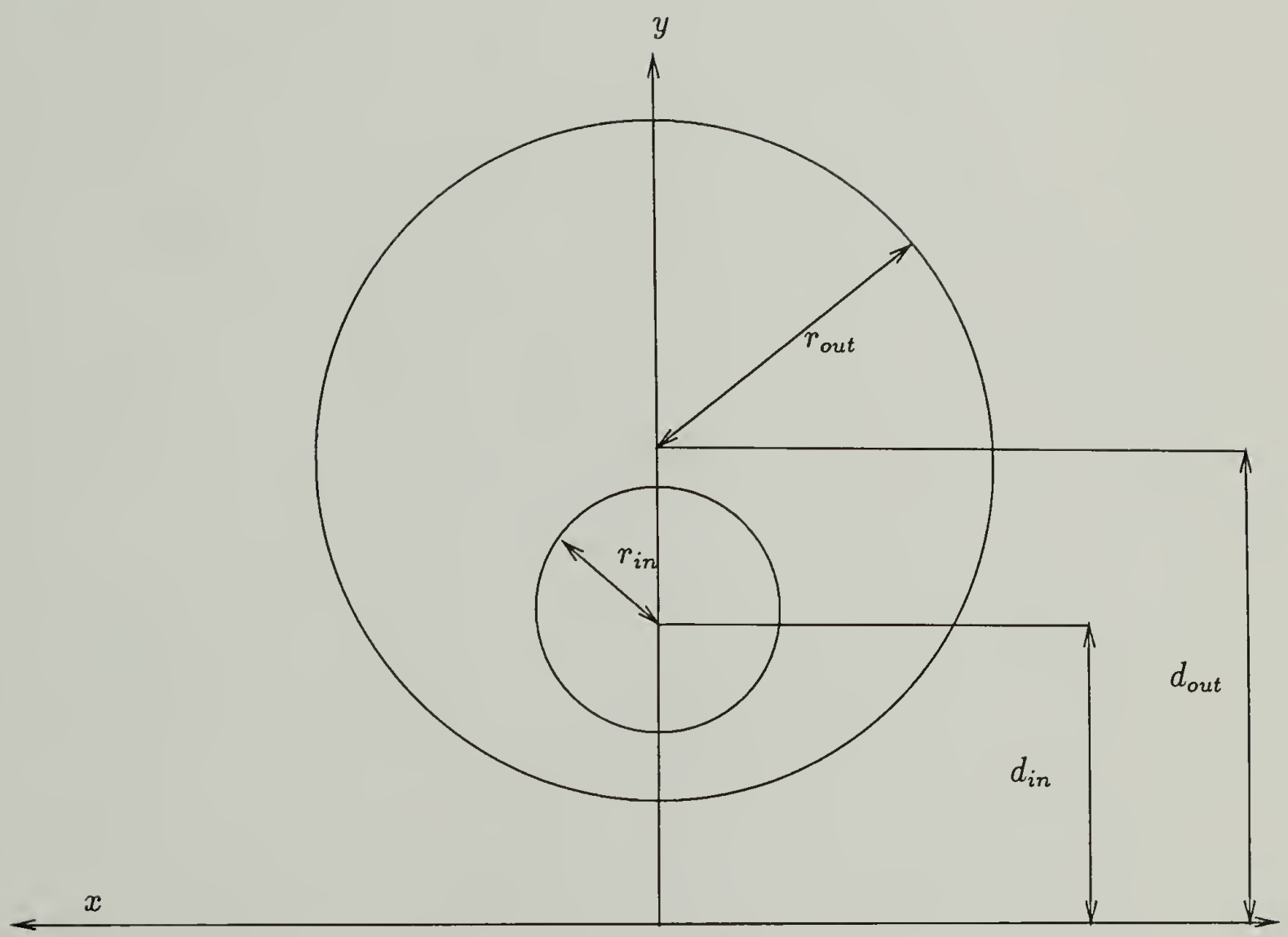

Figure 6.1: Journal bearing coordinate system.

The constant s is determined from the radii of the cylinders and the eccentricity according to:

$$s^2 = \frac{1}{4e^2}(r_{out} - r_{in} - e)(r_{out} - r_{in} + e)(r_{out} + r_{in} - e)(r_{out} + r_{in} + e). \qquad (6.3)$$

A whole family of circles with different radii and centers can be defined using s as

$$d^2 - r^2 = s^2. \qquad (6.4)$$

In order to form the elements a sequence of eccentric circles with constant difference in the radii are created using equation 6.4. Nodes are then placed on each circle approximately Δr apart (where Δr is the difference in radii between two neighboring circles). The nodes are connected by an algorithm to form triangular elements.

Figure 6.2 shows the elements created by the above process for the two sizes of elements used in this work. Figure 6.2(a) shows 1257 elements and figure 6.2(b) shows 5027 elements. There are two important points to make about the element generation scheme. First, the boundaries are naturally formed by this method without any need for special constraints. Second, it is obvious from the figure that the elements are not of a uniform size throughout the domain. This is actually somewhat advantageous in this case since the elements are smallest exactly where the gradients in the velocity field are the greatest.

Both first and second order elements are used. For both orders nodes are placed at the corners of the elements. When second order elements are used we need three

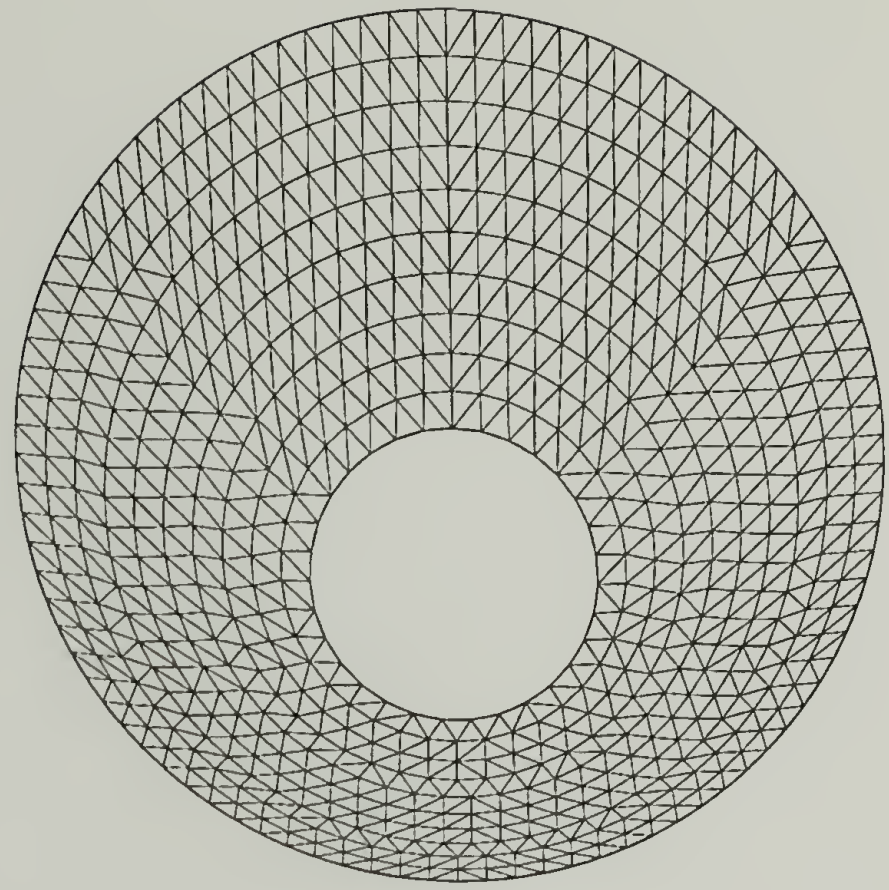

(a)

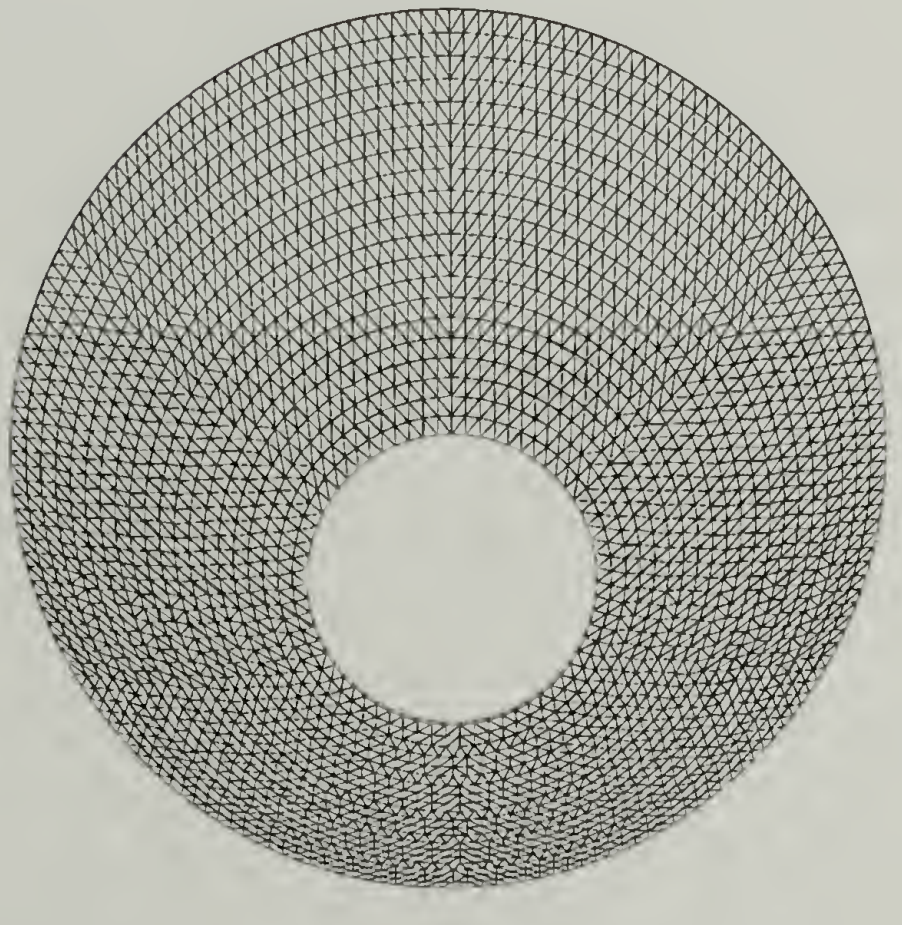

(b)

Figure 6.2: Elements for approximate velocity field.

more nodes and the extra nodes in each element are taken at the midpoint of each side. The value of the velocity in an element is approximated as

$$v = ax + by + c \tag{6.5}$$

for a first order node and

$$v = ax^2 + bxy + cy^2 + dx + ey + f \tag{6.6}$$

for a second order node. The values of a, b, c (and d, e, f for second order) are determined for each element from the velocities at the nodes by solving a 3×3 or 6×6 system of linear equations. In summary, there are four approximate velocity fields used. We refer to them as fields 1-4. Field 1 has 1257 first order elements, field 2 has 5027 first order elements, field three has 1257 second order elements, and field 4 has 5027 second order elements.

6.2 Steady State Streamlines

Before we conduct time periodic flow computations, such as Poincaré sections, using the approximate velocity fields we should first establish how accurately they represent the steady flow. In order to test the agreement with the exact solution we plot the pathlines of some selected fluid elements. Since the flow is steady the pathlines should be equivalent to the streamlines and the plots generated should resemble the steady state streamlines shown in figure 2.6. At the very least the

pathlines should close back on themselves. Figure 6.3 shows the pathlines generated for the first and second order elements of both element sizes. A plot of the pathlines generated using the exact velocity field is also given in figure 6.3(c) for reference.

The pathlines of all four approximate velocity fields show good agreement with the pathlines of the exact velocity field. However, in field 1 the pathline near the inner cylinder appears to be drifting away from the inner cylinder. Also, the behavior near the hyperbolic point is somewhat different for the first order elements as compared to the exact pathlines. The pathlines for both resolutions of second order elements are indistinguishable from the exact pathlines. Based on these results we expect that computations using field 1 will compare poorly to ones using the exact velocity field. It is still undetermined how well the other fields will work since the computations we have developed to study chaos are undoubtedly more sensitive to errors in the velocity field than computing pathlines for the steady flow.

6.3 Poincaré Sections

The results of the previous section suggest that, except for field 1, the approximate velocity fields may yield results similar to the exact velocity field in unsteady flow computations. In the first set of unsteady flow computations we generate Poincaré sections using the approximate velocity fields. This will be a much stiffer test of how accurately the approximate velocity fields represent the exact velocity

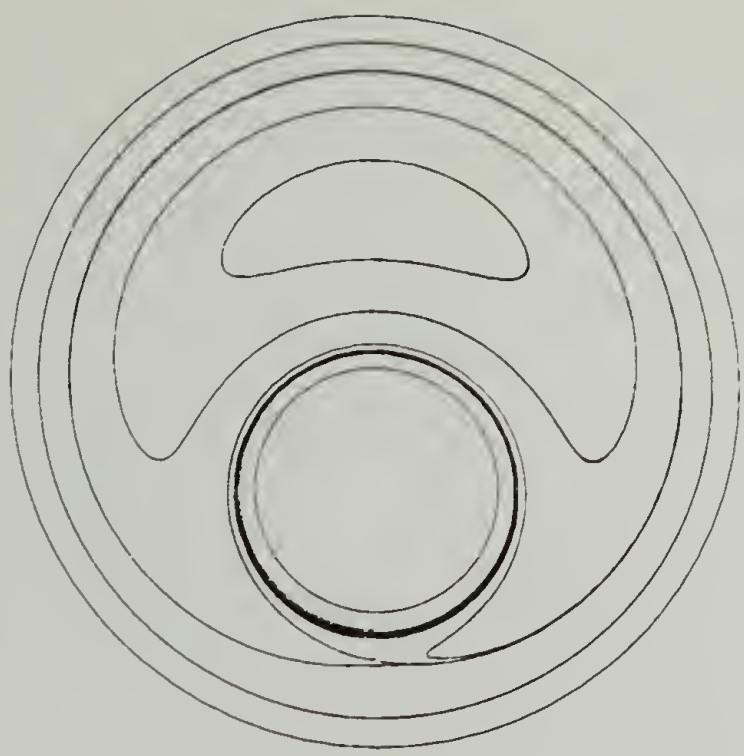

(a)

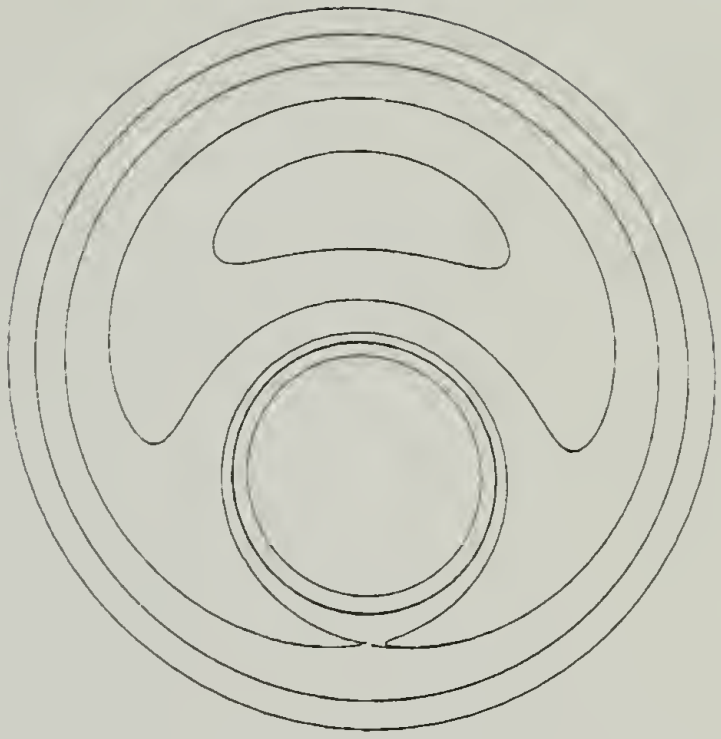

(b)

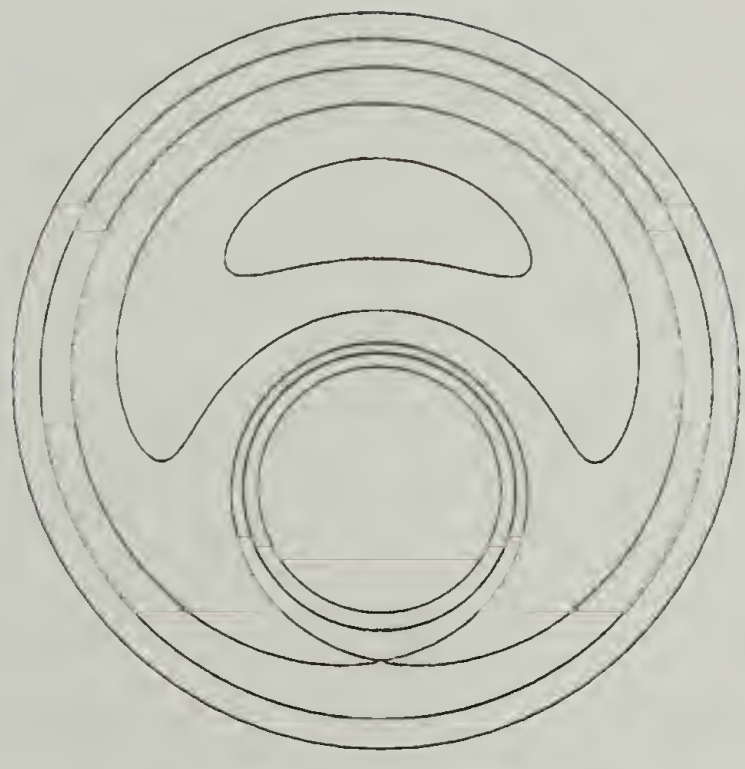

(c)

Figure 6.3: Streamlines for approximate velocity field. (a) 1257 first order elements, (b) 5027 first order elements, (c) exact velocity field, (d) 1257 second order elements, and (e) 5027 second order elements.

Continued, next page.

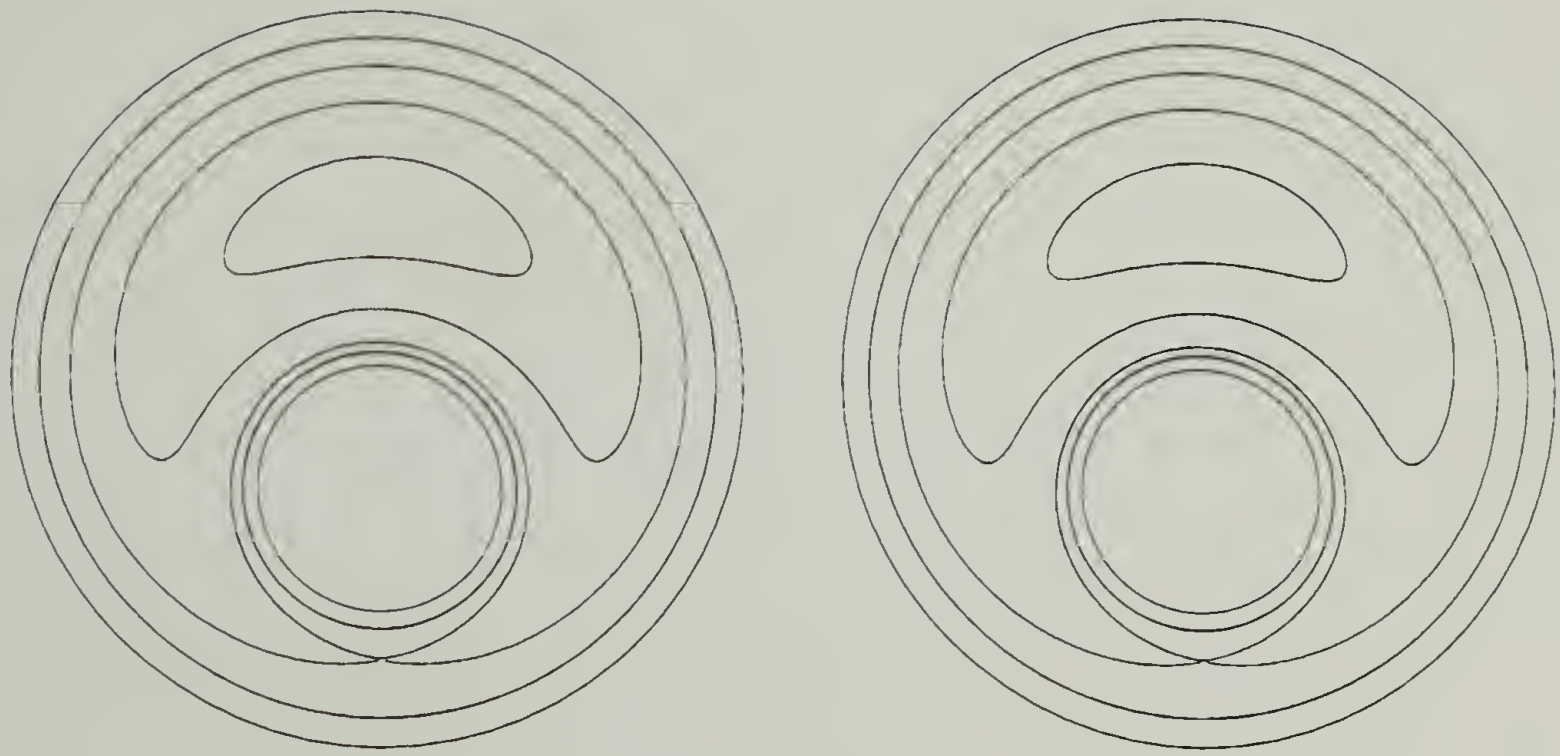

(d) (e)

Figure 6.3: continued.

field than were the pathline plots. This is due to the very long times trajectories are followed for the Poincaré sections. Also, the flow will be unsteady (although at any particular moment in time the flow is actually steady).

Figure 6.4 shows Poincaré sections generated using the four approximate fields for parameters $\theta = 180°$, $e = 0.3$, $r = 1/3$, and $\Omega = -3.0$. The Poincaré section generated using the exact velocity field is also shown for reference. For all four approximate velocity fields the basic structure of the Poincaré sections agree with the Poincaré section of the exact velocity field. However, field 1 shows chaotic like behavior even where it should be regular and appears to be void of trajectories in the chaotic region of the exact flow. This behavior is no doubt due the the inaccuracy of the velocity field and the differences between the regular and chaotic regions. There will be a larger error in computing the locations of points in the chaotic region than in the regular region. As a result, points are more likely to wander from the chaotic region into a regular region than they are to move from a regular region to a chaotic region. So the results from field 1 also show the difference between the regular and chaotic regions but in an unfamiliar manner.

The remaining approximate velocity fields all yield results in very good agreement with the exact velocity field. The results from field 4 are particularly good, being practically indistinguishable from the result of the exact velocity field. The basic conclusion of these results is that it is possible to use an approximate velocity

(a)

(b)

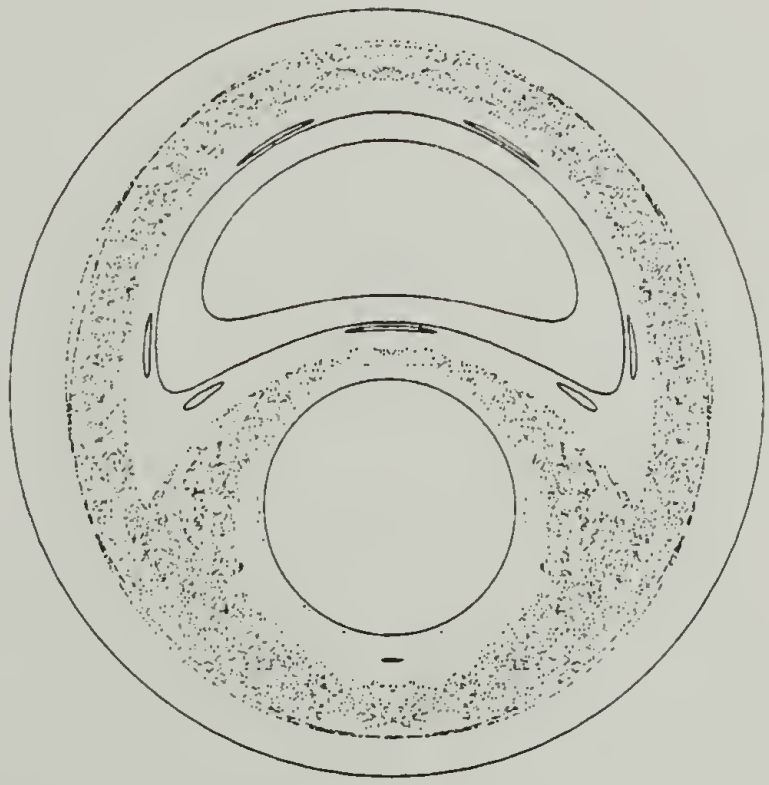

(c)

Figure 6.4: Poincaré sections for approximate velocity field with $e = 0.3$, $r = 1/3$, $\theta = 180°$, and $\Omega = -3.0$. (a) 1257 first order elements, (b) 5027 first order elements, (c) exact velocity field, (d) 1257 second order elements, and (e) 5027 second order elements. The initial conditions are identical for all plots.

Continued, next page.

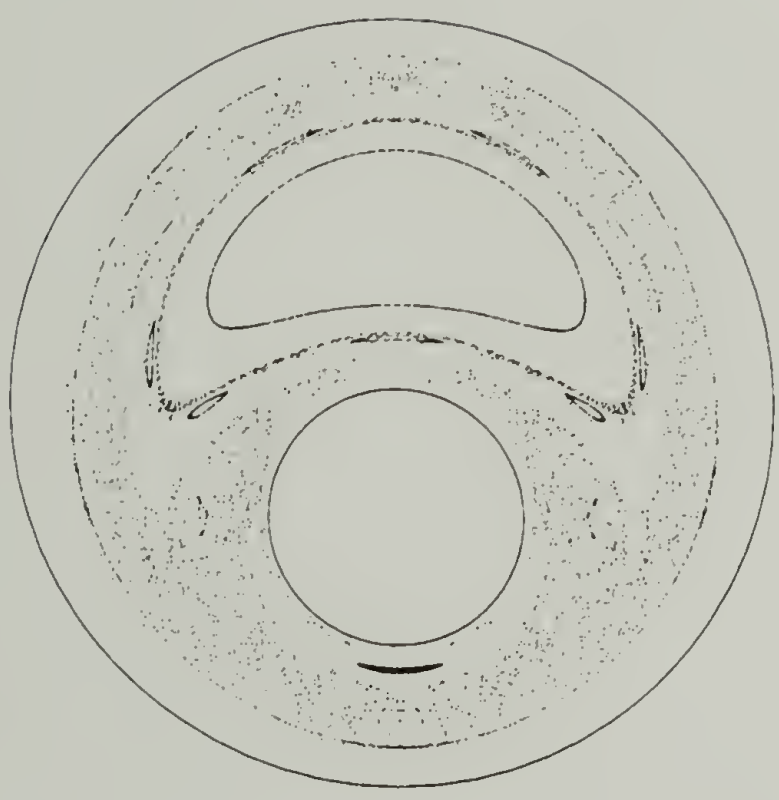

(d)

(e)

Figure 6.4: continued.

field to perform our Poincaré section computations and have confidence that the results will be meaningful.

6.4 Stretching Plots

Stretching plots provide a more detailed method to analyze the mixing of a flow than do the Poincaré sections. Therefore, stretching plots are the final type of computation we do using the approximate velocity field. The computation of stretching requires that we know the gradients of the velocity field in addition to the velocity field itself. In most algorithms for solving fluid flow problems the gradients of the velocity field would be one order less precise than the velocity field itself. With this in mind we only use the second order approximations of the velocity field and first order approximations for the gradient of the velocity field. In the same spirit we could have used a zeroth approximation to the gradients with the first order elements. But the discontinuities of the gradients between elements would have made the simulations extremely difficult.

Figure 6.5 shows the stretching plots for the two element sizes. The parameters for these plots are $\theta = 270°$, $e = 0.3$, $r = 1/3$, and $\Omega = -3.0$. In both cases the elements are second order in velocity and first order in the gradients of velocity. The results for the exact velocity field are shown for comparison. As with the Poincaré sections, there is basic agreement between the approximate velocity fields and the

(a)

(b)

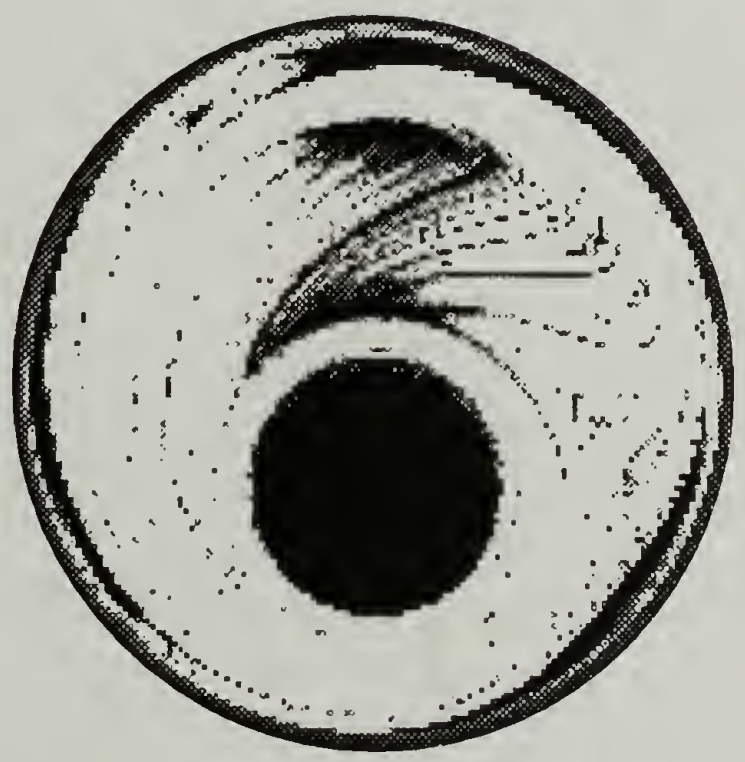

(c)

Figure 6.5: Stretching plots for approximate velocity field with $e = 0.3$, $r = 1/3$, $\theta = 270°$, and $\Omega = -3.0$. (a) 1257 elements, (b) 5027 elements, (c) exact velocity field. The elements are second order in velocity and first order in the gradients of the velocity.

exact velocity field. Actually the agreement is quite good. The most important point to note is that all of the features visible in the exact stretching plot are visible in the approximate stretching plots. Also there are no 'extra' features in the stretching plots for the approximate velocity fields. Again we see that we can have confidence that results computed using a discretized velocity field will accurately reflect the chaotic behavior of the flow.

CHAPTER 7

CONCLUSIONS

The principal goal of this research was to develop a base of knowledge about fluid mixing in a simple flow, the eccentric cylinder system. The advantage of studying the journal bearing is that it is a physically realizable flow with an analytic expression for the stream function. In other words, it can be studied both experimentally and computationally. The synergism between the two gives us insight into mixing processes that cannot be obtained from experiments or analysis alone. One of the most important of these insights is the ability to determine how well a number of computational methods are able to predict what sort of mixing, as shown by dye experiments, a given flow will exhibit. It is clear that no one particular computational method can provide a complete prediction. If we just want to get a gross picture of the spreading of the dye, then the Poincaré section is adequate. The chaotic regions of the Poincaré sections match the regions that the dye spreads over in experiments. However, the match is not perfect and there is no information about the rate of mixing in a Poincaré section. Further, some phenomena which look quite spectacular in the Poincaré sections do not show up in any significant way in the experiments (i.e. the Poincaré sections can be misleading if viewed on their own). The plot of the

eigendirections associated with the hyperbolic periodic points shows a strong correlation to the alignment of the striations in the mixing experiments. However, since the periodic points are not distributed uniformly throughout the flow, they cannot form a complete picture of the striations. A more complete picture is given by the unstable manifolds of the hyperbolic periodic points; the manifolds of period-one manifolds give a template for the folding of the dye throughout the chaotic region but the method can only give a template, not the full striation pattern.

The best indicator of dye spreading is given by stretching plots. The stretching plots seem to match the experiments extraordinary well. The probable reason for this is that the high stretching regions appear to fall on the manifolds of the hyperbolic periodic points with the largest eigenvalues. This results in the stretching plots resembling the shape of the manifolds. We have seen that the experiments adopt the shape of the manifolds as well. The stretching plots agree with experiments because they are both manifestations of the same phenomena. This match does not come without a cost however; the computational time for these stretching plots is at least an order of magnitude greater than any other method and becomes even greater if more resolution is desired. Note that all of these methods deal with the chaotic region. From the viewpoint of mixing it is a reasonable approximation to consider fluid elements in the regular regions to not stretch or mix at all; the regular regions are best thought of as 'dead' zones.

When the cylinders are operated in a co-rotating fashion we found that the chaos was more widespread that for the equivalent counter-rotating flow. In fact, for some parameter values the counter-rotating flow produced large islands while the co-rotating flow was nearly globally chaotic. However, we observed that the mixing rate was lower for the co-rotating flows in the sense that it took them a much longer to fill the chaotic region than the equivalent counter-rotating flows.

The type of waveform used to drive the cylinders appeared to have little effect on the results, at least for the restricted set of waveforms studied here. Further, it was possible to make the results due to the different waveforms even more similar by adjusting the strength of the deviation from the average velocity. The Melnikov method was the basis of a technique to determine the desired adjustments to the waveforms. This technique only requires the knowledge of the steady flow system and the waveform of the perturbation. When a discretized velocity field was used in conjunction with the computational methods we developed the results could still accurately reflect the chaotic behavior of the system provided the mesh size was sufficiently small.

APPENDIX

WANNIER'S SOLUTION FOR THE STREAM FUNCTION

Wannier [22] solved the eccentric rotating cylinders problem using two pieces of information. First, any solution to the biharmonic equation in two dimensions can be writen in terms of harmonic functions. If the streamfunction is a function of x and y then a solution to a creeping flow problem is found by solving:

$$\nabla^4 \Psi = 0.$$

Where Ψ can be writen in terms of harmonic functions as

$$\Psi = y\Phi_1 + \Phi_2$$

or

$$\Psi = (x^2 + y^2)\Phi_1 + \Phi_2$$

where

$$\nabla^2 \Phi_1 = \nabla^2 \Phi_2 = 0.$$

The second fact used to find a solution is that

$$\log \frac{x^2 + (s+y)^2}{x^2 + (s-y)^2}$$

is a harmonic function which is constant for a whole family of eccentric cylinders. The proper combination of this function and its derivatives gives a solution to the creeping flow fluid problem. That solution (in dimensionless form) is:

$$\begin{aligned}\Psi &= A\log\frac{x^2+(s+y)^2}{x^2+(s-y)^2}+B\frac{y(s+y)}{x^2+(s+y)^2}+C\frac{y(s-y)}{x^2+(s-y)^2}\\ &\quad +Dy+E(x^2+y^2+s^2)+F\,y\,\log\frac{x^2+(s+y)^2}{x^2+(s-y)^2}\end{aligned}$$

where

$$A = \frac{1}{2}(s^2-d_1d_2)\times\left[\frac{2(d_2^2-d_1^2)(rv_1+v_2)}{(1+r^2)\left((1+r^2)\log\frac{(d_1+s)(d_2-s)}{(d_1-s)(d_2+s)}-4s\epsilon\right)}+\frac{r^2(v_1/r-v_2)}{s(1+r^2)\epsilon}\right]$$

$$B = (d_1+s)(d_2+s)\times\left[\frac{2(d_2^2-d_1^2)(rv_1+v_2)}{(1+r^2)\left((1+r^2)\log\frac{(d_1+s)(d_2-s)}{(d_1-s)(d_2+s)}-4s\epsilon\right)}+\frac{r^2(v_1/r-v_2)}{s(1+r^2)\epsilon}\right]$$

$$C = (d_1-s)(d_2-s)\times\left[\frac{2(d_2^2-d_1^2)(rv_1+v_2)}{(1+r^2)\left((1+r^2)\log\frac{(d_1+s)(d_2-s)}{(d_1-s)(d_2+s)}-4s\epsilon\right)}+\frac{r^2(v_1/r-v_2)}{s(1+r^2)\epsilon}\right]$$

$$D = \frac{d_1\log\frac{d_2+s}{d_2-s}-d_2\log\frac{d_1+s}{d_1-s}-2s\frac{1-r^2}{1+r^2}}{\left((1+r^2)\log\frac{(d_1+s)(d_2-s)}{(d_1-s)(d_2+s)}-4s\epsilon\right)}(rv_1+v_2)-\frac{r^2(v_1/r-v_2)}{(1+r^2)\epsilon}$$

$$E = \frac{\frac{1}{2}\log\frac{(d_1+s)(d_2-s)}{(d_1-s)(d_2+s)}}{\left((1+r^2)\log\frac{(d_1+s)(d_2-s)}{(d_1-s)(d_2+s)} - 4s\epsilon\right)}(rv_1+v_2)$$

$$F = \frac{\epsilon(rv_1+v_2)}{\left((1+r^2)\log\frac{(d_1+s)(d_2-s)}{(d_1-s)(d_2+s)} - 4s\epsilon\right)}$$

$$r = \frac{\mathrm{R1}}{\mathrm{R2}}$$

$$\epsilon = \frac{\mathrm{EC}}{\mathrm{R2}}$$

$$d_1 = \frac{\mathrm{D1}}{\mathrm{R2}}$$

$$d_2 = \frac{\mathrm{D2}}{\mathrm{R2}}$$

$$s = \frac{\mathrm{S}}{\mathrm{R2}}$$

v_1 = velocity of the inner cylinder

v_2 = velocity of the outer cylinder

R1 = radius of the inner cylinder

R2 = radius of the outer cylinder

EC = distance between cylinder centers

$$\mathrm{S}^2 = \frac{1}{4\mathrm{EC}^2}(\mathrm{R2 - R1 - EC})(\mathrm{R2 - R1 + EC})(\mathrm{R2 + R1 - EC})(\mathrm{R2 + R1 + EC})$$

D1 = distance from x-axis to center of inner cylinder

D2 = distance from x-axis to center of outer cylinder

BIBLIOGRAPHY

[1] Middleman, S. *Fundamentals of Polymer Processing.* McGraw-Hill, New York, 1977.

[2] Franjione, J. G. and Ottino, J. M. Feasibility of numerical tracking of material lines in chaotic flows. *Physics of Fluids*, 30:3641–3643, 1987.

[3] Chaiken, J., Chevray, R., Tabor, M., and Tan, Q. M. Experimental study of lagrangian turbulence in a stokes flow. *Proceedings of the Royal Society of London*, A 408:165–174, 1986.

[4] Chaiken, J., Chu, C. K., Tabor, M., and Tan, Q. M. Lagrangian turbulence and spatial complexity in a stokes-flow. *Physics of Fluids*, 30(3):687–694, 1987.

[5] Balachandar, S. Chaotic advection in a stokes flow. Master's thesis, Brown University, 1985.

[6] Aref, H. and Balachandar, S. Chaotic advection in a stokes flow. *Physics of Fluids*, 29(11):3515–3521, 1986.

[7] Percival, I. and Richards, D. *Introduction to Dynamics.* Cambridge University Press, Cambridge, 1982.

[8] Abraham, R. H. and Shaw, C. D. *Dynamics - The Geometry of Behavior. Part One: Periodic Behavior.* Aerial Press, Inc., Santa Cruz, 1985.

[9] Abraham, R. H. and Shaw, C. D. *Dynamics - The Geometry of Behavior. Part Two: Chaotic Behavior.* Aerial Press, Inc., Santa Cruz, 1985.

[10] Abraham, R. H. and Shaw, C. D. *Dynamics - The Geometry of Behavior. Part Three: Global Behavior.* Aerial Press, Inc., Santa Cruz, 1985.

[11] Abraham, R. H. and Shaw, C. D. *Dynamics - The Geometry of Behavior. Part Four: Bifurcation Behavior.* Aerial Press, Inc., Santa Cruz, 1988.

[12] Baker, G. L. and Gollub, J. P. *Chaotic Dynamics: An Introduction.* Cambridge University Press, New York, 1989.

[13] Guckenheimer, J. and Holmes, P. *Nonlinear Oscillations, Dynamical Systems, and Bifurcations of Vector Fields.* Springer-Verlag, New York Berlin Heidelberg Tokyo, 1983.

[14] Lichtenberg, A. J. and Lieberman, M. A. *Regular and Stochastic Motion.* Springer, 1983.

[15] Ottino, J. M. *The Kinematics of Mixing: Stretching, Chaos and Transport.* Cambridge University Press, Cambridge, 1989.

[16] Wiggins, S. *Global Bifurcations and Chaos.* Springer - Verlag, Berlin Heidelberg New York Tokyo, 1988.

[17] Jeffrey, G. B. The rotation of two cylinders in a viscous fluid. *Proceedings of the Royal Society of London*, A 101:169–174, 1922.

[18] Duffing, G. Beitrag zur Theorie der Flüssigkeitsbewegung zwischen Zapfen und Lager. *Zeitschrift für angewandte Mathematik und Mechanik*, 4:297–314, 1924.

[19] Müller, W. Über die Drehung zweider Zylinder in einer zähen Flüssigkeit und die Theorie der Kräfte am Rotationsviskosimeter mit exzentrischen Zylindern. *Annalen der Physik*, 41:335–354, 1942.

[20] Müller, W. Beitrag zur Theorie der langsamen Strömung zweier exzentrischer Kreiszylinder in der zähen Flüssigkeit. *Zeitschrift für angewandte Mathematik und Mechanik*, 22:177–189, 1942.

[21] Ballal, B. Y. and Rivlin, R. S. Flow of a newtonian fluid between eccentric rotating cylinders: Inertial effects. *Archive of Rational Mechanics and Analysis*, 62:237–294, 1976.

[22] Wannier, G. H. A contribution to the hydrodynamics of lubrication. *Quarterly of Applied Mathematics*, 8(1):1–32, 1950.

[23] Franjione, J. G., Leong, C. W., and Ottino, J. M. Symmetries within chaos: a route to effective mixing. *Physics of Fluids A*, 1:1772–1783, 1989.

[24] Ariel Corp., New York, NY 10012. *Operating Manual for the DSP-16 Data Acquisition Processor*, 1987.

[25] Leong, C.-W. and Ottino, J. M. Experiments on mixing due to chaotic advection in a cavity. *Journal of Fluid Mechanics*, 209:463–499, 1989.

[26] Press, W. H., Flannery, B. P, Teukolsky, S. A., and Vetterling, W. T. *Numerical Recipes - The Art of Scientific Computing.* Cambridge University Press, New York, 1986.

[27] Rom-Kedar, V., Leonard, A., and Wiggins, S. An alytical study of transport, mixing and chaos in an unsteady vortical flow. *Journal of Fluid Mechanics*, 214:347–394, 1990.